Estuarine hydrodynamics in arid climates – a case study of the Persian Gulf and its small estuaries

Dissertation

with the aim of achieving a doctoral degree

at the Faculty of Mathematics, Informatics and Natural Sciences

Department of Earth System Sciences

at University of Hamburg

submitted by

Seyedtaleb Hosseini

Hamburg, 2025

Department of Earth Sciences

Date of Oral Defense:	25.03.2025
Reviewers:	Prof. Dr. Corinna Schrum
	Prof. Dr. Emil Stanev
Members of the examination commission:	Prof. Dr. Corinna Schrum
	Prof. Dr. Emil Stanev
	Dr. Johannes Pein
	PD Dr. Thomas Pohlmann
	Prof. Dr. Uwe A. Schneider
Chair of the Subject Doctoral Committee	
Earth System Sciences:	Prof. Dr. Hermann Held
Dean of Faculty MIN:	Prof. Dr.-Ing. Norbert Ritter

Eidesstattliche Versicherung | Declaration on Oath

I hereby declare and affirm that this doctoral dissertation is my own work and that I have not used any aids and sources other than those indicated.

If electronic resources based on generative artificial intelligence (gAI) were used in the course of writing this dissertation, I confirm that my own work was the main and value-adding contribution and that complete documentation of all resources used is available in accordance with good scientific practice. I am responsible for any erroneous or distorted content, incorrect references, violations of data protection and copyright law or plagiarism that may have been generated by the gAI.

Hamburg, 07.10.2024

S.T.Hosseini

Seyedtaleb Hosseini

Ort,den **|** City,date

Unterschrift **|** Signature

Abstract

Unlike positive estuaries, low-inflow estuaries such as inverse and salt-plug estuaries have received less scientific attention. This thesis aims to investigate the hydrodynamic aspects of these remarkable estuarine systems by example of the Persian Gulf (PG), the Mond River Estuary (MRE), and an idealized funnel-shaped estuary using observations and numerical modeling.

The PG region, characterized by an arid climate, represents an extraordinary environment for studying estuarine hydrodynamics. Classified as an inverse estuary due to higher evaporation than precipitation and river discharges, the PG provides a valuable case study for understanding the dynamics of low-inflow estuaries. The system is studied with a particular focus on the influence of tidal forcing on the exchange flows and salinity. Numerical experiments indicate that tidal forcing significantly increases the annual inflow-outflow rates at the Strait of Hormuz (SOH) to approximately ±0.54 Sv, which is more than double previous estimates. Tides enhance PG salinity through (i) intense landward (entering the PG) salt flux by tidal advection, and (ii) strong tidal mixing in the PG, especially at the SOH. On the northwestern and southern shallow banks of the PG, high salinity values imposed by tides coincide with peak values of the tidal Froude number (F_{rT}) and the formation of amphidromic points in these coastal areas.

The MRE, located on the northern coast of the PG, exhibits a salt-plug estuarine system during warm months, representing another type of low-inflow estuaries. In fact, the MRE transitions from a positive estuary in wet months to inverse and salt-plug estuaries during dry months. Also, the MRE exhibits a highly unsteady estuarine state following heavy rains. The unsteady state is characterized by the formation of a relatively freshwater lens between two high-salinity water masses: one from the PG and another from the hypersaline runoff passing saline soils upstream of the estuary

(freshwater lens estuary). The Péclet Number (Pe), calculated from observed salt flux terms, indicates a predominance of strong advective transport imposed by hypersaline runoff over diffusive transport throughout the MRE. Additionally, numerical modeling of the MRE indicates that a sea-level rise of 20 cm can result in an increase in salinity within the freshwater lens and positive estuaries, in contrast to a salinity decrease in inverse and salt-plug estuaries.

Furthermore, a three-dimensional hydrodynamic model is employed to compare various scenarios under different tidal conditions in an idealized funnel-shaped salt-plug estuary. The analysis reveals that when $\log(F_{rT}) > 3$, tidal forcing overcomes the density gradient, reinforcing the salinity maximum zone with a landward displacement. In this idealized estuary, the model demonstrates the development of longitudinal flows in two cells of positive and inverse estuarine circulations, detached by a salinity maximum zone. Meanwhile, two cells of positive estuaries are separated by a mixing maximum zone in the idealized freshwater lens estuary.

The results of these studies provide valuable foundations for understanding biogeochemical processes and sediment dynamics in low-inflow estuarine systems, which can support sustainable development considering water quality and climate change impacts worldwide.

Zusammenfassung

Im Gegensatz zu positiven Ästuaren sind Ästuare mit geringem Durchfluss, wie inverse Ästuare und „salt-plug“-Ästuare, bisher kaum wissenschaftlich erforscht worden. Ziel dieser Arbeit ist es, die hydrodynamischen Aspekte dieser bemerkenswerten Ästuarsysteme am Beispiel des Persischen Golfs (PG), des Mond River Ästuars (MRE) und eines idealisierten trichterförmigen Ästuars durch Beobachtungen und numerische Modellierung zu untersuchen.

Die PG-Region, die sich durch ein trockenes Klima, stellt eine außergewöhnliche Umgebung für die Untersuchung der Hydrodynamik von Ästuaren dar. Der PG wird als inverses Ästuar eingestuft, da die Verdunstung höher ist als die Niederschläge und Zuflüsse, und stellt somit eine wertvolle Fallstudie für das Verständnis der Dynamik von Ästuaren mit geringem Zufluss dar. Das System wird mit besonderem Augenmerk auf den Einfluss der Gezeiten auf Austauschströme und Salzgehalt untersucht. Numerische Experimente zeigen, dass die Gezeiten die jährlichen Zufluss-Abfluss-Raten in der Straße von Hormuz (SOH) auf etwa ±0,54 Sv erhöhen, was mehr als das Doppelte früherer Schätzungen ist. Die Gezeiten erhöhen den Salzgehalt des PG durch (i) einen intensiven landwärtigen (in den PG eintretenden) Salzfluss durch Gezeitenadvektion, und (ii) eine starke Gezeitenvermischung im PG, besonderes an der SOH. An den nordwestlichen und südlichen flachen Ufern des PG fallen hohe Salzgehaltswerte, die durch Gezeiten verursacht werden, mit Spitzenwerten der Froude-Zahl (FrT) und der Bildung von Amphidromischen Punkten in diesen Küstengebieten zusammen.

Das MRE an der Nordküste des PG weist in den warmen Monaten ein salt-plug-Ästuar auf, das eine andere Art von Ästuaren mit geringem Zufluss darstellt. Tatsächlich geht das MRE von einem positiven Ästuar in nassen Monaten in ein inverses Ästuar und ein salt-plug-Ästuar in trockenen Monaten über. Außerdem weist das MRE nach starken Regenfällen einen sehr instabilen Zustand auf. Dieser instationäre Zustand ist durch die Bildung einer Süßwasserlinse zwischen zwei hochsalinen Wassermassen gekennzeichnet: eine aus dem PG und die andere aus einem hypersalinen Abfluss, der

von stromaufwärts gelegenen salzhaltigen Böden stammt (Süßwasserlinsen-Ästuar). Die aus den beobachteten Salzflüssen berechnete Péclet-Zahl (Pe) deutet darauf hin, dass im gesamten MRE ein starker advektiver Transport durch den hypersalinen Abfluss gegenüber dem diffusiven Transport vorherrscht. Darüber hinaus zeigt die numerische Modellierung des MRE, dass ein Anstieg des Meeresspiegels um 20 cm zu einem Anstieg des Salzgehalts in der Süßwasserlinse und in den positiven Ästuaren führen kann, im Gegensatz zu einem Rückgang des Salzgehalts in inversen und salt-plug-Ästuaren.

Darüber hinaus wird ein dreidimensionales hydrodynamisches Modell eingesetzt, um verschiedene Szenarien unter unterschiedlichen Gezeitenbedingungen in einem idealisierten trichterförmigen salt-plug-Ästuar zu vergleichen. Die Analyse zeigt, dass die Gezeiten den Dichtegradienten für $\log(F_{rT}) > 3$ ist überwinden und die Zone des Salzgehaltsmaximums durch eine landwärtige Verschiebung verstärkt. In diesem idealisierten Ästuar zeigt das Modell die Entwicklung von Längsströmungen in zwei Zellen mit positiver und inverser Ästuarzirkulation, die durch eine Zone mit maximalem Salzgehalt getrennt sind. Hingegen werden im idealisierten Süßwasserlinsen-Ästuar zwei Zellen positiver Ästuare durch eine Zone mit einem Mischungsmaximum getrennt.

Die Ergebnisse dieser Studien liefern wertvolle Grundlagen für das Verständnis biogeochemischer Prozesse und der Sedimentdynamik in Ästuarsystemen mit geringem Zufluss, um somit weltweit eine nachhaltige Entwicklung hinsichtlich der Wasserqualität und Klimawandelauswirkungen zu befördern.

List of Publications

Publications related to this dissertation:

Study I

Hosseini, S. T., Stanev, E., Pein, J., Valle-Levinson, A., and Schrum, C. (2023). *Longitudinal and lateral circulation and tidal impacts in salt-plug estuaries*. Frontiers in Marine Science, 10, 1152625. doi: 10.3389/fmars.2023.1152625

Study II

Hosseini, S. T., Siadatmousavi, S. M., Stanev, E., Pein, J., and Schrum, C. (2024). *Transitions Between Different Estuarine States in a Low-inflow Estuary of Arid Coasts (Mond Estuary, Persian Gulf) with a Focus on Freshwater Lenses*. Regional Studies in Marine Science 74 (2024) 103525. doi: https://doi.org/10.1016/j.rsma.2024.103525

Study III

Hosseini, S. T., Stanev, E., Pein, J., Schrum, C., and Jacob, B. (2024). *Tidal Impacts on Volume and Salt Transport through the Strait of Hormuz and on Persian Gulf Salinity*. (to be submitted).

Contents

Abstract i

Zusammenfassung iii

List of Publications v

Contents vii

1 Introduction 1

2 Study I: Salt-plug Estuarine Hydrodynamics 16

3 Study II: Freshwater Lens Estuarine Hydrodynamics 38

4 Study III: Hydrodynamics of the Persian Gulf, as an inverse estuary 55

5 Discussion 89

6 Synthesis 99

References 106

Acknowledgements 112

1 Introduction

The complex interplay between oceanic environments, shelf seas and coastal processes has long fascinated oceanographers. Within the diverse fields of oceanography, two principal approaches can be distinguished: one focused on observations and their analysis, and the other based on theoretical frameworks employing numerical modeling techniques. Despite these approaches being distinct, they have been converging with the increasing integration of observational data and advancements in data assimilation techniques and numerical modeling.

1. Observational Approach: Historically, the field of physical oceanography in coastal and estuarine areas has relied heavily on the analysis of observational data collected by in situ instruments and satellite imagery. This empirical approach provides valuable insights into local processes but is often limited by sparse data coverage and temporal gaps.

2. Theoretical Approach and Numerical Modeling: From a theoretical viewpoint, numerical modeling has emerged as a powerful tool. By mathematically simulating oceanic processes, numerical models allow us to explore scenarios that are otherwise difficult or impossible to observe directly. These models capture the underlying physics, including fluid dynamics, thermodynamics, and transport mechanisms. Numerical simulations bridge the gap between theory and observation, enabling us to investigate complex interactions across spatial and temporal scales.

The integration of measurements into numerical modeling allows for the refinement of model accuracy and the improvement of our understanding of local processes. This thesis, situated in this context, uses available data to enhance numerical simulations by focusing on physical processes in the Persian Gulf (PG) and the Mond River Estuary (MRE) in the northern gulf. The thesis represents an example of collaboration between

regional and coastal oceanographic studies, contributing to a broader understanding of regional-coastal physical oceanography in arid climates such as the PG region. In other words, this study provides the convergence of theory, data, and modeling – a holistic approach that promises deeper insights into the ocean physics of estuaries and coastal seas with high evaporation.

From the perspective of ocean physics, it becomes evident that numerous aspects still need to be adequately explored within the arid oceanic basins, such as the PG region. The thesis attempts to clarify some of these unresolved issues (see the "Background information"). The thesis, which comprises three individual studies, addresses the hydrodynamics of estuarine and coastal systems in the Persian Gulf, an arid climate region characterized by high evaporation rates and limited freshwater inputs.

The Persian Gulf (PG, see Figure 1) is located between 24 °N and 30 °N latitude, experiencing a subtropical climate in winter and a tropical climate in summer (Sheppard, 2019). The PG's high evaporation rate classified it as a large inverse estuary (Johns et al., 2003; Lorenz et al., 2020; Kämpf & Sadrinasab, 2006), where dense PG-water sinks and flows out to the open ocean, associated with inflowing surface low-salinity Indian Ocean water.

Almost all freshwater rivers entering the PG originate from the northern (Iranian) side (Reynolds, 1993), including the Mond River. The MRE extends east to west, with the Persian Gulf situated west (see Figure 1). During the dry summer months, the MRE exhibits a salt-plug estuarine system (Ghaemi & Gholamipour, 2017), due to high evaporation and low river discharge. As a result, a zone with high salinity (salinity maximum zone or salt plug) is formed in the estuary's middle, which can strongly impact estuarine hydrodynamics. Actually, salt-plug and inverse estuaries are two main types of low-inflow estuaries (Valle-Levinson, 2011) in the arid area of the PG in which the evaporation-precipitation balance tends to be negative. Occasional hypersaline river floods during wet months create an unsteady state with a freshwater lens

between high-salinity waters from the PG and the hypersaline runoff (Hosseini & Siadatmousavi, 2018).

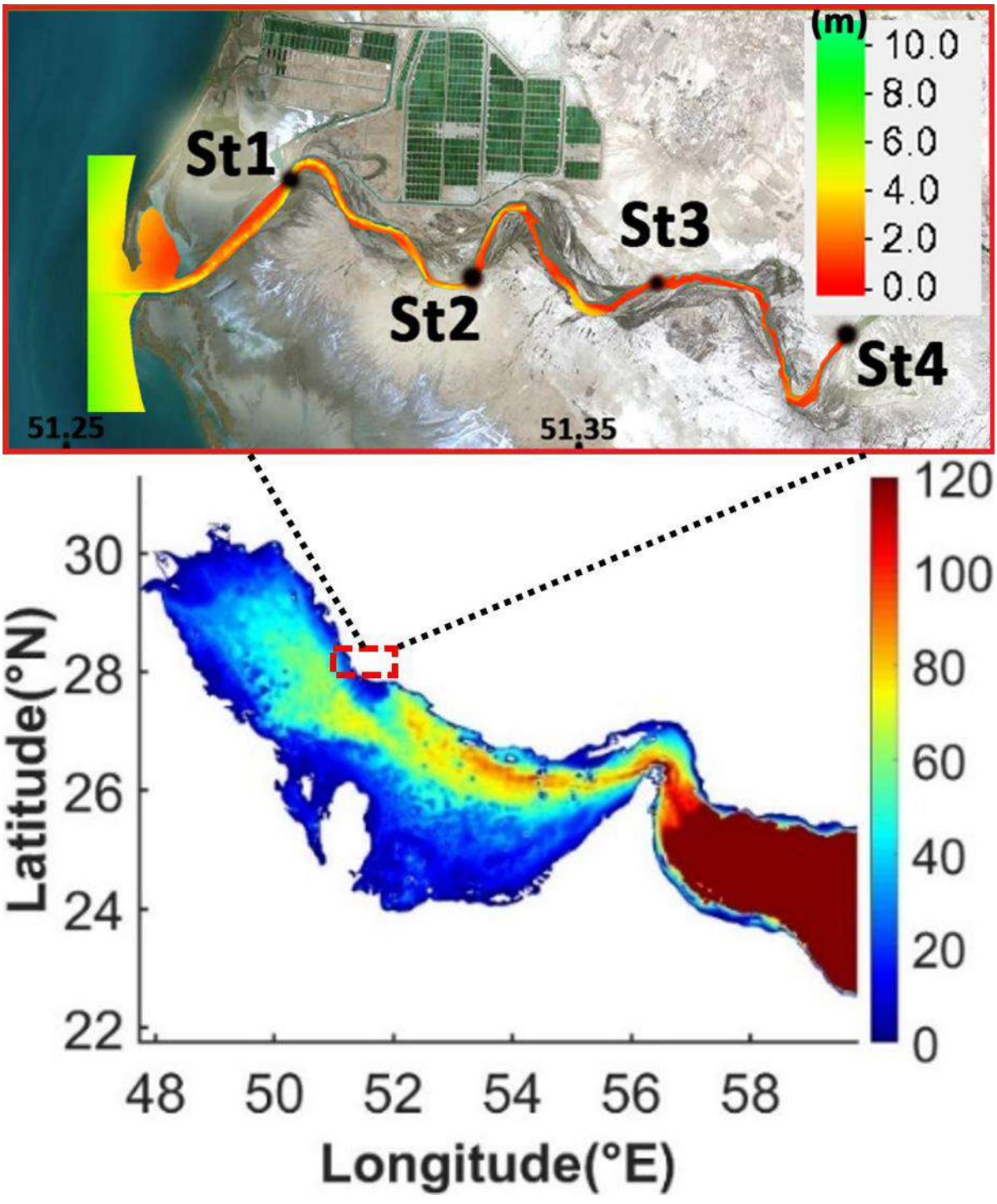

Figure 1. *Bathymetries (m) of the Persian Gulf and the Mond River Estuary located along the northern coast of the gulf*

The MRE, with its distinctive seasonal transitions and sensitivity to climatic and hydrological changes, serves as an optimal natural-laboratory for investigating estuarine hydrodynamics in arid regions.

By advancing our understanding of these unique estuarine systems, this research offers invaluable insights for addressing hydrodynamical challenges in low-inflow estuaries. Some important hydrodynamical characteristics involved in the inverse estuary of the PG, salt-plug estuaries, and the freshwater lens system of the MRE have not been analyzed by relevant earlier studies. This thesis aims to elucidate the unclear physical processes governing these three estuarine systems dedicated to the arid climate of the PG. In other words, this research fills gaps in the existing literature on estuarine hydrodynamics and provides a foundation for both future physical-biogeochemical studies and informed management in arid coastal regions.

This introductory chapter proceeds with a general picture of the research, providing pertinent background information on the hydrodynamics of the three estuaries. This is followed by a description of the existing gaps in previous related studies, which serve to motivate the research questions and objectives on salt-plug estuaries in general, the freshwater lens state of the MRE, and the PG-inverse estuary.

Background information

Salt-plug estuaries

Valle-Levinson (2010) classified estuaries into three categories based on their water balance: positive, inverse, and low-inflow (salt-plug) estuaries. According to Valle-Levinson (2011), estuaries can be classified into two general groups: positive and low-inflow estuaries. The latter category (low-inflow estuaries) can be further subdivided into four distinct types of estuarine dynamics: inverse, thermal, salt-plug, and thermal-plug (or thermal bar).

There are numerous regions worldwide that exhibit prolonged periods of low inflow to estuaries; however, research in this domain is still in its preliminary stages (Largier, 2023).

A salt-plug estuary features two along-channel (longitudinal) circulation cells on either side of a salinity maximum zone (salt plug). In the seaward direction from the salt plug, salinity (density) decreases by fresher seawater than the salt plug, resulting in an inverse estuarine circulation: surface low-density seawaters flow into the estuary, while denser near-bottom waters flow out to the ocean. In the landward direction from the salt plug, riverine freshwater inflows decrease salinity, establishing a positive circulation cell: low-density waters flow towards the salt plug at the surface, while denser waters flow landward near the bottom (Wolanski, 1986; Valle-Levinson, 2010).

Relatively few studies have explored the hydrodynamics of salt-plug estuaries compared to positive estuaries. Key studies include those by Wolanski (1986), Valle-Levinson and Bosley (2003), Valle-Levinson (2010), Valle-Levinson (2011), Cabrera et al. (2014), Shaha and Cho (2016), Juarez et al. (2020), Juarez et al. (2022), Mariani et al. (2022), and Shaha et al. (2022).

Wolanski (1986) first identified a salt-plug estuary in the Alligator River Estuary in northern Australia during warm months. Valle-Levinson and Bosley (2003) observed similar behavior in the Gulf of Fonseca, located on the Pacific Ocean side of Central America, which transitions from a salt-plug estuary in dry months to a typical positive estuary during wet months. In their study of Malampaya Sound in Palawan, Philippines, Cabrera et al. (2014) observed that the Sound behaves as a salt-plug estuary during dry periods. The salt plug acts to restrict water exchange between the Inner and Outer Sound, which likely explains the observed differences in nutrient, sediment, and phytoplankton composition between the two areas. Additionally, the salt plug may prevent the spread of blooms into the Sound. However, the presence of the salt plug has been found to have a negative environmental impact, as it traps pollutants from river inflows into the Inner Sound (Cabrera et al., 2014). The CTD summer

measurements carried out in the Mond River Estuary (MRE) on the northern coast of the Persian Gulf revealed the presence of a salt plug in the MRE (Ghaemi & Gholamipour, 2017). Mariani et al. (2022) examined the effect of regional climate change on the salinity distribution in Todos os Santos Bay, Brazil. It was demonstrated that the occurrence of hypersalinity events peaked in 2013, coinciding with the most severe regional drought on record. During this period, an estuarine salinity (density) plug was observed (Mariani et al., 2022).

Furthermore, a salt plug can be formed mainly due to a decrease in river discharges resulting from upstream barrages, as seen in the multi-channel Pasur River Estuary located in the southwestern coastal zone of Bangladesh (Shaha & Cho, 2016). Shaha et al. (2022) estimated the flushing time of the upper Pasur River Estuary during dry seasons. Their findings indicated that the flushing time during this season was approximately thirteen times longer than during wet seasons, due to a significant decrease in river discharge of nearly 94%. Additionally, the daily exchange volume decreased by approximately eight times during the dry season compared to the wet season. Consequently, the estuary is more dynamic during the wet season due to the large amount of river discharge it receives (Shaha et al., 2022).

It is also important to note that a salt plug can also form in positive estuaries of non-arid regions, such as Barataria Bay and the Mississippi River Delta. In these areas, freshwater pulses from the ocean into the bay can create a salt plug (Juarez et al., 2020). In their research, Juarez et al. (2022) also demonstrated that the persistence of a salt plug is dependent on two factors: tidal flushing and wind forcing. The same authors considered a buoyant coastal current modified by wind stresses and disregarded the effects of evaporation processes.

Previous hydrodynamic studies of salt-plug estuaries have largely focused on the observed salt plug and its relevant longitudinal variabilities, leaving gaps in understanding lateral variabilities (variations in estuarine properties perpendicular to the main axis). In particular, lateral (secondary) flows have not been investigated in the

existing literature reviews. This thesis aims to fill this knowledge gap, particularly by examining the neap-spring variability of lateral flows at the salt plug. The secondary flows reach approximately 10% of the magnitude of the longitudinal flow in normal (positive) estuaries. Nevertheless, they exert a considerable influence on the dispersion of estuarine waters (Chant, 2010).

Furthermore, the literature reviews on salt-plug estuaries have not yet considered the relative influence of density gradients and tidal forcing in these estuaries. This thesis also compares density gradients and tidal forcing in salt-plug estuarine systems.

The freshwater lens estuary

The MRE is unique in transitioning from a positive estuary to a freshwater lens condition during wet months. Heavy precipitation over saline soil areas upstream of the MRE can cause hypersaline runoff, creating a relatively freshwater lens between high-salinity waters from the PG near the mouth and the runoff at the head (Hosseini & Siadatmousavi, 2018).

The MRE is shallow (depth < 2m in most parts of the estuary), narrow (~ 150m wide) and meandering, leading to weak stratification (Simpson number ~0.2). The MRE exhibits a micro-tidal regime with a flood-dominated asymmetry near the mouth, where a 13.66-day periodic tidal asymmetry from the triad K1-O1-M2 is overcome by higher harmonics (Hosseini & Siadatmousavi, 2018). The same authors demonstrated that tidal wave propagation decreases from spring tide to neap tide, which was associated with a hypersaline runoff during the neap tide. However, the role of the salt-river flood could not be distinguished from the tidal weakness during the neap period, which hindered the propagation of the tidal wave. This study aims to quantify the hypersaline runoff required to obstruct tidal signals and salt transport to the Persian Gulf through various hypersaline runoffs.

In a freshwater lens estuary, the longitudinal density gradient is opposite to that of a salt-plug estuarine system. The water density increases in both the seaward and

landward directions of the freshwater lens. In contrast, in a salt-plug estuary, the water density decreases from the salt plug in both the seaward (similar to an inverse estuary) and landward (similar to a positive estuary) directions. This thesis also investigates the possibility of reversing longitudinal circulation cells between salt-plug and freshwater lens estuaries. Furthermore, the temporal variations in estuarine conditions from a positive state during wet months to salt-plug estuary in dry months are studied in the MRE.

The potential impact of rising sea levels on longitudinal salinity distributions in different estuarine states (positive, inverse, salt-plug, and freshwater lens estuaries) in the MRE is not well understood. This is a key area of uncertainty that is addressed in the thesis.

The Persian Gulf as a big inverse estuary

The PG is a shallow marginal sea and semi-enclosed basin located in a subtropical high-pressure region of the Middle East. This region is characterized by a hot and arid climate. As a result, the high evaporation rate of approximately 1.44 m/yr (Privett, 1959) exceeds the low precipitation of approximately 0.11-0.19 m/yr (Marcella & Eltahir, 2008), leading to the formation of high-salinity waters with salinity ranging from 38.5 psu to 41 psu (Al-Muzaini & Jacob, 1996).

This gulf connects to the Oman Sea and the Indian Ocean via the Strait of Hormuz (SOH), (see Figure 1). The Residual water exchange between the PG and the Indian Ocean results from an inverse estuarine circulation in the PG, whereby a net-inflow rate emerges to compensate for higher evaporation rates than freshwater inflows by precipitation and river discharges (Johns et al., 2003; Lorenz et al., 2020; Kämpf & Sadrinasab, 2006). The inverse estuarine flows are identified by the outflow of high-salinity (dense) deep PG water (PGW) mass, which is associated with an inflow of low-salinity Indian Ocean surface water (IOSW) at the SOH.

The PG exhibits a cyclonic circulation driven by halocline forces caused by the high evaporation rates (density gradient) associated with Coriolis forcing (Reynolds, 1993). The IOSW intrudes into the PG along the Iranian (northern) side, becoming more saline and denser through evaporation. This process produces the deep, dense PGW mass, which mainly outflows along the southern side of the SOH (Chao et al., 1992; Reynolds, 1993). The seasonally variable intrusion of the low-salinity IOSW into the PG is greatest in warm months, driven by a significant difference in density between the PGW in the interior of the basin and the oceanic water at comparable depths outside the PG (Swift & Bower, 2003).

Tides in the PG are mainly semi-diurnal and play a significant role in vertical mixing at the PG (Reynolds, 1993). Indeed, the PG is an energetic tidal basin in which the tidal range is usually larger than 1 m (Reynolds, 1993). A study by Azizpour et al. (2016) revealed that tides control flows at the SOH. The semi-diurnal and diurnal tidal constituents M2 and K1 were identified as the most significant contributors to those flows. Aboobacker et al. (2021) observed that the dominant wind in the PG is the northwest wind, with a typical duration of 3-5 days.

The density gradient-driven flows are considerably weaker than the magnitude of tidal velocities (Lardner & Das, 1991). When considering net (residual or time-averaged) flows, it can be seen that density gradients and winds exert a dominant influence over tidal residual flows, which are of negligible magnitude. The influences of tides and wind on the PG-circulation have already been the subject of extensive literature reviews. For example, Pous et al. (2013) noted that wind-driven circulation is more pronounced than the residual tidal flows in the PG. The same authors employed an idealized model without initial density gradient and thermohaline surface forcing, demonstrating that the wind-induced circulation driven by a dominant wind in the PG (northwesterly wind) comprises a cyclonic gyre along the Arabian coast and an anticyclonic one along the Iranian coast. Thoppil & Hogan (2010), using a non-tidal model, showed that wind stress forcing exerts a significant influence on the PG-general circulation. Their findings

indicated that winter northwesterly winds generated a flow of approximately 0.25-0.3 m/s in the vicinity of the Iranian coast. Pous et al., (2012) noted that residual currents induced by tides have a relatively weak influence (approximately 0.02 m/s) on the overall circulation. On the other hand, the strong tidal flows in the SOH facilitate the efficient mixing of the two water masses of the PGW and IOSW (Pous et al., 2012). In fact, the outflowing PGW can be modified by mixing across a density gradient that separates the deep PGW from the IOSW (Swift & Bower, 2003). The impact of tidal mixing on salinity fields and salt transports at the SOH is still lacking, which prompts us to investigate it at this strait.

A lot of scholarly attention has been focused on the issue of water exchanges through the SOH. The majority of these studies propose that the density gradient at the SOH is the primary driver of volume exchanges, as evidenced by the work of (Johns et al., 2003; Sadrinasab & Kämpf, 2004; Pous et al., 2015; Campos et al., 2020). Similarly, Swift & Bower (2003) suggested that the density field dominates the hydrodynamic circulation and long-term transport processes of water and salt in the gulf. However, the effects of wind and tidal forcings on the inflowing-outflowing volume transport through the SOH remain to be investigated.

The estimated inflow and outflow rates have been estimated to be approximately ±0.2 Sv. A higher inflowing (positive) volume transport results in an inflowing netflow rate of approximately +0.01 Sv. For example, the inflow, outflow and netflow rates were respectively estimated to be +2696 km3/yr (0.085 Sv), -2375 km3/yr (-0.075 Sv) and +321 km3/yr (0.010 Sv) by (Reynolds, 1993). In a similar vein, Campos et al. (2020) also proposed 0.272 Sv, -0.26±0.05 Sv, and 0.0122 as the corresponding volume exchanges.

The motivation behind this research is the current lack of scholarship on the role of tides on inflowing-outflowing volume transports. By considering the influence of tides on the inflow-outflow rates, it may be possible to improve the estimated inflow-outflow rates by approximately±0.2 Sv, as previous studies have largely focused on

density gradients and have computed the volume transport by considering residual (time-averaged) or non-tidal flows.

In addition to freshwater outflux by high evaporation and freshwater influx by low precipitation and river discharge, saltwater exchange through the SOH constitutes the water mass balance (the Knudsen relationship) in the PG. This thesis also examines the Knudsen relationship incorporating volume and salinity balances in the PG.

The density gradients induced by gravitational circulation drive the transport of salinity from saltier locations to fresher ones. Consequently, this type of salt transport can reverse from positive to inverse estuaries.

The primary river inflow is from the Shatt Al-Arab River at the PG head. Salinities in the vicinity of the Shatt Al-Arab mouth are typically below 35 psu, especially during the peak spring river flow. The PG's mean surface salinity is about 41 psu. The river discharge locally (or regionally in rare instances) affects the PG's hydrodynamics (Alosairi et al., 2019). The densest water with the highest salinity forms in the shallow water banks at the northwestern and southern coasts of the PG.

To the best of our knowledge, salinity distributions affected by wind and tidal forcings throughout the PG have rarely been investigated by earlier observational and numerical studies. This thesis aims to address this gap in knowledge by examining the role of tides on the PG salinity distribution. It provides a comprehensive understanding of PG hydrodynamics and a basis for the study of environmental management and sustainability.

Research questions and objectives

The objective of this thesis is to address the gaps (aforementioned in the background information) in understanding the hydrodynamics of salt-plug estuaries, the freshwater lens estuary of the MRE, and the inverse estuary of the PG. The main research questions that guide the study's objectives, are as follows:

- Salt-plug estuaries:
    1) What is the relative influence of density gradients and tidal forcing in producing a salt plug?
    2) How are lateral circulation cells formed landward and seaward of the salinity maximum zone?
    3) How does neap–spring variability affect longitudinal and lateral circulations at the salt plug?
- Freshwater lens condition of the Mond River Estuary:
    4) How can the MRE switch between a freshwater lens system and a salt-plug estuary during seasonal transitions?
    5) Do opposite longitudinal salinity patterns imply a reversal in dynamics between salt-plug and freshwater lens estuaries?
    6) What is the impact of sea level rise on the longitudinal salinity distribution in the MRE's estuarine systems?
- Inverse estuarine system of the Persian Gulf:
    7) What are the roles of tides in inflowing-outflowing volume transports through the SOH, especially on annual time scales?
    8) What is the relative influence of density gradients and tidal forcing on currents at the PG, particularly on exchange flows at the SOH?
    9) What role do tides play in the salinity distribution of the PG?

The responses to these queries will facilitate the acquisition of knowledge regarding the physical processes within the low-inflow estuaries, particularly regional PG system and its coastal areas, including the MRE. Studying the hydrodynamics of these low-inflow estuaries is also important for sediment transport, biogeochemical conditions, water quality, and assessing the impacts of climate change and anthropogenic pressures in these estuarine systems.

Approach and outline

The thesis examines the hydrodynamics of the PG and the MRE, which is located on the northern coast of the gulf. The Persian Gulf, characterized by high evaporation rates, behaves as an inverse estuary. The MRE exhibits significant seasonal variability, switching from positive and freshwater lens estuaries in wet months to salt-plug estuarine conditions during dry months. The intricate bathymetry and geometry of the MRE present significant challenges to the study of longitudinal and lateral circulations. To address this, we have conducted a second type of numerical experiment using an estuary with an idealized form and topography, namely a simple trumpet shape. This experiment enables the analysis of secondary flows in a salt-plug estuary in a simplified manner.

The hydrodynamical analysis employs the Semi-implicit Cross-scale Hydroscience Integrated System Model, SCHISM, (Zhang et al., 2016), based on unstructured horizontal grids and uses Reynolds-averaged Navier-Stokes equations and the Boussinesq approximation.

This thesis comprised of six chapters. Following this introductory section (Chapter 1) outlining the research questions and objectives, the three research papers are presented in Chapters 2 to 4. Paper 1 (Study I), Paper 2 (Study II), and Paper 3 (Study III) address the first (salt-plug estuaries), second (freshwater lens estuary), and third (the PG-inverse estuary) groups of the research questions , respectively.

The first paper (Study I) analyzes the physical characteristics and dynamics of salt-plug estuaries. It considers an idealized estuarine basin that is assumed to be located in close proximity to the MRE area. This assumption enables the model to incorporate actual atmospheric fluxes, including the high evaporation rates observed in the MRE region during dry months. Study I identifies two opposing longitudinal circulations in a salt-plug estuary. This is the first study to analyze lateral circulations and the competition between tidal forcing and density gradients in salt-plug estuaries.

Study II (Chapter 3) examines the temporal variations in estuarine conditions of the MRE through numerical modeling. This estuary can change from a positive estuary in wet months to a salt-plug estuary during dry months. The focus of Study II is on the hydrodynamics of a highly unsteady freshwater lens estuary based on both observations and model results. In order to model the impact of rising sea level on various estuarine systems (positive, freshwater lens, inverse, and salt-plug estuaries), Study II, also, evaluates the corresponding longitudinal salinity variations affected by a sea level rise.

Ultimately, the findings of Study III (Chapter 4) demonstrate that tidal currents and associated mixing play a pivotal role in the transport of inflowing-outflowing volume and salt in the SOH. This, in turn, affects the distribution of salinity in the PG. The study employs a range of numerical experiments with high horizontal and vertical resolutions to quantify the impact of tides on hydrodynamic conditions in the PG, in comparison to the influence of density gradients. This aspect has been largely overlooked in earlier observational and numerical studies.

The significance of the three study findings and their interrelationships are discussed in Chapter 5. This chapter also offers some suggestions for further research directions. The synthesis of the thesis is presented in the final chapter (Chapter 6). It includes a summary of the novelties across the three publications, and then provides an outlook on how the present research contributes to the advancement of science, particularly in the context of low-inflow coastal-regional estuaries in arid climates.

2 Study I: Salt-plug Estuarine Hydrodynamics

This chapter contains the first paper, published in Frontiers in Marine Science – Coastal Ocean Processes:

Hosseini, S.T., Stanev, E., Pein, J., Valle-Levinson, A. and Schrum, C. (2023). ***Longitudinal and lateral circulation and tidal impacts in salt-plug estuaries***. Front. Mar. Sci. doi: 10.3389/fmars.2023.1152625

Author contributions:

STH performed model analyses and wrote the manuscript. STH and JP developed the model set-up and different numerical experiments. STH, ES, JP and AVL contributed to the conception and design of the study. ES, AVL, and CS advised on the analysis of model results. All authors revised and approved the manuscript.

frontiers | Frontiers in Marine Science

TYPE Original Research
PUBLISHED 28 April 2023
DOI 10.3389/fmars.2023.1152625

Check for updates

OPEN ACCESS

EDITED BY
Carina Lurdes Lopes,
University of Aveiro, Portugal

REVIEWED BY
Alessandro Stocchino,
Hong Kong Polytechnic University,
Hong Kong SAR, China
Andrea Cucco,
National Research Council (CNR), Italy
Wei-Bo Chen,
National Science and Technology Center for Disaster Reduction (NCDR), Taiwan

*CORRESPONDENCE
Seyed Taleb Hosseini
seyed.hosseini@hereon.de

RECEIVED 28 January 2023
ACCEPTED 12 April 2023
PUBLISHED 28 April 2023

CITATION
Hosseini ST, Stanev E, Pein J, Valle-Levinson A and Schrum C (2023) Longitudinal and lateral circulation and tidal impacts in salt-plug estuaries. *Front. Mar. Sci.* 10:1152625. doi: 10.3389/fmars.2023.1152625

COPYRIGHT
© 2023 Hosseini, Stanev, Pein, Valle-Levinson and Schrum. This is an open-access article distributed under the terms of the Creative Commons Attribution License (CC BY). The use, distribution or reproduction in other forums is permitted, provided the original author(s) and the copyright owner(s) are credited and that the original publication in this journal is cited, in accordance with accepted academic practice. No use, distribution or reproduction is permitted which does not comply with these terms.

Longitudinal and lateral circulation and tidal impacts in salt-plug estuaries

Seyed Taleb Hosseini[1]*, Emil Stanev[1], Johannes Pein[1], Arnoldo Valle-Levinson[2] and Corinna Schrum[1,3]

[1]Institute of Coastal Systems - Analysis and Modeling, Helmholtz-Zentrum Hereon, Geesthacht, Germany, [2]Department of Civil and Coastal Engineering, University of Florida, Gainesville, FL, United States, [3]Institute of Oceanography, Center for Earth System Research and Sustainability, Universität Hamburg, Hamburg, Germany

This study presents a comparison of forcings between density gradient and tides in idealized funnel-shaped salt-plug estuaries. Three-dimensional numerical model results also examine longitudinal and lateral circulations. In salt-plug estuaries, a positive longitudinal estuarine circulation is observed landward of a salinity maximum zone or salt plug. Seaward of the salt plug, the estuary shows an inverse circulation cell. The longitudinal flows show a fortnightly variability inside the salt plug. Also, the salt plug is saltier in spring tides than in neap tidal cycles mainly owing to higher landward salt transport by tidal advection during the spring tides. The lateral circulation and divergence dv/dy have the influence of Coriolis acceleration. In the absence of Earth's rotation, the tidally averaged lateral circulations have nearly the same directions within the positive and inverse cells. Directions of lateral flow reverse in the salt-plug area. Inside this area, the lateral circulation also shows clear neap–spring variability, including downwelling cells during spring tides and upwelling in neap tides. The salinity maximum zone exhibits a vertically homogeneous condition particularly in meso-tidal salt-plug estuaries. Finally, this study introduces the threshold of "*log(tidal Froude number)=3*" (tidal forcing 3 orders of magnitude ≥ density gradients) for salt-plug estuaries as the condition under which the tidal forcing can overcome the density gradient, and consequently salinity inside the salt plug zone is reinforced by tides with a landward movement. This robust salinity maximum zone is also identified by a high Ekman number (*log(Ekman number)>0.25*).

KEYWORDS

salinity maximum zone, Ekman number, tidal Froude number, tidal advection, salt flux, Persian Gulf

1 Introduction

A salt plug or salinity maximum zone can form in an estuary when evaporation rates compare to river discharge (Valle-Levinson, 2010). If we have on one side the river and on the other side a salty ocean, it is normal to expect that, in the estuary, salinity will continuously decrease from the mouth to the head. A situation in which a salt plug forms is if evaporative losses are such that they do not add salt but extract fresh water from the estuary. A small river runoff can overcome the evaporation only close to the head of the estuary. This area thus develops typical gravitational circulation. The high evaporation results in waters that are saltier than waters in the open ocean with a maximum salinity zone. A salt plug separates positive gravitational circulation, landward of the salt plug, from inverse gravitational circulation seaward of the salt plug. An example of a salt-plug estuary was first given by Wolanski (1986) for the Alligator River Estuary in northern Australia. Other similar highly evaporative systems are the Gulf of Fonseca on the Pacific side of Central America (Valle-Levinson and Bosley, 2003), the bay of Malampaya Sound in Palawan in the Philippines (Cabrera et al., 2014), the Pasur River Estuary in southern Bangladesh (Shaha and Cho, 2016), and the Mond River Estuary on the northern coast of the Persian Gulf during summer (Ghaemi and Gholamipour, 2017). The latter belongs to the type of low-inflow estuaries in the category of "arid coasts" (Largier, 2010; Hosseini and Siadatmousavi, 2018). However, a salt plug can also form in typical positive estuaries without arid conditions, such as Barataria Bay, and in the Mississippi River Delta, in which freshwater pulses from the ocean into the bay may develop a salinity maximum zone (Juarez et al., 2020).

In estuaries, secondary (lateral) currents are perpendicular and up to 10% of the magnitude of axial flows (Rozovskii, 1957; Geyer, 1993; Chant, 2010). Despite its relatively small magnitude, secondary circulation greatly impacts estuarine dispersion (Chant, 2010). Li et al. (2014) specified at least four important mechanisms that drive lateral circulation in positive straight estuaries: (1) differential advection of along-channel or longitudinal density (salinity) gradients (Nunes and Simpson, 1985, Lerczak and Geyer, 2004, Li et al., 2014), (2) cross-channel variation in mixing (Chant, 2010) or boundary mixing on a sloping bottom (Phillips, 1970; Wunsch, 1970; Chen and Sanford, 2009; Li et al., 2014), (3) Ekman forcing (Johnson and Ohlsen, 1994; Ott and Garrett, 1998; Scully et al., 2009; Chant, 2010; Huijts et al., 2011; Li et al., 2014), and (4) interactions between barotropic tides and lateral variations in bathymetry(Li and O'Donnell, 1997; Li and Valle-Levinson, 1999; Khosravi et al., 2018). In curved channels, centrifugal accelerations represent a fifth mechanism for secondary circulation (Chant, 2010; Pein et al., 2018; Kranenburg et al., 2019).

In the absence of Coriolis acceleration and channel curvature, differential advection in positive estuaries is considered the main mechanism driving estuarine secondary flows (Chant, 2010). The analysis of differential advection of longitudinal salinity gradients is of utmost relevance in this study. Following Chant (2010) and considering only mechanisms that can generate the lateral salinity gradients associated with secondary circulations, the tendency (the time rate of change) of lateral salinity gradients ($\frac{\partial}{\partial t}\frac{\partial s}{\partial y}$) can be approximated as

$$\frac{\partial}{\partial t}\frac{\partial s}{\partial y} = -\frac{\partial u}{\partial y}\frac{\partial s}{\partial x} - \frac{\partial w}{\partial y}\frac{\partial s}{\partial z} + \frac{\partial}{\partial y}\frac{\partial}{\partial z}\left(K_v \frac{\partial s}{\partial z}\right) \quad (1)$$

where s and t are salinity and time, respectively, y is the lateral (cross-channel) direction, u and w are the along-channel or longitudinal (x) and vertical (z) flows, respectively, and K_v is the vertical eddy diffusivity of salt. The first term on the right-hand side of equation (1) describes the mechanism of differential advection in which the lateral shear in the longitudinal velocity ($\frac{\partial u}{\partial y}$) acts on the longitudinal salinity gradient ($\frac{\partial s}{\partial x}$) to generate the lateral salinity gradients and thus secondary circulations. The second term reveals the tilting of vertical stratification by lateral variability in vertical motion. This mechanism (the second term) requires the existence of secondary circulations and typically acts to shut down the secondary flows. The third term on the right-hand side of equation (1) produces lateral salinity gradients by lateral variations in vertical mixing. This mechanism usually plays an insignificant role in driving lateral circulations in estuaries (Lerczak and Geyer, 2004, Chant, 2010).

In contrast to the case of positive estuaries, there are relatively few studies of salt-plug estuaries (Wolanski, 1986; Valle-Levinson and Bosley, 2003; Valle-Levinson, 2010; Valle-Levinson, 2011; Cabrera et al., 2014, Shaha and Cho, 2016, Juarez et al., 2020; Mariani et al., 2022). To the best of our knowledge, no study has assessed the relative influence of density gradients and tidal forcing in producing a salt plug, and lateral circulations in the salt-plug estuaries, which are the main objectives here. We also consider the relative contribution of tidally averaged lateral and longitudinal flows to drive surface and bottom convergences and their linkage to the zone of maximum salinity. These main objectives are addressed with process-oriented numerical simulations in an idealized semienclosed basin with semiarid climate, where evaporation rates are much higher than precipitation values.

The idealized model investigates the influence of various tidal forcings on longitudinal and lateral circulations in salt-plug estuaries. Numerical experiments yield results that place the salinity maximum zone in terms of non-dimensional parameter space and salt flux terms throughout the estuary. Results also depict how symmetric lateral circulations are modified landward and seaward of the salinity-maximum zone; particular focus is placed on the neap–spring variability in the longitudinal and lateral circulations at the salinity-maximum zone.

The paper is structured as follows. In Section 2, we present the methods, including the model description and setup as well as a decomposition of total salt flux in the estuary that is used to analyze the model results. The results are presented in Section 3, addressing longitudinal and lateral circulations in salt-plug estuaries including their variations in a spring-neap tidal cycle. Section 4 discusses three salient points. First, longitudinal and lateral divergences are discussed in term of dynamical depths (Ekman number). Second, the relative influence of forcing from tidal versus density gradient in driving the salinity-maximum zone is discussed in terms of the tidal Froude number and of salt-flux terms. Third, salt-plug estuaries are

cast in a general dynamic framework for semienclosed basins (Valle-Levinson, 2021). Finally, the conclusions are given at the end.

2 Method

2.1 Model description

The semi-implicit cross-scale hydroscience integrated system model (SCHISM, Zhang et al. (2016)) is used to investigate the hydrodynamics of salt-plug estuaries. SCHISM is a three-dimensional (3D) unstructured-grid numerical model that is based on the Reynolds-averaged Navier–Stokes equations with hydrostatic and Boussinesq approximations. These equations are supplemented by the turbulence closure equations based on the generic length scale (GLS) parameterizations of (Umlauf and Burchard, 2003).

This model has been used to study the dynamics of the German Bight estuaries, that is, the estuaries of the Ems, Weser and Elbe Rivers(Stanev et al., 2019), as well as idealized estuaries (Pein et al., 2018). Further details regarding the model and some applications are given in those studies.

2.2 Idealized basin and model setup

An idealized symmetrical cross-channel topography is used to investigate the hydrodynamics of salt-plug estuaries (Figure 1A). The morphology represents a funnel-shaped straight estuary with exponentially converging width from mouth to head (see, for example, (Ensing et al., 2015)). In a Cartesian coordinate system, where the x-axis points from the mouth (x = 0) to the head of the estuary (x = 100 km), the width W decreases exponentially:

$$W(x) = w_0 \exp(-\frac{x}{L_x}) \quad (2)$$

where w_0 and L_x are the width at the mouth (12 km) and the convergence length scale (30 km), respectively. The width of the estuary decreases to ~100 m at the head. The maximum depth at the estuary mouth on the main axis is 20 m (Figures 1A, B). This maximum depth decreases linearly with a rate of 0.25 m/km up to 36 km of the mouth and then with a rate of 0.11 m/km between 36 km and the estuary head (see Figure 1B).

The computational grid is represented by 4180 triangular elements constructed from 150 grid points in the longitudinal direction and 15 grid points laterally (2250 points in total). The resolution of this grid ranges from 2,000 m at the marine open boundary to 10 m at the estuary head. The idealized basin uses 25 sigma layers in the vertical direction.

The location of this idealized funnel-shaped estuary is around 28°N and 51°E, corresponding to the northern coast of the Persian Gulf (Figure 1A). Realistic atmospheric forcing ensures an evaporation rate commensurate with arid coastal conditions (Largier, 2010). This geographic area of the idealistic estuary is selected because it is close to the location of the Mond River Estuary, which behaves as a slat-plug estuary in the warm months (Ghaemi and Gholamipour, 2017).

All numerical simulations are performed for two years (from January 2013 to December 2014), in which atmospheric forcing uses hourly meteorological data from the European Centre for Medium-Range Weather Forecasts (ECMWF, https://cds.climate.copernicus.eu). Wind forcing was disabled to avoid additional complications to the idealistic circulation. Furthermore, temperature and salinity values at the open boundary were taken from the daily reanalysis data of the Persian Gulf provided by the Copernicus Marine Environment Monitoring Service (CMEMS, https://resources.marine.copernicus.eu) during 2013-2014 (730 days).

Eleven different numerical experiments (EXP1-EXP11) served to identify the dynamic differences between various salt-plug estuaries, typical of low latitudes, and to establish canonical patterns of longitudinal and secondary circulations (see Table 1). A low river inflow of 2 m^3/s was prescribed at the head of the estuary in all EXP1-EXP11. Additionally, in all experiments, the salinity of the river water was set to zero. The Coriolis force was turned off in EXP1-EXP3 and on in the other eight experiments (EXP4-EXP11). In order to investigate the influence of Coriolis on secondary circulation, the results of EXP1 and EXP2 are compared with the corresponding experiments EXP6 and EXP8 (see Table 1).

Except for EXP3 and EXP11, tidal forcing was prescribed as the M2 tide only with different amplitudes between 0 m and 1.5 m (see Table 1) to assess the impact of tidal forcing on the salt-plug dynamics. Experiments EXP3 and EXP11 aimed to study the response of the salt plug to spring–neap tidal variability. The tidal forcing in EXP3 and EXP11 used 10 tidal constituents: Q1, O1, P1, S1, K1, N2, M2, S2, K2 and M4 (see Table 2 and Figure 1C). Tide data were taken from the Danish Hydraulic Institute (DHI) global tidal model (Cheng and Andersen, 2010), as Table 2 shows. The amplitude of 0.465 m is selected in EXP1 and EXP6 as it equals M2 amplitude from the 10 tidal components at the approximate experiment location (51.2°E, 28.14°N). Time- (tidally-) averaged model results were obtained from model outputs during 28 days in the summer (20 July - 16 August) of 2014.

We used the idealized funnel-shaped basin to consider different tidal forcings in completion with density gradients. The limitations of this study are related to the simplified geometry used. But we are interested in processes, rather than particular systems. Future efforts shall concentrate in examining estuaries with different shapes and geometries.

2.3 Salt flux decomposition in the idealized salt-plug estuary

High evaporation rates (as in the northern coast of the Persian Gulf during the summer), together with the low river inflow (2 m^3/s), tend to create a salt plug in the idealistic basin. Thus, there are two areas of relatively lower salinity on both sides of the salt plug. Changing forcings in EXP4-EXP11 should elucidate the competition between density gradient and tidal forcing to change

10.3389/fmars.2023.1152625

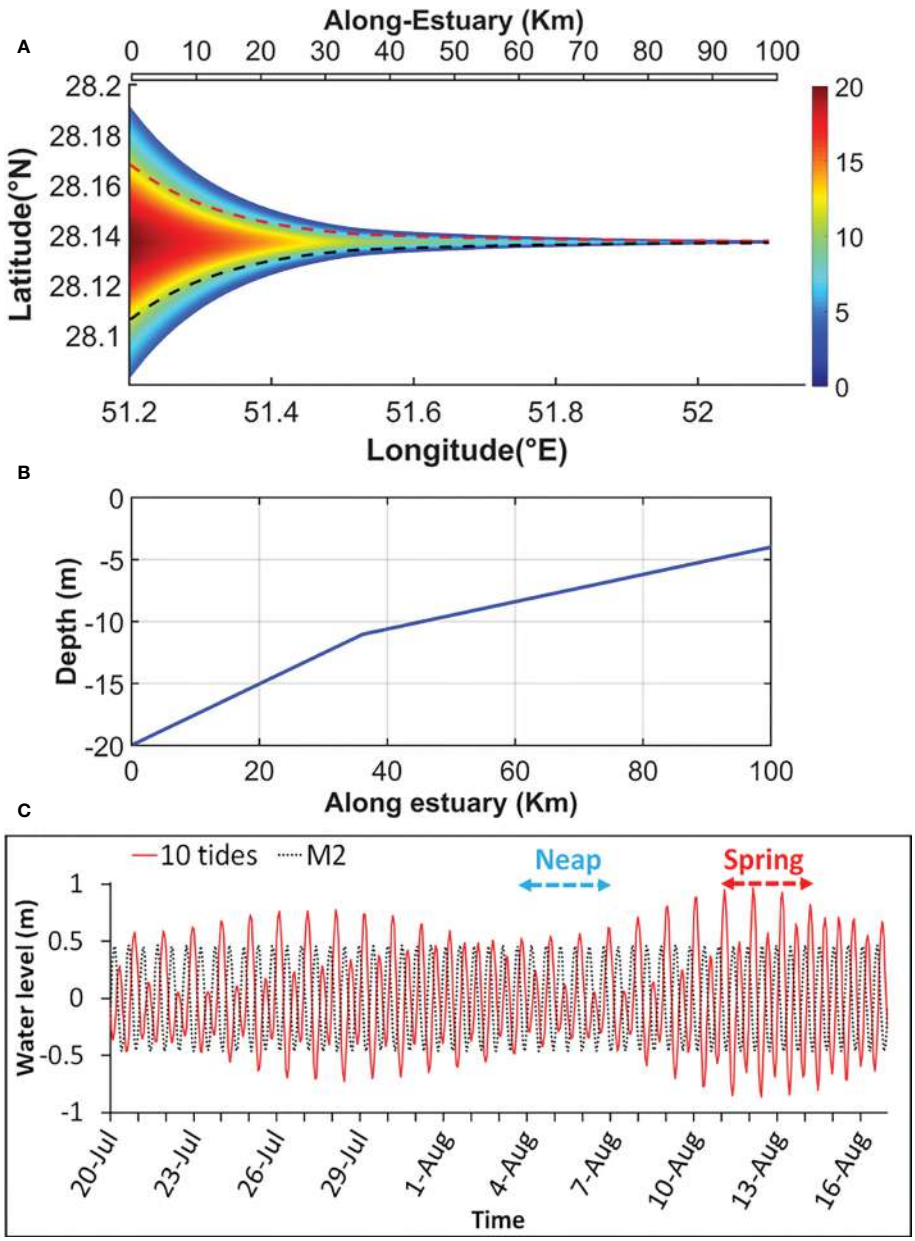

FIGURE 1
(A) The bathymetry (m) of the idealized basin. The red and black dashed lines show the two symmetrical northern and southern transects between the main axis and the northern and southern coasts, respectively. **(B)** Along-channel depth variation in the idealized estuary used in numerical simulations. **(C)** Two 28-day time series of water levels depict the open boundary conditions: only M2 tide in EXP1 and EXP6, and 10 tidal constituents in EXP3 and EXP11. Two 75-hour periods during neap and spring tides in EXP3 are shown by the two blue and red double arrows, respectively, during which average model states are analyzed.

the longitudinal salinity structure in the basin, especially at the salinity-maximum zone.

The instantaneous (time-varying t) total salt flux $F_s(t)$ at each one of the 150 cross-sections along the estuary was calculated as:

$$F_s(t) = \sum_{j=1}^{15}\sum_{k=1}^{25} U(\mathrm{j,k},t)S(j,k,t)A(j,k,t) \tag{3}$$

where j and k represent the number of cells at cross-sectional and vertical directions, respectively. In fact, the idealized basin includes 150 cross-sections (longitudinal grid points) and 15 lateral grid points (j) in 25 sigma layers (k). U, S and A are the longitudinal velocity, salinity and area of each cell located at the cross-section. Also, the tidally averaged total salt flux $\langle F_s(t) \rangle$ is given by:

$$\langle F_s(t) \rangle = \langle \sum_{j=1}^{15}\sum_{k=1}^{25} U(j,k,t)S(j,k,t)A(j,k,t) \rangle \tag{4}$$

in which the brackets $\langle\rangle$ identifies the tidal-averaged value. In order to separate the contribution of different forcings to the salt fluxes, the instantaneous $U(j,k,t)$ and $S(j,k,t)$ can be decomposed into the three components: (1) cross-sectionally and tidally

TABLE 1 Summary of the idealized salt-plug estuarine experiments.

Experiment	Tide	Tidal Amplitude (m)	Coriolis Force
1 (Reference)	M2	0.465	Not
2	M2	1	Not
3	10 components	0.92 in Spring tide 0.52 in Neap tide	Not
4	M2	0	Yes
5	M2	0.25	Yes
6	M2	0.465	Yes
7	M2	0.75	Yes
8	M2	1	Yes
9	M2	1.25	Yes
10	M2	1.5	Yes
11	10 components	0.92 in Spring tide 0.52 in Neap tide	Yes

averaged u_a and s_a, (2) tidally averaged and cross-sectionally varying u_e and s_e, and (3) both cross-sectionally and tidally varying u_t, s_t, (Lerczak et al., 2006; Aristizábal and Chant, 2015). The three components of velocity define as equations (5), (6), and (7). The salinity decomposition also produces analogous to these equations.

$$u_a = \frac{\langle \sum_{j=1}^{15}\sum_{k=1}^{25} U(j,k,t)A(j,k,t) \rangle}{\langle \sum_{j=1}^{15}\sum_{k=1}^{25} A(j,k,t) \rangle} \tag{5}$$

$$u_e(j,k) = \frac{\langle U(j,k,t)A(j,k,t) \rangle}{\langle A(j,k,t) \rangle} - u_a \tag{6}$$

$$u_t(j,k,t) = U(j,k,t) - u_e(j,k) - u_a \tag{7}$$

TABLE 2 The ten tidal constituents extracted from the DHI global model (Cheng and Andersen, 2010) at 51.2°E and 28.14°N used in EXP3 and EXP11.

Tidal component	Amplitude (m)	Phase (deg)
M2	0.465	61.26
S2	0.175	111.08
K1	0.208	204.82
O1	0.141	171.26
N2	0.100	35.91
P1	0.060	203.61
K2	0.045	99.13
Q1	0.028	157.90
M4	0.016	35.97
S1	0.013	338.00

Then, $\langle F_s(t) \rangle$ (equation 4) with neglecting interaction terms yields from the components (equations 5-7) as equation (8) (Lerczak et al., 2006; Aristizábal and Chant, 2015).

$$\langle F_s(t) = u_a s_a \sum_{j=1}^{15}\sum_{k=1}^{25} \langle A(j,k,t) \rangle + \sum_{j=1}^{15}\sum_{k=1}^{25} [u_e(j,k)s_e(j,k)] \langle A(j,k,t) \rangle + \sum_{j=1}^{15}\sum_{k=1}^{25} \langle u_t(j,k)s_t(j,k,t)\, A(j,k,t) \rangle + interactions \tag{8}$$

Generally, the advective salt flux (the first term on the right-hand side of equation 8) is mainly related to river discharge transport, but includes other contributions from meteorological forcing like wind (Valle-Levinson, 2022). Here, the advective term consists of the low-river inflow (2 m^3/s) and longitudinal advection from the tidal residual flows (without wind forcing).

The sheared salt transport (the second term on the right-hand side of equation 8) is driven by exchange flows of estuarine circulation (Valle-Levinson, 2022), or by longitudinal density (salinity) gradients (Lerczak et al., 2006).

The third term on the right-hand side of equation (8) indicates the salt transport by tidal pumping that is determined by the covariance between tidal flows and tidal oscillation in salinity. Therefore, this salt flux is related to the phase difference between the longitudinal tidal velocity and salinity. When the salinity and tidal currents are 90° out of phase (are in quadrature), their covariance will be zero (or near zero) and consequently the relevant tidal salt flux tends to zero. In fact, the 90° phase difference is exclusively imposed by longitudinal advection from the tidal flows where the sheared salt transport (induced by gravitational circulation) overcomes tidal pumping salt flux. On the other hand, the salt flux by tidal pumping strengthens when the longitudinal velocity and salinity become out of quadrature under increased processes like tidal mixing and lateral advection. It suggests that the tidal pumping term plays an important role in contributing the net salt flux when salinity extremes occur at time of maximum tidal flood or ebb flows (Aristizábal and Chant, 2015; Valle-Levinson, 2022). In this study, the tidally averaged total salt flux is calculated using Equation (4). Also, Equation (8) is used to compute the contributions from advective, sheared, and tidal pumping salt transports in the tidally averaged total salt flux.

3 Results

3.1 Longitudinal residual circulation in salt-plug estuaries

3.1.1 Basic properties

The time-averaged axial salinity and its longitudinal gradient ($\frac{\partial s}{\partial x}$) in the reference scenario (EXP1, see Table 1) demonstrate a typical salt-plug estuary. The salinity in the salt plug, which is in the zone of maximum salinity, is higher than 41.5 between 40 km and 60 km (Figures 2A, D). The zero-value of $\frac{\partial s}{\partial x}$, at ~50 km (Figures 2A, B), identifies the position of the salinity maximum. Two estuarine segments (cells) dominate the residual circulation pattern

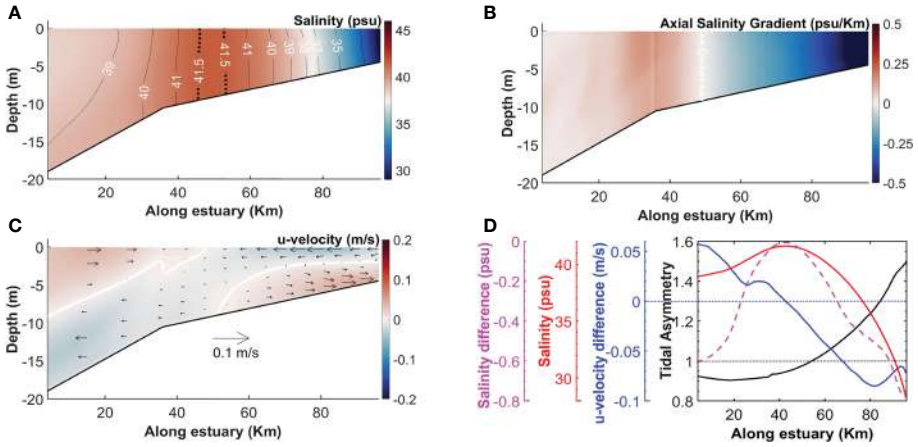

FIGURE 2
Along-channel profiles of time-averaged salinity **(A)**, axial salinity gradients ($\frac{\partial s}{\partial x}$) **(B)**, and axial velocity **(C)** in EXP1. The depth-averaged tidal current asymmetry along with the time-averaged surface and bottom differences in axial velocity, depth-mean salinity, and surface and bottom differences in salinity are plotted in **(D)** with different lines. The white dotted line in **(B)** is zero- $\frac{\partial s}{\partial x}$, indicating the border between two estuarine segments. White lines in **(C)** represent the positions of zero-velocities. The landward direction in the velocity differences is positive in **(D)**.

(Figure 2C). In the segment with inverse gravitational circulation, seaward of the plug, surface salinity increases from the mouth to the salinity maximum. Typical gravitational circulation is observed in the upper estuary between the head and the salt plug. In the maximum salinity zone, the mean axial flow nearly cancels out, and vertical stratification is weakest (see Figure 2A). This is consistent with the convergence of surface velocities and the divergence of bottom flow at this area.

The surface-to-bottom salinity difference (Figure 2D) provides the positioning of the salt plug. Exactly at the position of the minimum salinity difference, with practically no stratification in EXP1, the surface to bottom axial velocity difference is also zero. The dominance of well-mixed conditions in this area identifies the transition between positive and negative gravitational circulation cells. The change in the sign of the velocity-difference curve (blue line, Figure 2D) represents the changing sense of the circulation cells.

Further insights are drawn by the axial tidal current asymmetry, expressed as the ratio between maximum flood and maximum ebb depth-mean velocities (black line, Figure 2D). A ratio higher than 1 indicates flood-dominated asymmetry. According to this ratio, the direction of tidal current asymmetry changes close to the salt plug so that ebb-dominated asymmetries appear at the inverse gravitational circulation segment while flood-dominated asymmetries develop at the positive gravitational circulation portion.

3.1.2 Fortnightly variations

We extend EXP1 to EXP3 by forcing with ten tidal constituents (spring–neap scenario in Table 1). Results show that the residual circulation after 28 days (Figure 3A) is similar to that from EXP1 (Figure 2C). Two 75-hour intervals during this 28-day period represent neap tide (from 04 August to 07 August 2014) and spring tide (from 11 August to 14 August 2014). Each subperiod covers six M2 cycles (see both periods in Figure 1C). The residual flow for those periods (Figures 3C, E) show that spring-tide patterns resemble the 28-days mean (compare Figures 3A, E). The spring tide residual flow displays seaward displacement of the surface outflow in the positive gravitational circulation that extends throughout the water column (from the surface to the bottom) at the salt plug zone (~50 km) (see Figure 3E). Also, the areas of landward inflow in the spring tide, both surface and bottom, shrink and separate in comparison with those of neap tide (Figure 3C), retreating toward both ends of the estuary (see Figure 3E). In contrast, the inflow areas in neap tides are connected at the salt-plug location (around 50 km in Figure 3C). In general, however, flow patterns in spring and neap tides show essentially the same features. In both cases, the salt plug is in the area that connects (neap) or separates (spring) the residual inflows.

Considering surface longitudinal residual flows across the estuary around the salt plug (36 km – 60 km), shadowed by surface salinity (Figures 3B, D, F), also confirms that the landward surface flows intrude into estuary up to ~km 43 in both averaged 28-day (Figures 3A, B) and spring tide (Figures 3E, F). While the residual landward flows exceeds 50 km in the neap tide (Figures 3C, D). The salt plug is slightly saltier in the spring tide than in the neap tide (see Figures 3D, F), owing to higher tidal mixing during spring tides (Geyer and MacCready, 2014) that is associated with higher landward salt transport by tidal advection in the spring tide. Also, tidal pumping of salt shows a landward direction in the spring tide contrary to the neap tide (see section 4.2).

From the different residual flow fields at the salinity maximum zone (around 50 km) in the spring-neap transition, it is reasonable to expect that dissimilar lateral shears in the axial velocities $\frac{\partial u}{\partial y}$ and

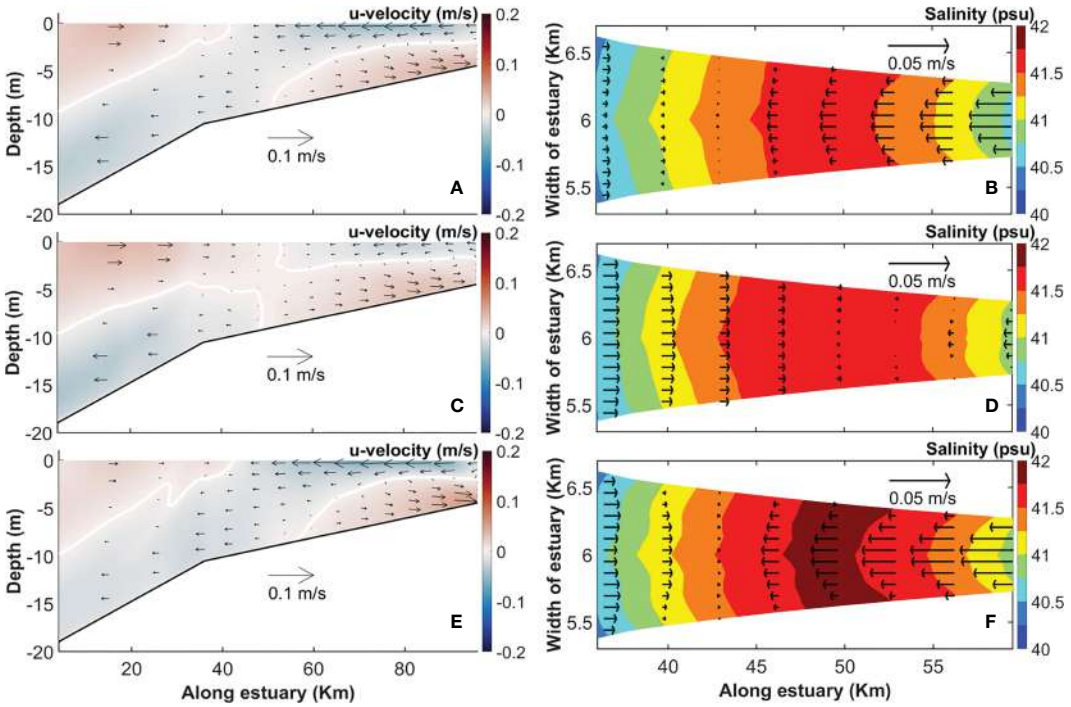

FIGURE 3
Along-channel profiles of axial velocity in EXP3 (see Table 1). Averaging is for the full neap–spring cycle of 28 days **(A)**, for six M2 periods during neap tide from 04 August to 07 August 2014 **(C)**, and for spring tide from 11 August to 14 August 2014 **(E)**. 2D distribution of surface axial-velocity and salinity corresponding with the periods of **(A, C, E)** are respectively presented in **(B, D, F)**.

the axial change in salinity should lead to differential advection $\frac{\partial u}{\partial y}\frac{\partial s}{\partial x}$ (equation 1), resulting in generation of different lateral flows. Thus, fortnightly variations in lateral flows should be evident around the salt-plug region, as described in the following section.

3.2 Lateral circulation in salt-plug estuaries

3.2.1 The impact of earth's rotation

Time-averaged lateral shears of along-channel velocities ($\frac{\partial u}{\partial y}$) in the inverse estuarine segment (at 25 km) have opposite signs at the surface to those in the positive estuarine segment (at 75 km) (Figures 4A, E). Also opposite is the sign of the along-channel salinity gradients ($\frac{\partial s}{\partial x}$) on both sides of the salt plug (see Figure 2B). Therefore, their product ($\frac{\partial s}{\partial x}\frac{\partial u}{\partial y}$), representing differential advection, has the same sign in the two estuarine segments. Differential advection thus builds converging flows at the surface in the deep channel (Figures 4B, F). Lateral circulation cells are rather symmetric because the model setup is symmetric (no Coriolis force or asymmetric bathymetry in EXP1). Although the cells show similar overall structure at the two cross-sections, they have marked differences along the channel in terms of the proportions occupied by positive or negative flows.

The impact of Earth's rotation on the salinity field is straightforward as the maximum salinity zone is displaced to the right, looking seaward. More revealing is that the values of $\frac{\partial u}{\partial y}$ in EXP6 at 25 km display asymmetries (compare Figures 4A, C). At the narrow part of the channel (75 km), the asymmetries in $\frac{\partial u}{\partial y}$ are less evident (compare Figures 4E, G). However, the structure of the lateral velocities are changed along both sections, especially in the upper layers (compare Figures 4B, D, as well as Figures 4F, H) after activating Coriolis accelerations. The section close to the mouth is distinguished by a near-surface diverging cell (Figure 4D).

Near the bottom, on the other hand, lateral flows change little from EXP1 (without Coriolis accelerations, Figures 4B, F) to EXP6 (with Coriolis force, Figures 4D, H) in both cross-sections. In fact, experiments with and without Coriolis (EXP1 and EXP6) reveal that Coriolis deflection alters lateral circulation even in narrow cross-sections near the head of the estuary, reproducing cross-sectional flow asymmetries such as those reported by (Valle-Levinson et al., 2003) and (Chant, 2010). The bottom line is that asymmetries tend to be enhanced at the surface and reduced near the bottom (see Figure 4). This is consistent with the results of (Johnson and Ohlsen, 1994). Using laboratory experiments over a simulated ocean channel ("trough"), they demonstrated that the surface secondary (Ekman) flows vary along the channel, while the flows in the bottom Ekman layer almost have the same structure along the channel. Moreover, (Friedrichs and Valle-Levinson, 1998) showed that secondary circulations driven by Coriolis forcing are stronger at the surface and weaker near the channel bed,

considering positive estuaries at the dominant tidal frequency. Both secondary and longitudinal tidal currents were surface intensified, which suggests that Coriolis accelerations cannot be entirely balanced by a barotropic pressure gradient.

Thus, in the absence of Coriolis acceleration, the dominant dynamic mechanism driving lateral flows is differential advection. However, Coriolis influences lateral circulations, as diagnosed with the Ekman and Kelvin numbers (Garvine, 1995), (Table 3).

Table 3 presents these number values for the two cross-sections of 25 km and 75 km from EXP6. Since both the width and depth decrease from the estuary mouth to the head, the Coriolis impact (Kelvin number) increases quite substantially with decreasing distance to the mouth (compare the two Kelvin numbers in Table 3). In contrast, the Ekman number (frictional effects) increases with decreasing distance to the head (see the Ekman number values in Table 3).

TABLE 3 The time-averaged values of nondimensional vertical Ekman and Kelvin numbers in the cross-sections at 25 km and 75 km in EXP6.

Cross-section	Kelvin	Ekman
25 km	0.9230	0.0160
75 km	0.2939	0.6395

3.2.2 Influence by differential advection

3.2.2.1 Along-channel evolution

The cross-channel sections in Figure 4 are different enough to question any conclusions on secondary flows drawn from only two sections. Therefore, lateral velocities along the northern along-estuary line (from Figure 1A) provide a relatively more comprehensive picture (Figure 5A). This line's position, away from the thalweg, should illustrate robust lateral velocities. Because of the symmetric flow structures in EXP1, the southern along-estuary line mirrors the northern line (not shown).

Over most of the estuary, the lateral circulation in EXP1 is typically structured in two symmetric cells, one north (see Figure 5A) and one south of the thalweg. The northern cell is formed in the inverse estuarine segment, between the mouth and the salt plug. In this cell, lateral near-surface velocities converge

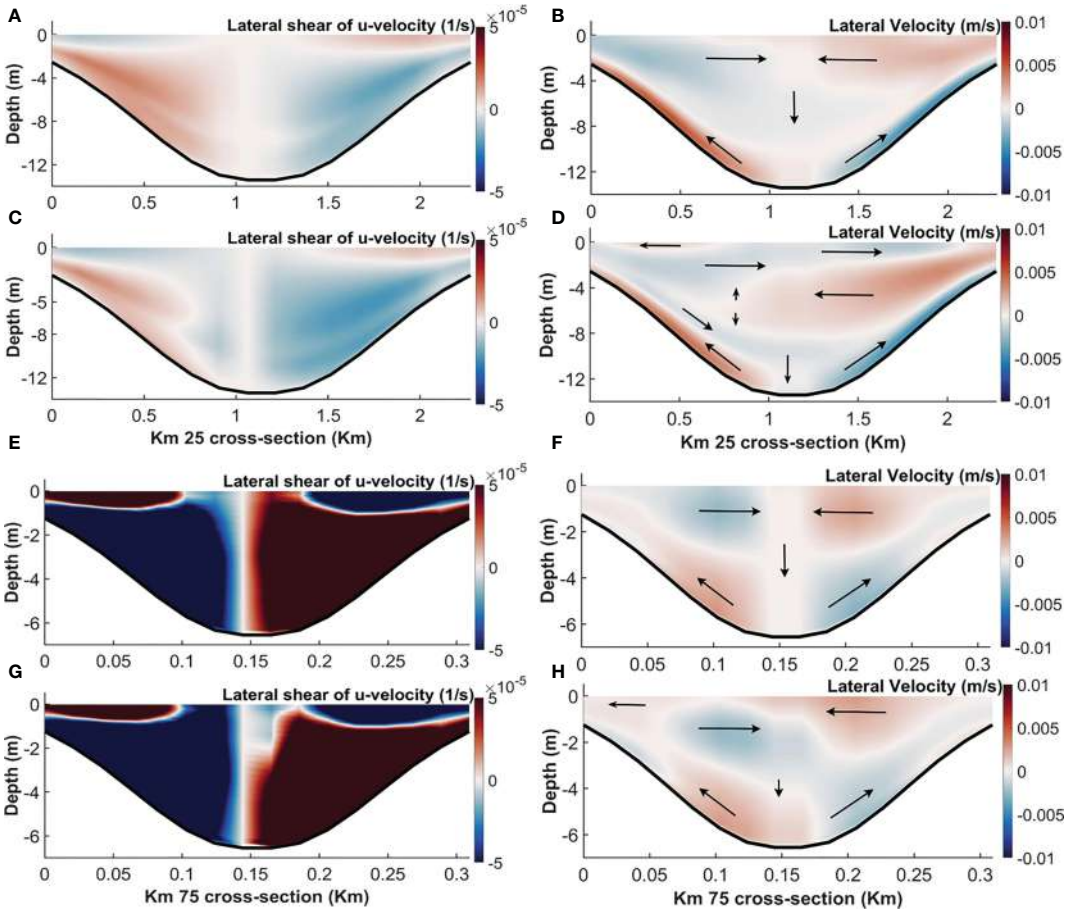

FIGURE 4
Time-averaged lateral shear of along-channel velocities ($\frac{\partial u}{\partial y}$) **(A, C, E, G)** and lateral velocities **(B, D, F, H)** along the cross section at 25 km **(A–D)** and 75 km **(E–H)** from the mouth in EXP1 **(A, B, E, F)** and EXP6 **(C, D, G, H)**. Red and blue colors in lateral velocities represent leftward and rightward velocities, respectively, looking into the estuary.

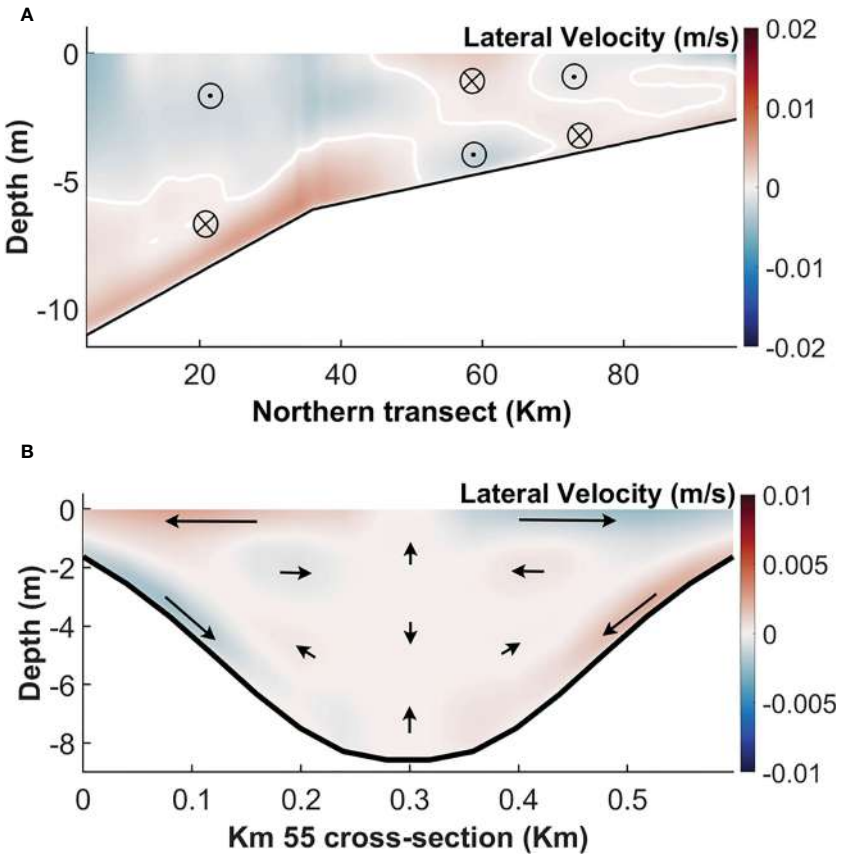

FIGURE 5
Time-averaged lateral velocities **(A)** along the northern transects shown in Figure 1, and **(B)** along the cross section at 55 km from the mouth in EXP1. Red and blue colors in **(A)** represent northward and southward velocities, respectively. Leftward and rightward velocities looking into the estuary are identified in **(B)** by red and blue colors, respectively.

toward the thalweg and diverge at the bottom. In the positive estuarine segment, the residual lateral flow is more complex. Close to the head of the estuary (>70 km in Figure 5A), there are two cells one above the other. At the salt-plug zone, between 50 km and 70 km, the directions of lateral velocities reverse. Actually, the pattern illustrates a divergent surface cell at 55 km (also shown in Figure 5B). This is in opposition to the convergence of axial velocities in the same area (Figure 2C), that is the surface axial inflow and outflow approaching each other (the surface longitudinal convergence occurs) at the salt plug zone (see km 50 in Figure 2C). Conversely, the bottom longitudinal flows diverge from each other in this zone.

3.2.2.2 Spring-neap lateral flows and salinities at the salt plug

The time-average lateral flows at 50 km in neap and spring tide show similar structure across the basin, but with opposite signs (Figures 6A, E; see the neap and spring averaging periods in Figure 1C). During the neap period, the lateral flow shows circulation cells conducive to upwelling in the deep channel (Figure 6A). Conversely, spring tides lateral flows illustrate downwelling in the deep channel (Figure 6E). As a result, the time-averaged salinities are also redistributed by the relevant lateral circulations across the section in the neap and spring tides (Figures 6B, F). The upwelling flows in the center channel lift isohalines in the neap tide (Figure 6B), whereas lying down lateral flows depress isopycnals in the center channel, creating a saddle shape in the isohalines associated with the upwelling flows in both sides of shallow shoals during the spring tide (Figure 6F).

A basic difference between spring-neap secondary circulations is that lateral circulation is stronger during neap than spring tide because of weaker mixing (Geyer and MacCready, 2014), (also see isohalines at the thalweg in Figures 6B, F). Actually, under weak stratification, such as in the salt-plug zone (see Figures 2D, 6B, F), the dynamics are consistent with the results of (Geyer, 1993). However, as stratification increases, the second term of the right-hand side of equation (1), $(\frac{\partial w}{\partial y}\frac{\partial s}{\partial z})$, tilts the halocline with the secondary flows. This advective

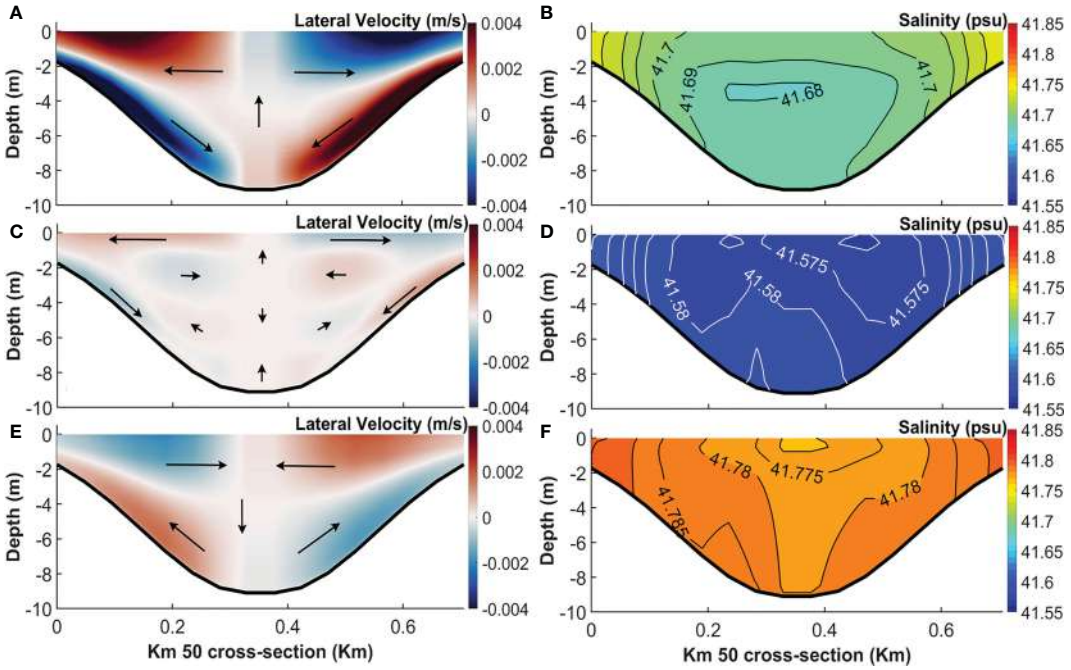

FIGURE 6
The time-averaged lateral velocities **(A, C, E)** and salinities **(B, D, F)** along the cross section at 50 km during neap tide **(A, B)**, full neap–spring cycle **(C, D)** and spring tide **(E, F)** from EXP3. Red and blue colors in velocities identify leftward and rightward velocities, respectively, looking into the estuary.

term produces a baroclinic pressure gradient that opposes the lateral shear mechanism and consequently tends to shut down the secondary flows, consistent with Chant, 2010.

This result agrees with the study by (Lerczak and Geyer, 2004), which claims that the structure of the secondary circulations could change in the transition from neap to spring tides. At the salt-plug zone, it actually reverses.

On the other hand, the secondary circulations during the full neap–spring period (Figure 6C) show more similarity with the neap than with the spring period. The secondary circulations redistribute isohalines in the vertical shape with upwelling them near the surface in the center channel during the full neap–spring period (Figure 6D).

3.3 Responses to increasing tidal amplitude

This section presents the relative influence of tidal forcing vs density gradients on the salt-plug position in the estuary. Eight experiments (EXP4 to EXP11) that portray, through the temporally and depth-averaged axial salinity, that the salt plug is not only enhanced with tidal forcing but it is also transported landward at tidal amplitudes higher than 1 m (the meso-tidal estuaries of EXP8-EXP10, Figure 7A and Table 4). While the salt plug moves landward from zero-tide (EXP4) to EXP5, it then moves seaward in microtidal experiments EXP5, EXP6 (~0.5 m tide), EXP11 (the spring-neap experiment) and EXP7 (with tidal amplitude of 0.75 m) (see Table 4), with a change in salinity of only around 1 psu at the salt plug (see Figure 7A). These responses are attributed to the competition between tides and density gradients dominating the momentum balance, and the prevalence of tidal pumping or sheared transport in driving the salt balance.

For the momentum balance competition, the densimetric tidal Froude number (Fr_T) (Figure 7B) is used according to the study of (Valle-Levinson, 2021) as $Fr_T = \frac{L_\rho}{L_T}\frac{U_T^2}{\acute{g}D}$ in which U_T is the along-basin tidal current amplitude. $\acute{g} = g\frac{\Delta\rho}{\rho_{up}}$ is the reduced gravity determined by the density difference ($\Delta\rho$) between the upper (ρ_{up}) and lower (ρ_{low}) layers. D is the mean water depth. L_ρ and L_T denote horizontal length scales associated with density and tidal forcing, e.g., the salt intrusion length and the tidal excursion, respectively. $L_T = \frac{TU_T}{\pi}$ in which T is the tidal period (Valle-Levinson, 2022) and equals the M2 period (12-hour-and-25-minute) in this study as M2 is the unique tidal forcing in EXP4-EXP10 (see Table 1) and acts as the strongest tidal component in EXP11 with the mixed mainly semidiurnal tidal regime (see Table 2 and Figure 1C). Also L_ρ is considered as the distance from the estuary mouth in which the direction of $\frac{\partial s}{\partial x}$ changes from the inverse segment to the positive segment in the relevant salt-plug estuary according to Table 4. Figure 7B demonstrates that the logarithm of tidal Froude number higher than 3 (tidal forcing 3 orders of magnitude ≥ density gradients) occurs only for tidal amplitudes higher than 1 m (EXP8-EXP10) from ~ km 50 to ~ km 90 where salt plugs have salinity higher than 45 psu.

Thus, Figures 7A, B introduce the threshold of "***log(tidal Froude number)=3***" as the condition under which the tidal forcing can overcome the density gradient, and consequently

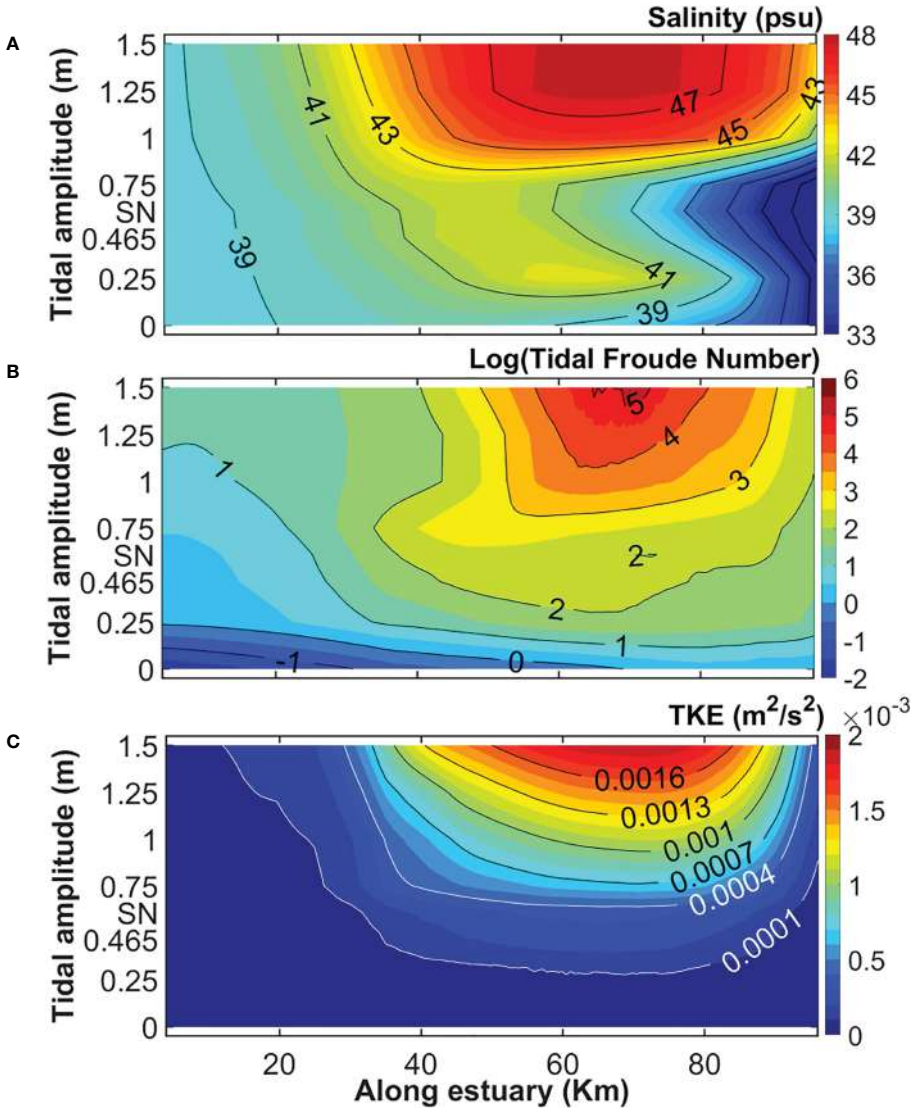

FIGURE 7
The tidally averaged depth-mean axial salinity **(A)**, the logarithm of tidal Froude number **(B)** and the turbulent kinetic energy TKE **(C)** from 8 scenarios of EXP4-EXP11 (see Table 1), as a function of distance from the estuary mouth (x-axis) and tidal amplitudes at the estuary mouth (y-axis). "SN" on the y-axis stands for the spring-neap scenario of EXP11.

salinity inside the salt plug zone and its location is dominated by tides. This is a new finding because salt plug estuaries have been exclusively attributed to density-driven flows.

The variations in quantity of salinity inside, and the location of the salt plug can be explained by different tidal forcing potentials of the microtidal and mesotidal estuaries, which impose different salt transports along the estuary. The analysis of different salt flux terms is discussed in Section 4.2.

The tidally averaged depth-mean axial turbulent kinetic energies (TKE) from EXP4 to EXP11 (Figure 7C) are consistent with the tidal Froude number distributions. Also, comparing this figure with Figure 7A indicates that the TKE, a measure of vertical mixing, increases from the inverse and positive estuarine segments toward the salt plug, especially at the meso-tidal estuaries.

In order to depict the influence of increasing tidal forcing on the longitudinal and lateral flows, these results from the meso-tidal

TABLE 4 The distances of the salt plug centers (where $\frac{\partial s}{\partial x}=0$) from the estuary mouth in the 8 numerical experiments of EXP4-EXP11 (These distances are considered as L_ρ to compute the tidal Froude number).

Experiment	EXP4	EXP5	EXP6	EXP7	EXP8	EXP9	EXP10	EXP11
Mouth-SMZ distance (km)	43.33	62.16	50.37	45.12	62.70	66.06	67.19	48.05

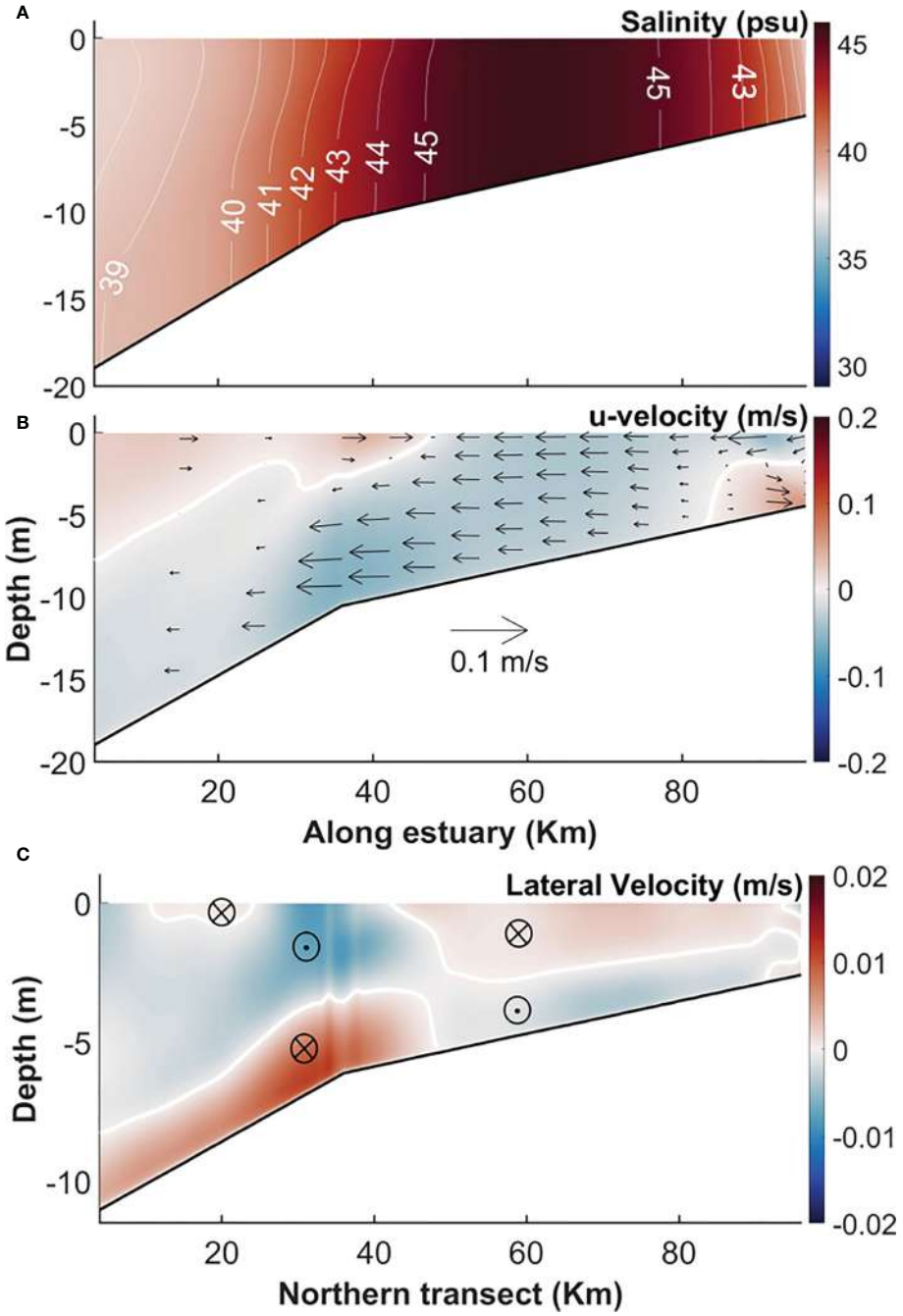

FIGURE 8
Along-channel profiles of time-averaged **(A)** salinity and **(B)** axial velocity along the main axis and **(C)** lateral velocities along the northern transect in EXP2.

EXP2 (with 1 m M2-tide at the mouth) in Figure 8 are compared with those in the micro-tidal EXP1 (with 0.465 m M2-tide at the mouth) in Figure 2.

When the tidal energy increases in EXP2 compared with that in EXP1, the freshwater rarely reaches the mid-estuary and is trapped near the estuarine head. It means that the positive estuarine segment weakens from the micro-tidal EXP1 to the meso-tidal EXP2 (compare Figures 2A with 8A, and 2C with 8B). The trend associated with more landward salt transport mainly by tidal advection (see Section 4.2), creates a stronger and more extensive salt plug in EXP2. In the other words, the salt plug in the meso-tidal EXP2 shows a much longer extension along the estuary, between 30 km and 90 km, and the salinity there is higher, from 42-45 psu (compare Figure 2A and Figure 8A). The zone of seaward longitudinal flows increases in size in EXP2 (compare Figure 2C and Figure 8B). The decrease in the area of landward flow is very strong at the bottom of the positive estuarine segment in Figure 8B in comparison to that in Figure 2C.

The landward expansion of the salinity-maximum zone and the contraction of the positive estuarine segment from EXP1 to EXP2 corresponds with a similar expansion and contraction in the lateral flows of EXP2 (compare Figures 5A and 8C). Figure 8C actually reveals a simple structure of lateral velocity in the mesotidal EXP2, particularly in the area of the positive estuarine segment. There, the situation is opposite to that in the salt plug: surface flows tend to diverge from the channel axis (thalweg) and converge at the bottom (Figure 8C). The increase in tidal amplitude in EXP2 also resulted in the formation of two surface circulation cells (on both sides of the thalweg) close to the mouth with an opposite sense of rotation to that of the dominant (converging toward the thalweg) cells.

4 Discussion

4.1 Longitudinal and lateral divergences

The ratio between tidally averaged lateral divergence (dv/dy) to longitudinal divergence (du/dx) is calculated at surface and bottom layers (Figures 9A, B) to determine their relative contribution to the divergence patterns associated with the salt plugs. In all eight scenarios (EXP4-EXP11), dv/dy is stronger than du/dx at the surface and bottom layers (Figures 9A, B). Thus, lateral divergence dominates the overall divergence, especially for the micro-tidal experiments.

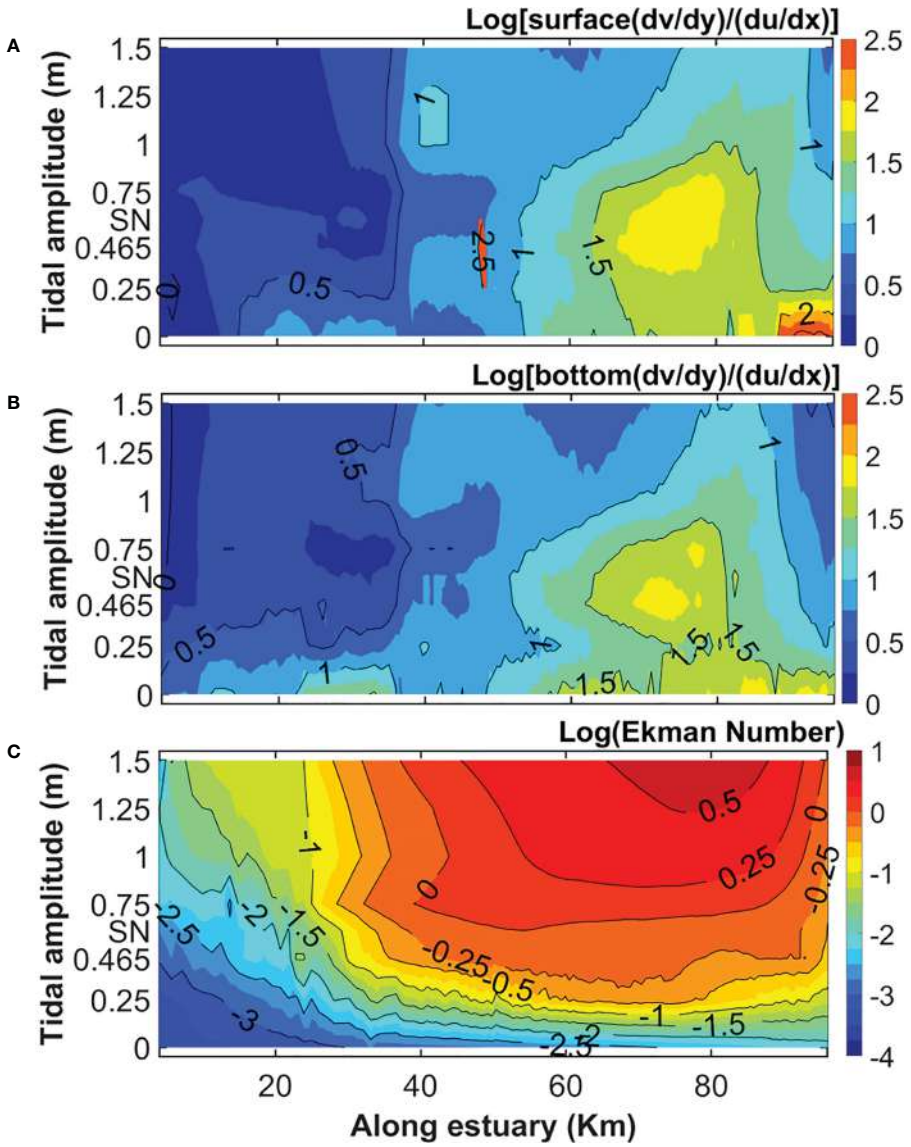

FIGURE 9
The logarithm of the ratio tidally averaged dv/dy to du/dx for surface **(A)** and bottom **(B)** layers as well as the logarithm of Ekman number **(C)** from 8 scenarios of EXP4-EXP11 (see Table 1), as a function of distance from the estuary mouth (x-axis) and tidal amplitudes at the estuary mouth (y-axis). "SN" on the y-axis stands for the spring-neap scenario of EXP11.

Also, the greatest ratios of dv/dy to du/dx are observed at the surface layer inside the salt plug of EXP11 (around 50 km, Figure 9A), resulting from a high value of dv/dy (see Figure 6C) and a low ratio of du/dx (see Figure 3A) at the same area. It suggests the importance of lateral divergent (longitudinal convergent) surface flows in the full spring-neap tidal cycle (28 days). Thus, lateral flows have a more important role than longitudinal flows in causing divergences. Section 3.2 (see Figure 4 and Table 3), it makes evident that Coriolis forcing affect the lateral circulations driven by the differential advection at the two cross-sections.

This is confirmed by estimates of Ekman number that is expressed as $E = \frac{A_z}{fD_{\max}^2}$ in Figure 9C where A_z and f are the vertical eddy viscosity and the Coriolis parameter respectively. D_{max} is the maximum water depth (the thalweg depth) of each cross-section. Coriolis forcing becomes higher than frictional effects (negative log of Ekman number) near the mouth for all the experiments and near the head of the micro-tidal experiments (Figure 9C). Positive log of Ekman numbers (stronger frictional effects than Coriolis forcing) nearly coincide with salt plugs attaining salinity > 45 psu and with logarithm of tidal Froude number > 3 (Figures 9C, 7A, B). Approaching the tidal Froude number (Figure 7B), TKE (Figure 7C) and Ekman number (Figure 9C) to their peak values inside the salt plug (Figure 7A) signifies that the nonlinearities reach their maximum values at the salt plug, particularly in the meso-tidal estuaries.

4.2 Link between salt-plug zones and salt-flux components

The phase difference between tidal velocity and salinity in the inverse (20 km) and positive (80 km) estuarine subsystems of EXP11 with a complex tidal regime tends to -90° and +90°, respectively (Figures 10A, C). It means that salinity reaches its maximum close to high water in the positive estuarine segment. Analogously, minimum salinities appear at low water in the positive segment (see the red and blue plots in Figure 10C). The opposite occurs for the inverse segment of the estuary (the red and blue plots in Figure 10A). The transition of the tidal flow-salinity phase difference from -90° to +90° should appear at the salt-plug zone, which explains the appearance of harmonics with ~6-hour periodicity at the plug (see Figure 10B). Inside the salt-plug zone (~ 48 km), salinity reaches maxima during peak ebb and peak flood, and its minima during high-water slacks and low-water slacks. The tidal axial flows and tidal level have also a phase difference of 90° throughout the shallow salt-plug estuary (see the black and blue plots in Figures 10A, B, C), signifying the formation of the standing wave in the estuary. In short and/or shallow estuarine embayments with negligible reflection, the phases of tidal velocity and water level are in quadrature, which specify classic standing waves (Friedrichs, 2010; Hosseini et al., 2016). Due to the landward convergence of the idealized geometry (effects of the convergent channel overcome friction effects), (see Figures 1A, B), both amplitudes of tidal flow and water-level increase in the landward direction (see the black and blue plots in Figure 10A–C). The amplitudes grow from ~0.3 m/s and ~0.93 m at 20 km (Figure 10A) toward the salt plug (~0.7 m/s and ~1.1 m in Figure 10B) and to the head (such as ~0.8 m/s and ~1.4 m at 80 km in Figure 10C). Also, the peak flood is stronger than the peak ebb at 80 km (the black plot in Figure 10C) indicating the tidal flood-dominated asymmetry at the upper estuary. The opposite asymmetry of ebb-dominance (stronger the peak ebb velocity than that during flood tide) is observed at the lower estuary of 20 km (see the black plot in Figure 10A) as Figure 2D shows these two contrary asymmetries.

The lower periodicity (higher frequency ~2 times) of the salinity fluctuation than the corresponding tidal current (Figure 10B) is associated with high tidal mixing inside the salt plug (see Figures 2D and 7C). In fact, the occurrence of extreme tidal fluctuations of salinity coincident with maximum tidal flood and ebb flows at the salinity maximum zone (Figure 10B) might be influenced by high tidal mixing there (Figure 7C), suggesting a considerable change of tidal pumping of salt in the salt plug.

The salt-flux decomposition along the estuary illustrates the advective salt flux (in the absence of wind forcing) as the dominant mechanism in both micro-tidal EXP5 (Figure 11A) and meso-tidal EXP10 (Figure 11C). In fact, the advective process (dominantly driven by tides) induces a landward salt flux that exponentially decreases along the estuary in the landward direction. This salt flux overcomes the other salt flux mechanisms, thus driving a landward total salt flux at the estuary and consequently reinforcing salinity maximum zone. The tidal advective salt flux is stronger in the mesotidal EXP10 than in the microtidal EXP5 particularly at the middle of estuary. For instance, the advection drives ~2200 m3/s psu in EXP10 that drops to ~250 m3/s psu in EXP5 at 40 km (see Figures 11A, C), which induces much stronger salt plug in EXP10 than in EXP5 (see Figure 7A). The advective salt flux is slightly weakened by the seaward sheared salt flux near the estuary mouth, especially in the microtidal estuary EXP5. The sheared salt flux remains seaward at the inverse estuarine segment (0 km – ~50 km) in both micro-tidal EXP5 and meso-tidal EXP10 (see Figure 11A, C). A sudden change observes at the advective flux and consequently at the total salt flux, especially in EXP10, around 36 km, where the bottom steepness change suddenly (see Figure 1B). Also, the tidal pumping of salt is close to zero in EXP5 but it experiences a low peak around the point of 36 km in EXP 10 (see Figures 11A, C). It can result from interactions between tidal flows and bathymetry changes.

In addition, higher tidal mixing during spring tide than in the neap tide particularly at the salt plug (around 50 km) of EXP3 (see Figures 6B, F) coincides with landward and seaward salt transport by tidal pumping at the salt plug in the spring and neap tides, respectively (see around 50 km in Figure 11B). Also, stronger landward advective salt flux occurs around 50 km in the spring tide than in the neap tide. Both changes in tidal pumping and advective salt transports in the spring-neap transition impose stronger salinity maximum zone during the spring tide (see Figures 3D, F).

In the neap tide, the tidal pumping of salt is relatively weak and shows a seaward transport at ~20 km – ~65 km, while it becomes stronger in the spring tide and indicates seaward directions close to the mouth and around 36 km (with the sudden change in the bottom steepness) during the spring tide (Figure 11B). The latter

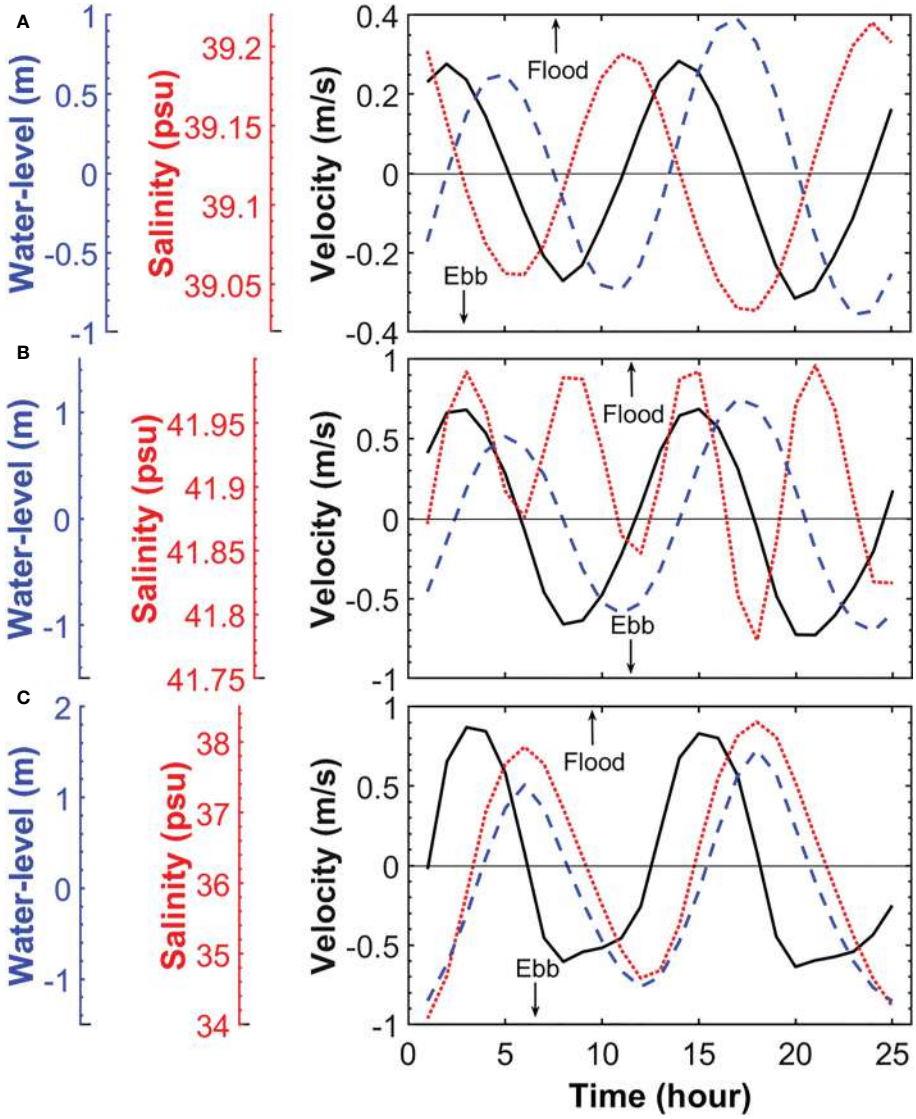

FIGURE 10
Tidal variations in depth-mean axial velocity (the thick black line), salinity (the dotted red line) and water-level (the dashed blue line) on the main channel axis at ~20 km **(A)**, ~ 48 km **(B)** and ~ 80 km **(C)** in EXP11 during 25 hours.

indicates a robust interaction between strong spring-tidal flows and bathymetry changes (see Figure 11B).

In both spring and neap tides, the time-averaged total salt flux is dominated by the advective flux (see Figures 11B, D). The seaward (negative) sheared salt flux is stronger in the neap tide than in the spring tide near the mouth because of higher longitudinal salinity (density) gradients driving stronger stratification during neap tide (Geyer and MacCready, 2014). This salt flux shows insignificant changes at the upper estuary (~40 km – 100 km), particularly inside the salt plug (around 50 km) in the spring-neap tidal cycle (see Figure 11D).

The advective, tidal pumping, sheared, and total salt fluxes depend on tidal forcing (experiments of EXP4-EXP11, Figure 12). The advective process mainly induces landward salt flux (with positive values) in the lower inverse estuary and at the salinity maximum zone. Seaward advective salt transport (with negative values) in the upper positive estuarine segment is driven by the low river discharge of 2 m^3/s (see Figure 12A). The seaward advective salt flux extends longer at the microtidal estuaries (EXP4-EXP7 and EXP11 with tidal amplitudes<1) than in the mesotidal experiments (EXP8-EXP10) upon decreasing tidal amplitude in the microtidal estuaries. The tidal pumping of salt almost shows seaward (negative) values at the salinity maximum zone of all the experiments (Figure 12B). In EXP4 and EXP5, the negative values of this salt flux also occur in the lower inverse estuary while a peak landward tidal salt flux around 36 km at the mesotidal estuaries indicates the importance of interactions between strong tidal flows and bathymetric changes (see Figure 12B). The sheared salt flux is usually landward in positive estuaries (Lerczak et al., 2006; Aristizábal and Chant, 2015; Valle-Levinson, 2022), which agrees with positive (landward) values of this salt flux in the upper positive estuarine segment of the microtidal salt-plug estuaries (Figure 12D).

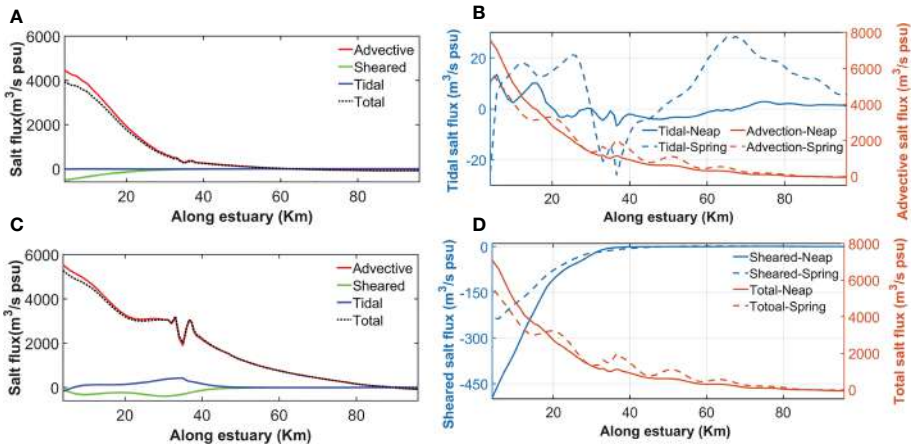

FIGURE 11
The distribution of the time averaged different salt flux terms along the estuary from the micro-tidal EXP5 **(A)** and from the meso-tidal EXP10 **(C)**, (see Table 1). Comparing the time averaged (75 hours) neap-spring salt fluxes from the tidal and advective terms **(B)** and from the sheared and total salt fluxes **(D)** in EXP3. The total salt flux equals advective plus sheared and tidal pumping. Positive fluxes are landward.

Conversely, the sheared salt flux becomes seaward at the lower inverse estuarine segment of all the salt-plug estuaries. The sheared flux shows an unusually weak seaward values close to the head of mesotidal salt-plug estuaries (see Figure 12D), which may result from overcoming tidal forcing over density gradients, as the sheared salt flux is driven by density gradients.

The salt transport by tidal advection (Figure 12A) dominates the fluxes by the tidal pumping (Figure 12B) and sheared (Figure 12D) terms throughout the estuary, which drives a similar total salt flux (Figure 12C). Therefore, in the lower estuary, landward total salt flux persists in all experiments (see Figure 12D). Thus, the salt plug formation and its location are controlled by high evaporation rates compared with low-river inflows associated with the total (net) salt transport consisting of three main salt fluxes induced by advection, tidal pumping and gravitational circulations (sheared term). The two latter terms (gravitational circulations and tidal pumping) cannot overcome the advective salt flux (in the absence of wind forcing). The secondary circulations can mainly redistribute isohalines laterally (see Figures 6B, D, F).

4.3 A framework for salt-plug estuaries based on Ekman and tidal Froude numbers

The logarithm of Ekman number (E) along the main axis approaches the highest value in the salt-plug zone (see Figures 7A and 9C) because of high values of vertical eddy viscosity A_z, where the longitudinal surface flows converge and the longitudinal bottom flows diverge (for example see Figures 2C and 8B). This maximum

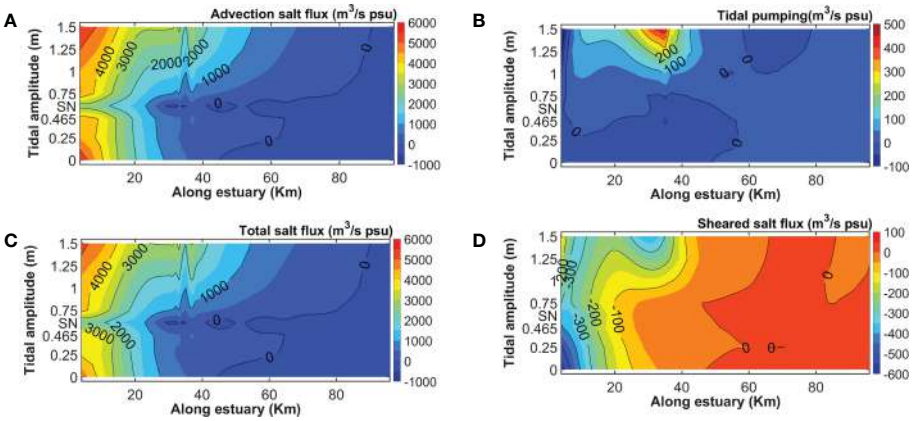

FIGURE 12
The time averaged advective **(A)**, tidal pumping **(B)**, total **(C)** and sheared **(D)** salt fluxes along the estuary from 8 scenarios of EXP4-EXP11 (see Table 1), as a function of distance from the estuary mouth (x-axis) and tidal amplitudes at the estuary mouth (y-axis). "SN" on the y-axis stands for the spring-neap scenario of EXP11 and positive fluxes are landward.

Ekman number rarely exceeds 1 ($(Log(E) = 0)$ in the micro-tidal EXP4-EXP7 and EXP11 (Figure 9C) but it becomes higher than 1.8 ($Log(E) > 0.25$) in the meso-tidal EXP8-EXP10 (see Figure 9C). The sheared bottom exchange flows in the region with high values of the Ekman number (within the salinity-maximum zone) resemble the laterally sheared flow mechanism suggested by Valle-Levinson (2008) in positive estuaries. Using laterally varying (channel-shoals) idealistic bathymetry, Valle-Levinson (2008) suggested that strong frictional control ($E > 1$) leads to horizontally sheared exchange flows in positive estuaries, independent of the width of the basin. Apparently, high frictional effects result in laterally sheared longitudinal flow patterns in both studies even though the salt-plug estuarine properties in this study are different from those in positive estuaries (the idealized positive estuary with high frictional effects and the narrow positive estuary of the Hudson River with moderate to strong friction) of Valle-Levinson (2008)'s study.

In addition to the high values of the Ekman number in the salt-plug zone, maximum values of tidal Froude number (Fr_T) also occur there (see Figures 7A, B). The logarithm of Fr_T rarely reaches 3 ($Fr_T = 1000$) in the microtidal salt-plug estuaries (EXP4-EXP7 and EXP11) while this logarithm passes 3 ($Fr_T > 1000$) in the meso-tidal EXP8-EXP10 (Figure 7B). Valle-Levinson (2021) suggested a general framework based on tidal Froude (Fr_T) and Ekman (E) numbers. This framework did not consider salt-plug estuaries so it is discussed here for different micro-tidal and meso-tidal funnel-shaped estuaries of EXP4-EXP11.

Based on this classification and considering the competition between Coriolis acceleration and friction, the entire estuarine basin of the salt-plug estuaries with tidal amplitudes lower than 0.25 m (at the mouth) belongs to the "deep (rotational)" space (see Figure 9C) in which $E \leq 0.1$ ($Log(E) \leq -1$). In the funnel-shaped salt-plug estuaries with tidal amplitudes higher than 0.25 m, the section between 0 km and ~25 km along the axis of the estuary is also classified as the "deep (rotational)" space (see Figures 9C and 13A). In these estuaries (with tidal amplitude > 0.25 m), the larger upstream part (~25 km -100 km) with $-1 < Log(E) < 1$ ($0.1 < E < 10$) is controlled by both rotation and friction (located in the "frictional and rotational" space). In particular, the salt plug in the meso-tidal EXP8-EXP10 shows high Ekman number greater than 1.8 ($Log(E) > 0.25$).

On the other hand, the micro-tidal salt-plug estuaries with tidal amplitudes lower than 0.25 have Fr_T values lower than 0.1 ($Log(Fr_T) \leq -1$), only close to the estuarine mouth that identifies "density-driven" classification. In the other words, almost none of the micro- and meso-tidal salt-plug estuaries (EXP4-EXP11) locate in the "density-driven" section.

According to the classification presented by (Valle-Levinson, 2021), the "tidally & density-driven" space with $-1 < Log(Fr_T) < 1$ ($0.1 < Fr_T < 10$) is only assigned to most of the inverse estuarine

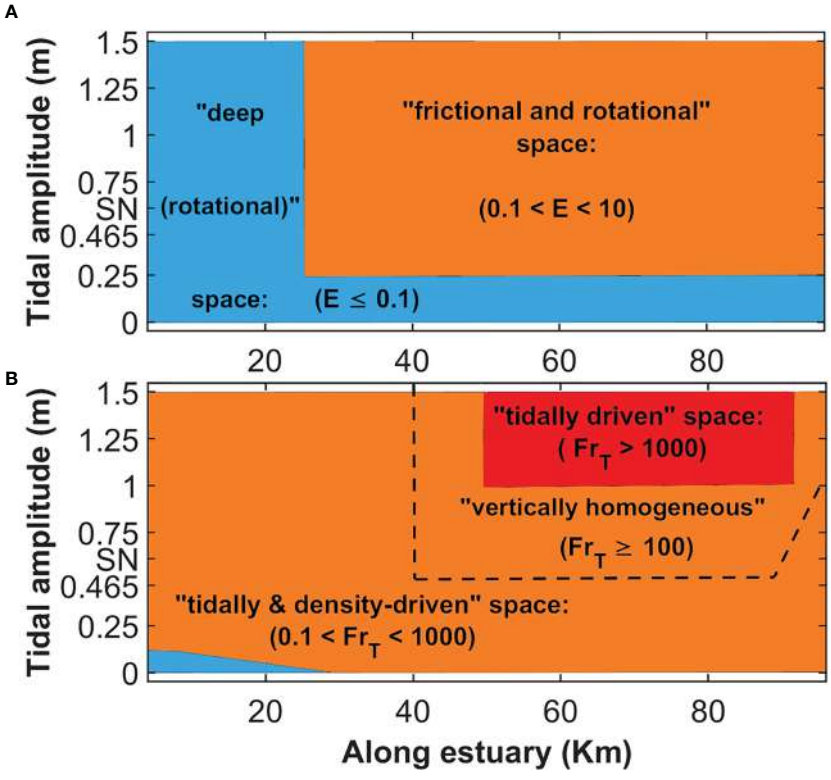

FIGURE 13
The schematic figures of the estuarine classification along the micro- and meso-tidal funnel-shaped salt-plug estuaries according to the longitudinal distributions of their Ekman **(A)** and tidal Froude numbers **(B)**. "SN" on the y-axis stands for the spring-neap scenario of EXP11. The small blue color close to the estuary mouth (0 km-30 km) in (b) indicates "density-driven" space with $Fr_T \leq 0.1$.

segments of the salt-plug estuaries with 0.25 m ≤ tidal amplitude ≤ 1 m and both inverse and positive segments of the estuaries with tidal amplitude< 0.25 m.

Also, based on this classification, the salinity maximum zone of the micro-tidal SPEs of EXP5, EXP6 and EXP11 (with tidal amplitude lower than 0.75 m) and the inverse estuarine segments of the meso-tidal EXP9 and EXP10 (with tidal amplitudes ≥ 1.25 m) belong to ("tidally driven" space) where $1 < Log(Fr_T) < 2$ ($10 < Fr_T < 100$). Although these areas and the salt plug of EXP 7 (with $Log(Fr_T) \sim 2.5$) are not completely "tidally driven" and they are also affected by density gradient (see Figures 7A, B).

On the other hand, the salinity maximum zones of the meso-tidal salt-plug estuaries of EXP8-EXP10 (with tidal amplitude ≥ 1m) have $Log(Fr_T) \geq 3$ ($Fr_T \geq 1000$) and correctly demonstrate a "tidally driven" section. Therefore, we suggest that the limitation of $0.1 < Fr_T < 10$ for the "tidally & density-driven" section can change to $0.1 < Fr_T < 1000$ and the "tidally driven" portion can be signified by $Fr_T \geq 1000$ in salt-plug estuaries (see Figure 13B). Thus, both inverse and positive estuarine segments of meso-tidal salt-plug estuaries and almost all parts (inverse and positive segments and salt plug area) of micro-tidal salt-plug estuaries are located in "tidally & density-driven" space with $-1 < Log(Fr_T) < 3$ ($0.1 < Fr_T < 1000$).

Since the salt-plug estuaries mainly belong to the "tidally & density-driven" space (the orange color in Figure 13B), tidal straining can substantially modulate stratification conditions in these estuarine systems. In the framework proposed, the salinity maximum zone appears to possess special characteristics (like having peak values of tidal Froude and Ekman numbers and TKE coincidently) in the salt-plug estuaries, especially in the meso-tidal experiments. In this zone of the meso-tidal EXP8-EXP10 with salinity > 45 psu (Figure 7A), TKE > 0.001 m^2/s^2 (Figure 7C), $Log(Fr_T) > 3$ (Figures 7B, 13B) and $Log(E) > 0.25$ (Figures 9C, 13A), tidal forcing dominates density gradient so tide is the basic strong driver of the tidally averaged or residual flows.

In the zone with $Fr_T \geq 100$ ($Log(Fr_T) \geq 2$), the tidally averaged flow is weakly influenced by baroclinicity and can be labeled as "vertically homogeneous" in the framework for salt-plug estuaries (see Figures 7B, 13B). Although, (Valle-Levinson, 2021), presented the condition of $Fr_T > 10$ for the "vertically homogeneous" in the classification. The inverse estuarine segment of EXP2 (with 1m amplitude) is not vertically homogeneous (see Figures 8A, B) although the similar segment of EXP8 (with 1m amplitude) has $Fr_T > 10$ (see Figure 7B). In fact, the criteria of $Fr_T \geq 100$ is consistent with the weakly stratified conditions within the salinity maximum zones in salt-plug estuaries with tidal amplitudes ≥ 0.5 m (see the mixed condition of EXP1 in Figure 2D), particularly in the meso-tidal EXP8-EXP10 (see Figure 7C), where $\acute{g}$ is almost minimal (Fr_T values are close to the maximum values), (see Figure 7B).

Valle-Levinson (2021) reported that the two transitions $E = 1$ and $Fr_T = 10$ may change from neap to spring tides and occur at different geographical locations at a specified time because of bathymetric variations, resulting in different E and Fr_T. In our study, the location of the salt plug in EXP11 (see Figure 7A) is close to both transition zones of $Log(E) \sim 0$ (see Figure 9C) and $Fr_T \sim 100$ ($Log(Fr_T) \sim 2$) (see Figure 7B), which insignificantly changes from the neap to spring tides (see Figures 3C-F).

Conclusion

In this study, the hydrodynamics in micro- and meso-tidal salt-plug estuaries are investigated using the numerical model SCHISM. Several modeling experiments are performed using an idealized funnel-shaped basin, which is assumed to be located close to the Mond River Estuary in the Persian Gulf. This study addresses for the first time the competition between density gradients and tidal forcing in the formation of salt plugs, as well as their lateral circulation. The results show that the salt-plug estuary is characterized by a salinity maximum zone in the mid-estuary separating the inverse and positive estuarine subsystems. The salt plug shows weakly stratified conditions (high turbulent kinetic energy) and has high values of tidal Froude and Ekman numbers especially in the meso-tidal salt-plug estuaries. Increasing the tidal Froude number from the micro-tidal salt-plug estuaries (with tidal amplitudes less than 1 m at the estuary mouth) to the meso-tidal experiments (with tidal amplitudes higher than 1 m) results in a stronger salt plug with the tidal Froude number higher than 1000, extending from the mid-estuary to the head. It signifies dominating tidal forcing over baroclinicity in the strong salt plug and resulted from enhancing landward salt flux by tidal advection in the meso-tidal estuaries. The longitudinal and lateral circulations consequently change due to the resulting changes in the longitudinal salinity gradients. In the absence of Coriolis and wind forces, differential advection appears to be the dominant driver of lateral flows so that the time-averaged lateral circulations demonstrate very similar patterns (converging surface flows over the deep channel) within the positive and inverse subsystems. These lateral flows reverse in the area of the salt plug (diverging surface flows over the deep channel). Coriolis accelerations influence the lateral circulation driven by differential advection and lateral divergence dv/dy even at the narrow sections close to the head. In the salt-plug estuaries, tidal fluctuations in salinity show that maximum salinities occur at times of high water slacks in the upper positive estuarine segment and at low water slacks in the lower inverse segment, which impose the salinity cycle with approximately half the tidal period at the salt plug. This half-tidal period (the occurrence of maximum salinities during extreme tidal velocities) indicates the importance of salt transport by the tidal pumping process at the salt plug where the direction of tidal pumping of salt changes. The spring–neap variability in the salt-plug estuary shows that both longitudinal positive and inverse subtidal circulation cells join each other during neap tide and have a maximum distance in the mid-estuary (approximately 50 km) during spring tide. Also, the salt plug in the spring tide is slightly saltier than in the neap tide because of stronger tidal mixing and consequently a landward salt flux by tidal pumping during the spring tide contrary to the neap tide (with a seaward tidal salt flux) as well as a higher tidal advective salt flux in the spring tide. In addition, inside the salt plug, tidally averaged lateral circulations

show downwelling cells in the spring tide and upwelling during the neap tide over the thalweg, indicating strong neap–spring variability. The salt plug location is controlled by the main longitudinal salt transports of tidal advection. Actually, this location is not considerably influenced by lateral flows. Although, the secondary flows can laterally redistribute isohalines in the vertical shape. For instance, the upwelling flows over the thalweg lift isohalines in the neap tide, while lying down lateral flows depress isohalines in the thalweg during the spring tide.

Data availability statement

The original contributions presented in the study are included in the article. Further inquiries can be directed to the corresponding authors.

Author contributions

STH, ES, JP and AVL contributed to the conception and design of the study. STH and JP developed the model set-up and different numerical experiments. STH performed model analyses and wrote the first draft of the manuscript. ES, AVL, and CS advised on the analysis of model results. All authors contributed to the article and approved the submitted version.

Funding

This study is a contribution to theme "C3: Sustainable Adaption Scenarios for Coastal Systems" of the Cluster of Excellence EXC 2037 'CLICCS - Climate, Climatic Change, and Society' – Project Number: 390683824 funded by the Deutsche Forschungsgemeinschaft (DFG, German Research Foundation) under Germany's Excellence Strategy.

Acknowledgments

This study used data from the DHI, CMEMS and ECMWF. Additionally, we thank Benjamin Jacob (Helmholtz-Zentrum Hereon) for his help with modeling.

Conflict of interest

The authors declare that the research was conducted in the absence of any commercial or financial relationships that could be construed as a potential conflict of interest.

Publisher's note

All claims expressed in this article are solely those of the authors and do not necessarily represent those of their affiliated organizations, or those of the publisher, the editors and the reviewers. Any product that may be evaluated in this article, or claim that may be made by its manufacturer, is not guaranteed or endorsed by the publisher.

References

Aristizábal, MaríaF., and Chant, R. J. (2015). An observational study of salt fluxes in Delaware bay. *J. Geophys. Res.: Oceans* 120 (4), 2751–2768. doi: 10.1002/2014JC010680

Cabrera, O. C., Villanoy, C. L., Jacinto, G. S., Bernardo, L. P. C., Ferrera, C. M., Velasquez, I. B., et al. (2014). Salt-plug estuarine circulation in malampaya sound, palawan, Philippines. *Phil. Sci. Lett.* 7, 428–437.

Chant, R. J. (2010). "Estuarine secondary circulation," in *Contemporary issues in estuarine physics* (Cambridge University Press), 100–124. doi: 10.1017/CBO9780511676567.006

Chen, S.-N., and Sanford, L. P. (2009). Lateral circulation driven by boundary mixing and the associated transport of sediments in idealized partially mixed estuaries. *Continental Shelf Res.* 29 (1), 101–118. doi: 10.1016/j.csr.2008.01.001

Cheng, Y., and Andersen, O. B. (2010). Improvement in global ocean tide model in shallow water regions. *Poster SV* 45, 1–68.

Ensing, E., de Swart, H. E., and Schuttelaars, H. M. (2015). Sensitivity of tidal motion in well-mixed estuaries to cross-sectional shape, deepening, and sea level rise. *Ocean Dynam.* 65 (7), 933–950. doi: 10.1007/s10236-015-0844-8

Friedrichs, C. T. (2010). Barotropic tides in channelized estuaries. *Contemp. Issues Estuar. Phys.* 27, 61. doi: 10.1017/CBO9780511676567.004

Friedrichs, C. T., and Valle-Levinson, A. (1998). Transverse circulation associated with lateral shear in tidal estuaries. *Proceedings, Physics of Estuaries and Coastal Seas, 9th International Biennial Conference*, Sponsored by Kyushu and Ehime Universities, Matsuyama, Japan, 24-26 September, p. 15–17.

Garvine, R. W. (1995). A dynamical system for classifying buoyant coastal discharges. *Continental Shelf Res.* 15 (13), 1585–1596. doi: 10.1016/0278-4343(94)00065-U

Geyer, W.R. (1993). Three-dimensional tidal flow around headlands. *J. Geophys. Res.: Oceans* 98 (C1), 955–966. doi: 10.1029/92JC02270

Geyer, W.R., and MacCready, P. (2014). The estuarine circulation. *Annu. Rev. fluid mechanics* 46, 175–197. doi: 10.1146/annurev-fluid-010313-141302

Ghaemi, M., and Gholamipour, S. (2017). Seasonal measurement of nutrient concentrations and total alkalinity in the mond estuary ecosystem. *J. Oceanogr.* 8 (30), 11–18. doi: 10.29252/joc.8.30.11

Hosseini, S. T., Chegini, V., Sadrinasab, M., Siadatmousavi, S. M., and Yari, S. (2016). Tidal asymmetry in a tidal creek with mixed mainly semidiurnal tide, bushehr port, Persian gulf. *Ocean Sci. J.* 51 (2), 195–208. doi: 10.1007/s12601-016-0017-9

Hosseini, S. T., and Siadatmousavi, S. M. (2018). Field observations of hypersaline runoff through a shallow estuary. *Estuarine Coast. Shelf Sci.* 202, 54–68. doi: 10.1016/j.ecss.2017.12.003

Huijts, K. M. H., de Swart, H. E., Schramkowski, G. P., and Schuttelaars, H. M. (2011). Transverse structure of tidal and residual flow and sediment concentration in estuaries. *Ocean Dynam.* 61 (8), 1067–1091. doi: 10.1007/s10236-011-0414-7

Johnson, G. C., and Ohlsen, D. R. (1994). Frictionally modified rotating hydraulic channel exchange and ocean outflows. *J. Phys. Oceanogr.* 24 (1), 66–78. doi: 10.1175/1520-0485(1994)024<0066:FMRHCE>2.0.CO;2

Juarez, B., Valle-Levinson, A., and Li, C. (2020). Estuarine salt-plug induced by freshwater pulses from the inner shelf. *Estuarine Coast. Shelf Sci.* 232, 106491. doi: 10.1016/j.ecss.2019.106491

Khosravi, M., Siadatmousavi, S. M., Vennell, R., and Chegini, V. (2018). The transverse dynamics of flow in a tidal channel within a greater strait. *Ocean Dynam.* 68 (2), 239–254. doi: 10.1007/s10236-017-1127-3

Kranenburg, W. M., Geyer, W.R., Garcia, A. M. P., and Ralston, D. K. (2019). Reversed lateral circulation in a sharp estuarine bend with weak stratification. *J. Phys. Oceanogr.* 49 (6), 1619–1637. doi: 10.1175/JPO-D-18-0175.1

Largier, J. (2010). "Low-inflow estuaries: hypersaline, inverse, and thermal scenarios" *in Contemporary issues in estuarine physics*. (Cambridge: Cambridge University Press), 247–272. doi: 10. 1017/CBO9780511676567

Lerczak, J. A., and Geyer, W.R. (2004). Modeling the lateral circulation in straight, stratified estuaries. *J. Phys. Oceanogr.* 34 (6), 1410–1428. doi: 10.1175/1520-0485(2004)034<1410:MTLCIS>2.0.CO;2

Lerczak, J. A., Geyer, W.R., and Chant, R. J. (2006). Mechanisms driving the time-dependent salt flux in a partially stratified estuary. *J. J. Phys. Oceanogr.* 36 (12), 2296–2311. doi: 10.1175/JPO2959.1

Li, M., Cheng, P., Chant, R., Valle-Levinson, A., and Arnott, K. (2014). Analysis of vortex dynamics of lateral circulation in a straight tidal estuary. *J. Phys. Oceanogr.* 44 (10), 2779–2795. doi: 10.1175/JPO-D-13-0212.1

Li, C., and O'Donnell, J. (1997). Tidally driven residual circulation in shallow estuaries with lateral depth variation. *J. Geophys. Res.: Oceans* 102 (C13), 27915–27929. doi: 10.1029/97JC02330

Li, C., and Valle-Levinson, A. (1999). A two-dimensional analytic tidal model for a narrow estuary of arbitrary lateral depth variation: the intratidal motion. *J. Geophys. Res.: Oceans* 104 (C10), 23525–23543.

Mariani, R., Lessa, G. C., and Marta-Almeida, M. (2022). Long-term variability of the salinity field in a Large tropical, well-mixed estuary: the influence of climatic trends. *Estuaries Coasts* 45 (3), 721–736. doi: 10.1007/s12237-021-01008-y

Nunes, R. A., and Simpson, J. H. (1985). Axial convergence in a well-mixed estuary. *Estuarine Coast. Shelf Sci.* 20 (5), 637–649. doi: 10.1016/0272-7714(85)90112-X

Ott, M. W., and Garrett, C. (1998). Frictional estuarine flow in Juan de fuca strait, with implications for secondary circulation. *J. Geophys. Res.: Oceans* 103 (C8), 15657–15666. doi: 10.1029/98JC00019

Pein, J., Valle-Levinson, A., and Stanev, E. V. (2018). Secondary circulation asymmetry in a meandering, partially stratified estuary. *J. Geophys. Res.: Oceans* 123 (3), 1670–1683. doi: 10.1002/2016JC012623

Phillips, O. M. (1970). On flows induced by diffusion in a stably stratified fluid. *Deep Sea Res. Oceanogr Abstracts*. 17, 435–443. doi: 10.1016/0011-7471(70)90058-6

Rozovskii, I. L. (1957). "Flow of water in bendsof open channels." *The Academy of Science of the Ukraine SSR*. SUKEQAWA, N. 1971 Conditions for the occurrence of river meanders. Trans. JSCE 2, 257–261.

Scully, M. E., Geyer, W.R., and Lerczak, J. A. (2009). The influence of lateral advection on the residual estuarine circulation: a numerical modeling study of the Hudson river estuary. *J. Phys. Oceanogr.* 39 (1), 107–124. doi: 10.1175/2008JPO3952.1

Shaha, D. C., and Cho, Y.-K. (2016). Salt plug formation caused by decreased river discharge in a multi-channel estuary. *Sci. Rep.* 6 (1), 1–11. doi: 10.1038/srep27176

Stanev, E. V., Jacob, B., and Pein, J. (2019). German Bight estuaries: an inter-comparison on the basis of numerical modeling. *Continental Shelf Res.* 174, 48–65. doi: 10.1016/j.csr.2019.01.001

Umlauf, L., and Burchard, H. (2003). A generic length-scale equation for geophysical turbulence models. *J. Mar. Res.* 61 (2), 235–265. doi: 10.1357/002224003322005087

Valle-Levinson, A. (2008). Density-driven exchange flow in terms of the kelvin and ekman numbers. *J. Geophys. Res.: Oceans* 113, C04001. doi: 10.1029/2007JC004144

Valle-Levinson, A. (2010). Definition and classification of estuaries. In A. Valle-Levinson (Ed.), *Contemporary Issues in estuarine physics* (pp. 1–11). Cambridge, UK: Cambridge University Press. doi: 10.1017/CBO9780511676567.002

Valle-Levinson, A. (2011). 1.05 classification of estuarine circulation. *Treatise Estuar. Coast. Sci.* 1, 75–86. doi: 10.1016/B978-0-12-374711-2.00106-6

Valle-Levinson, A. (2021). Dynamics-based classification of semienclosed basins. *Regional Stud. Mar. Sci.* 46, 101866. doi: 10.1016/j.rsma.2021.101866

Valle-Levinson, A. (2022). *Introduction to estuarine hydrodynamics* (Cambridge University Press). doi: 10.1017/9781108974240

Valle-Levinson, A., and Bosley, K. T. (2003). Reversing circulation patterns in a tropical estuary. *J. Geophys. Res.: Oceans* 108 (C10), 3331. doi: 10.1029/2003JC001786

Valle-Levinson, A., Reyes, C., and Sanay, R. (2003). Effects of bathymetry, friction, and rotation on estuary–ocean exchange. *J. Phys. Oceanogr.* 33 (11), 2375–2393. doi: 10.1175/1520-0485(2003)033<2375:EOBFAR>2.0.CO;2

Wolanski, E. (1986). An evaporation-driven salinity maximum zone in Australian tropical estuaries. *Estuarine Coast. Shelf Sci.* 22 (4), 415–424. doi: 10.1016/0272-7714(86)90065-X

Wunsch, C. (1970). On oceanic boundary mixing. *Deep Sea Res Oceanogr. Abstracts* 17, 293–301. doi: 10.1016/0011-7471(70)90022-7

Zhang, Y. J., Ye, F., Stanev, E. V., and Grashorn, S. (2016). Seamless cross-scale modeling with SCHISM. *Ocean Model.* 102, 64–81. doi: 10.1016/j.ocemod.2016.05.002

3 Study II: Freshwater Lens Estuarine Hydrodynamics

This chapter contains the second paper, which has been published in Regional Studies of Marine Science:

Hosseini, S.T., Siadatmousavi, S.M., Stanev, E., Pein, J. and Schrum, C. (2024). **Transitions between different estuarine states in a low-inflow estuary of arid coasts (Mond Estuary, Persian Gulf) with a focus on freshwater lenses.** Regional Studies in Marine Science 74 (2024) 103525. doi: https://doi.org/10.1016/j.rsma.2024.103525

Author contributions:

STH initiated the study, set up the numerical model, generated the data sets, performed the data analysis and wrote the manuscript. SMS and JP contributed to the data analysis and discussion of the results. ES and CS contributed to the discussion and the design of the study. All authors participated in the conception of this study, and revised and approved the manuscript.

Regional Studies in Marine Science 74 (2024) 103525

Contents lists available at ScienceDirect

Regional Studies in Marine Science

journal homepage: www.elsevier.com/locate/rsma

Transitions between different estuarine states in a low-inflow estuary of arid coasts (Mond Estuary, Persian Gulf) with a focus on freshwater lenses

Seyed Taleb Hosseini [a,*], Seyed Mostafa Siadatmousavi [b], Emil Stanev [a,c], Johannes Pein [a], Corinna Schrum [a,d]

[a] Institute of Coastal Systems - Analysis and Modeling, Helmholtz-Zentrum Hereon, Geesthacht, Germany
[b] Iran University of Science &Technology, Tehran, Iran
[c] Department of Meteorology and Geophysics, Faculty of Physics, Sofia University "St. Kliment Ohridski", Sofia, Bulgaria
[d] Institute of Oceanography, Center for Earth System Research and Sustainability, Universität Hamburg, Hamburg, Germany

ARTICLE INFO

Keywords:
Tidal damping
Salt flux
Péclet number
Mond Estuary
Persian Gulf

ABSTRACT

This study shows that the Mond Estuary, Persian Gulf experiences notable time-dependent longitudinal salinity variations. Monthly-seasonal variability in salinity changes from a positive estuarine system in wintertime to inverse and salt-plug estuaries during summertime. A highly unsteady state (time scale of hours-days) occurs in the wintertime named the freshwater lens estuary (FLE), in which a low-salinity water mass (lens) is confined by both marine and riverine saltwater sources. Here, FLE dynamics is investigated using realistic and idealized numerical models and two 25-hour data sets collected immediately before a hypersaline runoff (weak FLE condition) and during another one (strong FLE condition). The Péclet Number (*Pe*) reveals a much stronger advective transports than diffusive one ($Pe > 5.7$) throughout the estuary. An exception from this behavior (stronger mixing with $Pe = 0.8$) is observed at the estuary downstream, where a significant amount of freshwater mixes with seawater during the weak FLE conditions. Also, the minimum hypersaline runoff of ~400 m^3/s estimated by the numerical model can dampen tidal waves at the head of the estuary. In an idealized basin, the model shows that FLE longitudinal flows form two cells of positive estuarine circulation separated by a maximum mixing zone (the potential energy anomaly <0.75 J/m^3). In the Mond Estuary, a sea-level rise of 20 cm increases salinity in the FLE state and the positive estuary during winter. Conversely, it decreases salinity in the inverse and salt-plug estuaries in summer.

1. Introduction

The Mond River Estuary is a short (18–20 km long), narrow and very shallow (average depth of ~1.7 m), meandering estuary (Hosseini and Siadatmousavi, 2018) located on the northern coast of the Persian Gulf (Fig. 1). During the wet months, salinity at the head of the estuary increases following heavy precipitation in the upstream estuary. In fact, there are two main sources of salt upstream of the Mond Estuary. These include salinity sources in the salt dome of Kuh-e-Namkak (Talbot and Jarvis, 1984; Talbot and Rogers, 1980; Talbot, 1981) and the seasonal Shour River ("shour" means "salty" in Persian, see their locations in Fig. 1a). The Shour River generally dries in the warm months due to high evaporation rates. It has no freshwater inflows in the wet months as the inflowing water passes over the saline soils, especially after high rainfall. This transition in the river forcing results in an alteration of the type of estuarine circulation from positive to freshwater lens estuary (FLE, Hosseini and Siadatmousavi (2018)). In the FLE regime, a low-salinity lens is sandwiched in the mid-estuary between two salt-water masses: one from the Persian Gulf near the mouth and another from hypersaline runoff at the head. When a high-salinity water flood emerges at the head of a positive estuary, the FLE state begins to develop within the estuary. This unsteady state ends when the low-salinity lens dissipates near the estuary mouth. In this study, along-channel dynamics of an FLE system is addressed in detail.

The estuarine system of the Mond Estuary in the summertime is characterized by a salinity maximum zone (SMZ) or a salt plug in the mid-estuary (Ghaemi and Gholamipour, 2017). The SMZ separates a positive estuarine circulation at the upper estuary (in the SMZ upstream) from an inverse estuarine segment at the lower estuary (between the estuary mouth and SMZ). This estuarine condition usually occurs under

* Corresponding author.
E-mail address: seyed.hosseini@hereon.de (S.T. Hosseini).

https://doi.org/10.1016/j.rsma.2024.103525
Received 7 September 2023; Received in revised form 4 March 2024; Accepted 14 April 2024
Available online 15 April 2024
2352-4855/© 2024 The Author(s). Published by Elsevier B.V. This is an open access article under the CC BY license (http://creativecommons.org/licenses/by/4.0/).

a very low river inflow and high evaporation rates (Valle-Levinson, 2010; Valle-Levinson, 2011).

A "non-trivial" type of salinity gradient along the estuary is found in the FLE estuarine systems that opposes the gradient of salt-plug estuaries. An FLE state experiences a minimum salinity (low-salinity lens) within the estuary instead of the salt plug (SMZ) in a salt-plug estuary. To the best of our knowledge, little is known so far about dynamics of estuarine systems switching between salt-plug and FLE estuarine types. In fact, the Mond Estuary points out a salinity field that is never in a steady state. Its along-channel salinity shows temporal variability from hours to days in the FLE condition to months to seasons in the salt-plug estuary conditions.

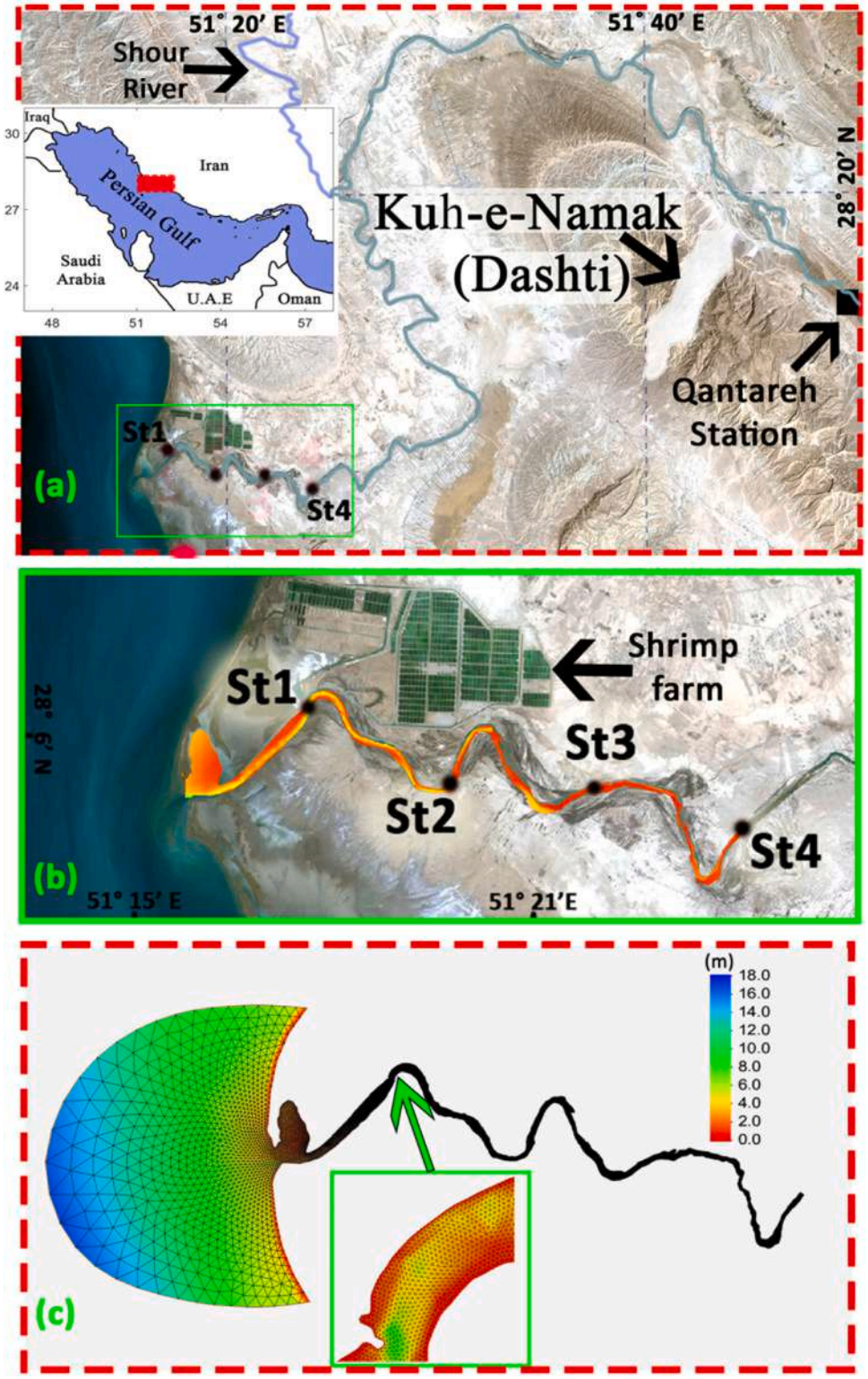

Fig. 1. (**a**) The geographic location of the Mond River Estuary which is bordered by the Persian Gulf in the west and the salt dome of Kuh-e-Namak (Dashti) and the seasonal Shour River in the east. The location of Qantareh station, which records the Mond River discharge, are also shown. (**b**) 4 CTD-Current meter stations and the location of shrimp farm are denoted in the estuary. (**c**) The computational grid used in the model of SCHISM. The inset shows the mesh grid close to St1.

Like hypersaline floods in the Mond Estuary, freshwater runoffs imposed by episodic rainstorm events in subtropical estuaries such as the Eprapah Creek, eastern Australia (Chanson, 2008) drive a highly unsteady state in the estuarine salinity field. Biemond et al. (2022) studied the impact of sudden high river discharge with short periods (freshwater pulses) on seawater intrusion in the Guadalquivir Estuary (Spain). They indicated that the decrease in the seawater intrusion is controlled by intensities and durations of the freshwater pulses, and tidal forcing has a minor influence on the salt intrusion. Another example of the highly unsteady estuarine state was suggested by Banas et al. (2004) in the Willapa Bay, Washington, where both river and ocean ends are highly variable in time. In this bay, the ocean condition alternating between wind-driven downwelling and upwelling along with variations in the intrusion of the buoyant Columbia River plume impose significant variations in salinity gradients on the event scale, ranging from 2 to 10 days (Banas et al., 2004).

The Mond Estuary with monthly to seasonal variations in the along-channel salinity (salt-plug estuary) is similar to the monsoonal estuaries e.g. the Mandovi estuary, west coast of India that is influenced by the Indian summer monsoon (Vijith et al., 2009). The Mandovi estuary experiences notable time-dependent salinity during a year transforming from riverine (induced by $\sim$1000 m^3/s intense runoff in the wet season) to highly stratified (salt-wedge) to partially mixed to well-mixed (late dry season with $\sim$1 m^3/s river inflow), (Vijith et al., 2016). Similarly, the microtidal Cochin Estuary, west coast of India shows the salt wedge system in the wet season and a partially to well-mixed estuaries during the dry season (Janardanan et al., 2015). The Yura Estuary (Japan) is a salt-wedge microtidal estuary that responds to both seasonal and short-term variations in river inflows (flood events). The salt-wedge moves landward (the intrusion length of salt-wedge increases) during summer and autumn with reducing river discharge, while the salt-wedge retreats seaward in winter and spring. A river flood > 250 m^3/s has the potential to eliminate the salt-wedge from the estuary (Funahashi et al., 2013).

This study aims to improve knowledge and fill gaps (mentioned in following) in understanding the time-dependent estuarine states particularly FLE hydrodynamics in the Mond River Estuary.

Generally, the gravitational circulation is one of the major drivers that brings salt into positive estuaries (Aristizábal and Chant, 2015; Valle-Levinson, 2022). On the other hand, hypersaline runoffs producing a strong seaward salt transport can overcome the estuarine circulation even at the estuary mouth. It highlights the strong interplay between the positive estuarine circulation and dispersion imposed by hypersaline runoffs. Therefore, one notable characteristic of the Mond FLE condition is the amount of salt, which is transported to the Persian Gulf by a strong hypersaline runoff. One of the objectives of the present study is to estimate this amount using observation data. For that, we calculate all terms contributed to the net salt flux along the estuary. Then, the non-dimensional Péclet Number (see Section 2.3.3) is analyzed to assess the relative influence of advection and diffusion.

Our next objective is to estimate the minimum amount of hypersaline runoff that can dampen tidal signals at the head of the estuary. Since data from observations are rather sparcy to fully address this issue (see Section 2.3.2), we use results from a numerical model to fill an important gap in our knowledge.

Our third objective is, using numerical modeling, to address seasonal estuarine variability in the Mond Estuary, specifically the formation of an FLE system and its similarities and differences to the estuarine circulations in salt-plug estuaries. In particular, the longitudinal circulation cells of a salt-plug estuary in an idealized basin (Hosseini et al., 2023) are compared with those in the corresponding idealized FLE system from this study. We use the idealized basin because the shallowness and meandering properties of the Mond Estuary may prevent to extend stratified flows along the estuary.

According to the Intergovernmental Panel on Climate Change (IPCC), one of the major concerns in coastal and estuarine areas is sea level rise, which is accelerating primarily due to global warming (Masson-Delmotte et al., 2021). In particular, a sea-level rise of 4 mm/yr was estimated by Etemadi et al. (2021), through analyzing 14-year (1995–2009) data from a tide gauge station near the Mond Estuary. (Baubekova et al., 2023), using the remote sensing analysis, showed that the sea level rise enhanced water coverage in the coastal area along with a landward shift of vegetation in the Mond protected area. The same authors suggested that rising sea level has a higher impact on this protected area than the upstream human activities (i.e. river regulation and land-use change). Therefore, the pressure induced by climate change is identified as the main stressor in the Mond River area. The global mean sea-level rise was estimated as 3.4 ± 0.6 mm/yr from 2001 to 2019 (Bagnell and DeVries, 2023). Normand et al. (2023) estimated a sea level rise of 21.3–22.7 cm in Bahrain Island (south of the Persian Gulf) by the year 2100. With assumption of 20 cm rising sea-level by 2100, the numerical model is also utilized to further investigate how this sea-level rise may affect along-channel salinity distribution in the Mond Estuary (the fourth objective). Sea-level rise reinforces saltwater intrusion into estuaries (Bhuiyan et al., 2012), as this process increases the entering volume of seawater into the estuarine basins. The process can oppose the pressure gradient driven by seaward freshwater river discharges (Valle-Levinson and Li, 2023).

This paper is structured as follows. Section 2 gives details on the characteristics of the studied area. Also, the observed data during FLE conditions along with relevant equations for calculating different salt flux terms, as well as the model setups of the real (Mond Estuary) and idealized basins are presented in this section. Section 3 depicts both observational and modeling results at the Mond Estuary. The observational analysis includes tidal variations in salinity and velocity, different salt fluxes, and the advection-diffusion competition using Péclet number. The modeling results address an evaluation of the numerical model against observations, FLE longitudinal salinity and velocity variations, an estimation of hypersaline runoff damping tidal waves, and time-dependent estuarine states in the Mond Estuary. Discussions on the idealized FLE longitudinal circulation and the impacts of a sea-level rise on the different time-dependent estuarine systems of the Mond Estuary are presented in Section 4, followed by a conclusion.

2. Methods and data

2.1. Study area

The Mond Estuary manifests a funnel-shaped geometry, widening 150 m and deepening to 10 m at a distance of 3 km from the mouth. Its width remains approximately constant for the rest of the estuary (see Fig. 1). The maximum depth of $\sim$10 m (close to St1 in Fig. 1b) is maintained by periodic dredging to facilitate pumping of water into Iran's largest shrimp farm (Ghaemi and Gholamipour, 2017) in the north of the estuary (see Fig. 1b). On one side, the farm creates a special economic interest in the Mond Estuary, but on the other side, its operation (e.g. pumping $\sim$8 m^3/s from the estuarine water and periodically dredging at the mouth) creates anthropogenic pressure that may influence the estuarine hydrodynamics and ecosystems of migratory birds, wildlife and aquatic organisms, especially fish. In the south of the estuary, the Mond protected area is located covering $\sim$46500 ha (Etemadi et al., 2021).

This estuary cannot provide navigation facilities because of its very shallow depths. Naturally, depths of $\sim$2 m dominate the bathymetry in the Mond Estuary, except within the estuary bends where the depth increases to more than 3 m. The estuary is a microtidal embayment with a mixed mainly semidiurnal regime where the maximum tidal range during spring tide rarely exceeds $\sim$2 m; the range is reduced to $\sim$1 m during neap tide (Hosseini and Siadatmousavi, 2018).

2.2. Regional meteorological and hydrological conditions

The monthly mean river discharge rarely exceeds 60 m^3/s at the Qantareh station (see its location in Fig. 1a), as it was only observed in November 2013 and January 2014 during the one-year period from October 2013 to September 2014 (see Fig. 2d). The monthly discharges dropped to less than 2 m^3/s in the warm months (May 2014 – September 2014), which classifies this estuary as a low-inflow system in the

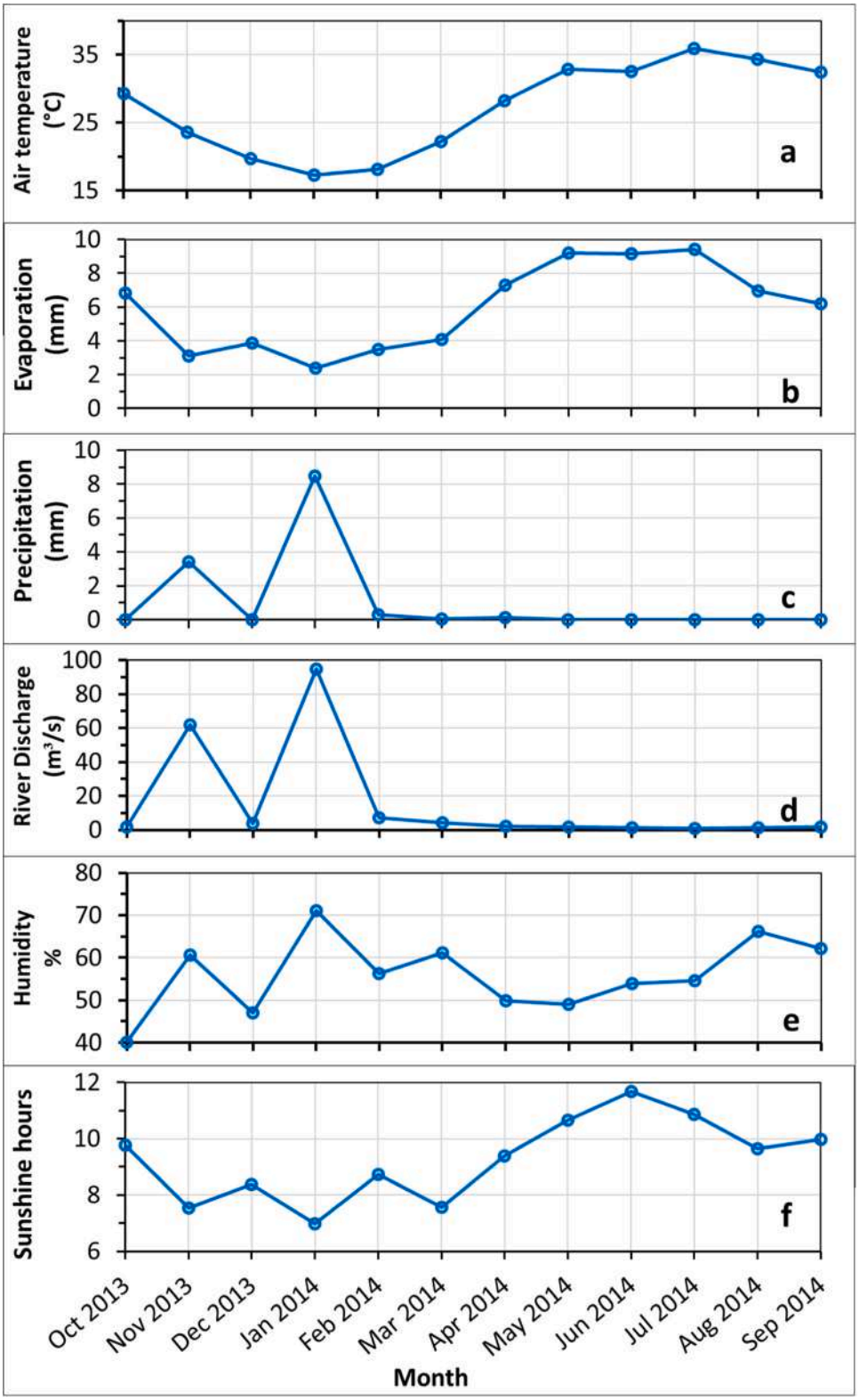

Fig. 2. The monthly mean values of observed air temperature (**a**), evaporation (**b**) and precipitation (**c**) rates, river discharge (**d**), relative humidity (**e**) and sunshine hours (**f**) at the meteorological synoptic stations near the Mond River Estuary and at the Qantareh station of river discharge recorder from October 2013 to September 2014.

category of "arid coasts" (Largier, 2010).

In the one-year period (October 2013 - September 2014), the meteorological synoptic station near the Mond Estuary recorded 179 sunny days (clear sky with cloudiness = 0 okta) and only 8 total overcast days (cloudiness = 8 oktas). As a result, the annual average of sunshine hours was 9.3 hour/day at the synoptic station. The minimum and maximum monthly mean sunshine hours were recorded in January (7 hours) and Jun (11.7 hours) 2014, respectively (Fig. 2f).

In January 2014, the monthly air temperature (Fig. 2a) and evaporation rate (Fig. 2b) experienced their minimum values, while the precipitation rate (Fig. 2c), river discharge (Fig. 2d), and relative humidity (Fig. 2e) reached their maximum values. In July 2014, the air temperature and evaporation rate reached their highest levels, peaking at 35.9°C and 9.4 mm/day respectively (see Figs. 2a and 2b). In contrast, the river discharge decreased to 1.04 m^3/s (see Fig. 2d) with no rainfall occurring during the month (see Fig. 2c). These observations indicate that July 2014 was the hottest and driest month in the one-year period. During the one-year period, the daily minimum and maximum air temperatures observed were 7.8 °C and 47.8 °C on 6th February 2014 and 12th June 2014, respectively. Also, the relative humidity ranged between daily minimum of 10% on 4th October 2013 and daily maximum of 97% on 26th January 2014. At the same time, the daily maximum precipitation and evaporation were 93.5 mm and 22.6 mm on 18th January 2014 and 23th July 2014, respectively. The corresponding annual averages of air temperature, precipitation, evaporation, and relative humidity were 27.3 °C, 1 mm, 6 mm and 56%, respectively. Monthly variations in evaporation rates are dominated by corresponding variations in air temperature (see Figs. 2a and 2b). A similar correlation occurs between monthly river discharge and precipitation rates (see Figs. 2c and 2d).

In addition, the northwestern wind was dominant during the year, with an annual mean of 8 m/s and daily minimum and maximum magnitudes of 2 m/s and 18 m/s, respectively.

2.3. Estuarine data

2.3.1. Data collection

This study uses a measured data set in the Mond Estuary by Hosseini and Siadatmousavi (2018). These observations consist of a time series of velocity, water-level, temperature, and salinity that were simultaneously measured at 4 stations along the estuary (See Fig. 1). The measurements were taken during two different 25-hour periods in February 2014 under weak and strong hypersaline runoffs. Each station was equipped with an Aanderaa RCM9 KM- II CTD-current meter instrument, located 1 m above the bottom to record data every 10 minutes. We use these data to calculate different salt flux terms. Also, tidal level data recorded by a TD sensor (STAR-ODDI) close to St1 (at depth of 3.45 m) during 2nd February – 4th March 2014 is used to compare with corresponding model results (see more details about the observations in Hosseini and Siadatmousavi (2018)).

2.3.2. Freshwater lenses

The 25 hours immediately before a saltwater discharge from 2nd to 3rd February 2014 during spring tide coincided with a precipitation event. Under this condition, a hypersaline runoff emerged at the estuary head (weak FLE condition), (see Fig. 3).

From 22nd to 23rd February 2014, during neap tide, a river flood with high saline water (hypersaline runoff) originating from the estuary upstream discharged into the estuary, which was preceded by a low-salinity water (strong FLE condition, see Fig. 3).

According to (Savenije, 2005), the shape of $\boldsymbol{S/S_i}$ as a function of $\boldsymbol{x/L}$ can be used to distinguish between different types of estuaries, in which $\mathbf{S(x)}$ is tidally-averaged salinity within the estuary at distance of $\boldsymbol{x}$ from the estuary mouth. $\boldsymbol{S_i}$ and $\boldsymbol{L}$ are tidally-averaged salinity at the mouth and the estuary length respectively. Fig. 3 presents such curves for both strong and weak FLE conditions in the Mond Estuary. In contrast to the along-channel salinity gradient in a salt-plug estuary, the salinity in a FLE state decreases monotonically from the mouth to the freshwater lens and then it increases due to hypersaline runoff (Hosseini et al., 2023). The weak FLE condition is similar to a normal (positive) estuary but salinity close to the estuary head slightly increases in the landward direction (see Fig. 3), indicating an emergence of hypersaline runoff at the head upstream.

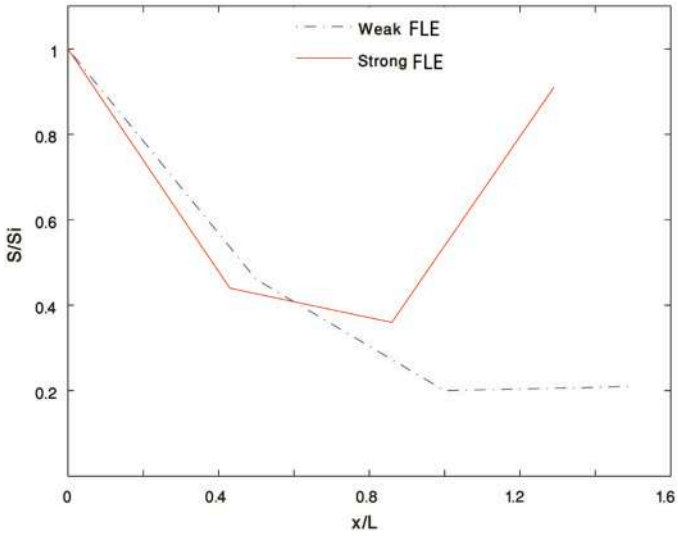

Fig. 3. The distribution salinity (S) inside the Mond Estuary normalized by the salinity at the mouth (Si), during the weak and strong FLE events on 2–3 and on 22–23 February 2014, respectively.

A tidal blockage was observed at the head of Mond Estuary during the strong FLE condition (Hosseini and Siadatmousavi, 2018). However, the associated processes cannot be effectively studied using few observations; there are no accurate records of river inflows and tidal fluctuations at the head of the estuary, especially during neap tides without hypersaline outflows. The nearest station recording the river discharge of the Mond River is 120 km upstream (Qantareh station, marked by the black square in Fig. 1a). Over such a long distance, hypersaline runoff from Kuh-e-Namkak and the seasonal Shour River could be joined in the Mond River during wet months (see their locations in Fig. 1a). Over a distance of 120 km, river water can also experience high rates of evaporation, especially during dry months. Thus, the river discharge into the Mond Estuary might be higher (lower) than the recorded values at Qantateh station during wet (dry) seasons.

2.3.3. Diagnostics

Vertical profiles of salinity $s(z)$, and the along-channel velocity $v(z)$ are used to calculate the net salt flux at each station. Transition from a well-mixed water column in spring tide to a weak strain-induced periodic stratification (SIPS) regime in neap tide was observed by Hosseini and Siadatmousavi (2018) close to the deepest station (St1, see Fig. 1b). In addition, the same authors reported well-mixed conditions in the vicinity of St2 and its upstream, which was explained by the shallow depths, less than 2.5 m, (see Fig. 1b). Therefore, $s(z)$ can be assumed vertically uniform for every 10-minute time step of measured data inside the Mond Estuary. The influence of vertical stratification induced by tidal straining (SIPS) on salt flux terms is addressed in Section 3.1.2.

The instantaneous $v(z)$ and $s(z)$ can be decomposed into depth-averaged values ($\overline{v}$ and $\overline{s}$) and deviations from the vertically mean values (v' and s'). The depth-averaged values may also be decomposed into time-averaged ($\langle\overline{v}\rangle$ and $\langle\overline{s}\rangle$), and time-varying components (V, S) (Ali et al., 2010; Bowden, 1967; Dyer, 1997; Hunkins, 1981; Pritchard, 1954; Restrepo and Kjerfve, 2002):

$$v = \langle \overline{v} \rangle + V + \acute{v} \tag{1}$$

$$s = \langle \overline{s} \rangle + S + \acute{s} \tag{2}$$

Note that $\langle \bullet \rangle$ represents the time-averaged quantity over one complete tidal cycle. The net salt flux Q per unit of width (psu m^2/s) through a water depth h, can be calculated as follows (Ali et al., 2010; Bowden, 1963; Dyer, 1997; Restrepo and Kjerfve, 2002):

$$Q = \int_0^h vs \, dz = \langle \overline{hvs} \rangle \tag{3}$$

Using Eqs. (1) and (2), Eq. (3) can be rewritten as follows:

$$\langle \overline{hvs} \rangle = \langle h \rangle \langle \overline{v} \rangle \langle \overline{s} \rangle + \langle hVS \rangle + \langle \overline{v} \rangle \langle HS \rangle + \langle \overline{s} \rangle \langle HV \rangle + \langle \overline{\acute{h}\acute{v}\acute{s}} \rangle \tag{4}$$

$$Q = Q_1 + Q_2 + Q_3 + Q_4 + Q_5 \tag{5}$$

Here H denotes tidal fluctuations. Each term on the right-hand sides of Eqs. (4) and (5) corresponds to a specific physical process: $Q_1 = \langle h \rangle \langle \overline{v} \rangle \langle \overline{s} \rangle$ is the advective flux, $Q_2 = \langle hVS \rangle$ is the tidal sloshing effect which is usually directed landward in positive estuarine systems, $Q_3 = \langle \overline{v} \rangle \langle HS \rangle$ is the cross-correlation between salinity and water-level, $Q_4 = \langle \overline{s} \rangle \langle HV \rangle$ is the Stokes' drift dispersion, and $Q_5 = \langle \overline{\acute{h}\acute{v}\acute{s}} \rangle$ is the mean shear-induced salt dispersion. The shear flux term, Q_5, has a negligible contribution to the net salt flux in a shallow microtidal estuary such as the Mond Estuary because this term is insignificant in a well-mixed embayment (Ali et al., 2010; Bowden, 1963).

The relative strength of advective and diffusive processes could be measured by the non-dimensional Péclet Number, *Pe*, defined as the ratio of the diffusive to the advective transport times (Kjerfve[1] and Knoppers, 1991). Advection and diffusion can be also compared by calculating their time scale ratios. The diffusive transport is stronger than the advection when *Pe* is less than 1. By contrast, the advective transport takes less time than the dispersive mixing when *Pe* is greater than 1 (Kjerfve[1] and Knoppers, 1991).

The time scale for the advective transport can be estimated as the ratio of the advection length scale, l, to the net current. Also, the required period for the diffusive mixing of the water inside the channel is scaled by $\frac{l^2}{K_x}$ where K_x is the coefficient of along-channel dispersion over a tidal cycle. Hence, *Pe* can be calculated as follows:

$$Pe = \frac{l^2/K_x}{l/v} = \frac{lv}{K_x} \tag{6}$$

On the other hand, from Eq. 5, *Pe* can be presented as the ratio between the advective salt flux and the remaining salt flux terms:

$$Pe = \frac{|Q_1|}{|Q_2 + Q_3 + Q_4 + Q_5|} \tag{7}$$

where $|\ |$ is the absolute value.

2.4. Numerical modeling

The numerical experiments performed in this study use the Semi-implicit Cross-scale Hydroscience Integrated System Model (SCHISM, Zhang et al. (2016)).

The model uses horizontal unstructured grids based on finite elements and finite volume methods, together with Eulerian-Lagrangian methods to solve the hydrostatic form of the Navier-Stokes equations with the Boussinesq approximation. It is capable to accurately simulate the seamless, 3D-baroclinic circulation from creek to ocean (Zhang et al., 2016).

We selected SCHISM, in part due to its proven quality of performance and extensive use in estuarine basins and coastal oceans (more information about SCHISM and relevant publications can be found at www.schism.wiki), and in part because this model is an open-source community-supported modeling system. SCHISM is set up for two basins: a realistic Mond Estuary and an idealized funnel-shaped straight basin, as used by Hosseini et al. (2023). In the following sections, we describe these two types of model setups and their numerical experiments.

2.4.1. Model setup for the Mond River Estuary

In the realistic model of the Mond Estuary, the boundary conditions and atmospheric forcing are prescribed using daily data from the Copernicus Marine Environment Monitoring Service (CMEMS, https://resources.marine.copernicus.eu) and hourly data from the European Centre for Medium-Range Weather Forecasts (ECMWF, https://cds.climate.copernicus.eu), respectively. This model was run for the period from January 2013 to December 2014 (two years). The horizontal resolution is approximately 8 m inside the estuary, which increases to approximately 850 m at the open boundary in the Persian Gulf. In the vertical direction, 20 sigma layers are prescribed. At the open boundary, the model was forced by 10 tidal constituents (Q1, O1, P1, S1, K1, N2, M2, S2, K2 and M4) from the Danish Hydraulic Institute (DHI) global tidal model (Cheng and Andersen, 2010). These tidal constituents were already used by Hosseini et al. (2023) and are presented in Table 2 of their study. Considering different riverine flows and a sea-level rise, seven numerical scenarios are defined as presented in Table 1. The first one (see the FLE scenario in Table 1) examines the seasonal variations in the estuarine salinity and especially the longitudinal circulation and salinity in the Mond FLE state. The second scenario examines the effects of sea level rise (20 cm) on the different estuarine systems in comparison with those in the first experiment. The other five numerical scenarios in Table 1 are designed to estimate river discharges that block the tidal wave, especially during neap tides. In these scenarios, different fresh- and salt-water discharges are prescribed at the riverine open boundary (Table 1) based on two-year data in 2013 and 2014.

In order to simulate an FLE system (in the two first scenarios presented in Table 1), the model is forced by time-dependent daily time series of the recorded discharges of the Mond River (see the Qantareh station in Fig. 1a) from 1 September 2013–1 October 2014; however, a salinity of 37 psu is assigned to the discharges when they are higher than 66 m^3/s in the three durations presented in Table 2. We analyzed the FLE regime in the third duration. The daily river inflow decreased from 1847 m^3/s on 7th January 2014, to0.67 m^3/s on 21st August 2014 at the Qantareh station. During February 2014, the maximum daily river discharge of 32 m^3/s was recorded at this station three days before the strong FLE condition (Hosseini and Siadatmousavi, 2018). This relatively high river discharge decreased to ~6 m^3/s at the time of strong FLE condition. It signifies that large amounts of salty runoff enter into the Mond River estuary from the Kuh-e-Namak and the seasonal river of Shour in the 120 km part between the Qantareh station and the estuary head during weak and especially strong FLE events.

Scenario Q10 (see Table 1), which replicates a positive estuarine condition, is like the weak FLE condition. The river inflow, in this case, is

Table 1
Seven SCHISM scenarios for the Mond River Estuary. Among these scenarios, only FLE is used in the idealized model.

Scenario	FLE	FLE with rising sea level	Q10	Q100	Q200	Q400	Q800
River inflow (m^3/s)	Daily time-series	Daily time-series	10	100	200	400	800
River salinity (psu)	Daily time-series	Daily time-series	6	37	37	37	37

Table 2
Three durations with river inflows higher than 66 m^3/s, for which salinity of 37 psu was prescribed to produce hypersaline runoff and consequently prepare the conditions of the FLE system in both models of Mond River Estuary and Idealized basin.

Duration	Time	Daily mean river discharge (m^3/s)
1	20-Nov-2013	197
	21-Nov-2013	570
	22-Nov-2013	485
	23-Nov-2013	215
2	7-Jan-2014	1847
	8-Jan-2014	177
3	19-Jan-2014	214
	20-Jan-2014	117
	21-Jan-2014	66.1

close to the monthly mean recorded values in February 2014 (7.05 m^3/s) and its salinity is close to the salinity at St3 and St4 at the upper estuary (see Fig. 1b) during the weak FLE condition (see Table 1 and Fig. 4d). The other scenarios of Q100, Q200, Q400 and Q800 (Table 1) are examined to estimate the role hypersaline runoff in dissipating the tidal signal.

2.4.2. Model setup for the idealized basin

The second model setup is an idealized trumpet-shaped basin. The estuary length is 100 km in which the width of the estuary decreases from 12 km at the mouth to ~100 m at the head. The maximum depth on the main axis decreases from 20 m at the estuary mouth to about 4 m at the head. The idealized basin uses 25 sigma layers in the vertical direction and its horizontal resolution changes from 2 km at the marine open boundary to 10 m at the estuary head. Further details regarding the idealized basin are given in the study of Hosseini et al. (2023).

This idealized funnel-shaped estuary with symmetrical cross-channel topography is placed between 28.08°N to 28.2°N and 51.2°E to 52.1°E, close to the location of the Mond Estuary. It uses hourly atmospheric forcing originating from the ECMWF in 2013–2014, similar to the one in the realistic Mond model. Furthermore, temperature and salinity at the open boundary, which are the same as those in the Mond model, are taken from the daily reanalysis data of the Persian Gulf provided by the CMEMS during 2013–2014 (730 days). The tidal forcing is prescribed as an M2 tide with a 0.465 m amplitude, which is the same as the magnitude of the M2 tide at the open boundary of the Mond model. Wind and Coriolis force are turned off to avoid additional complications to the idealistic FLE-circulation, and to compare with the idealized salt-plug circulations (Hosseini et al., 2023) under the same conditions. The same setup of the FLE scenario (the first scenario presented in Table 1) in the realistic Mond model is also used in the idealized estuary to build an idealized FLE system and examine its longitudinal salinity and circulation.

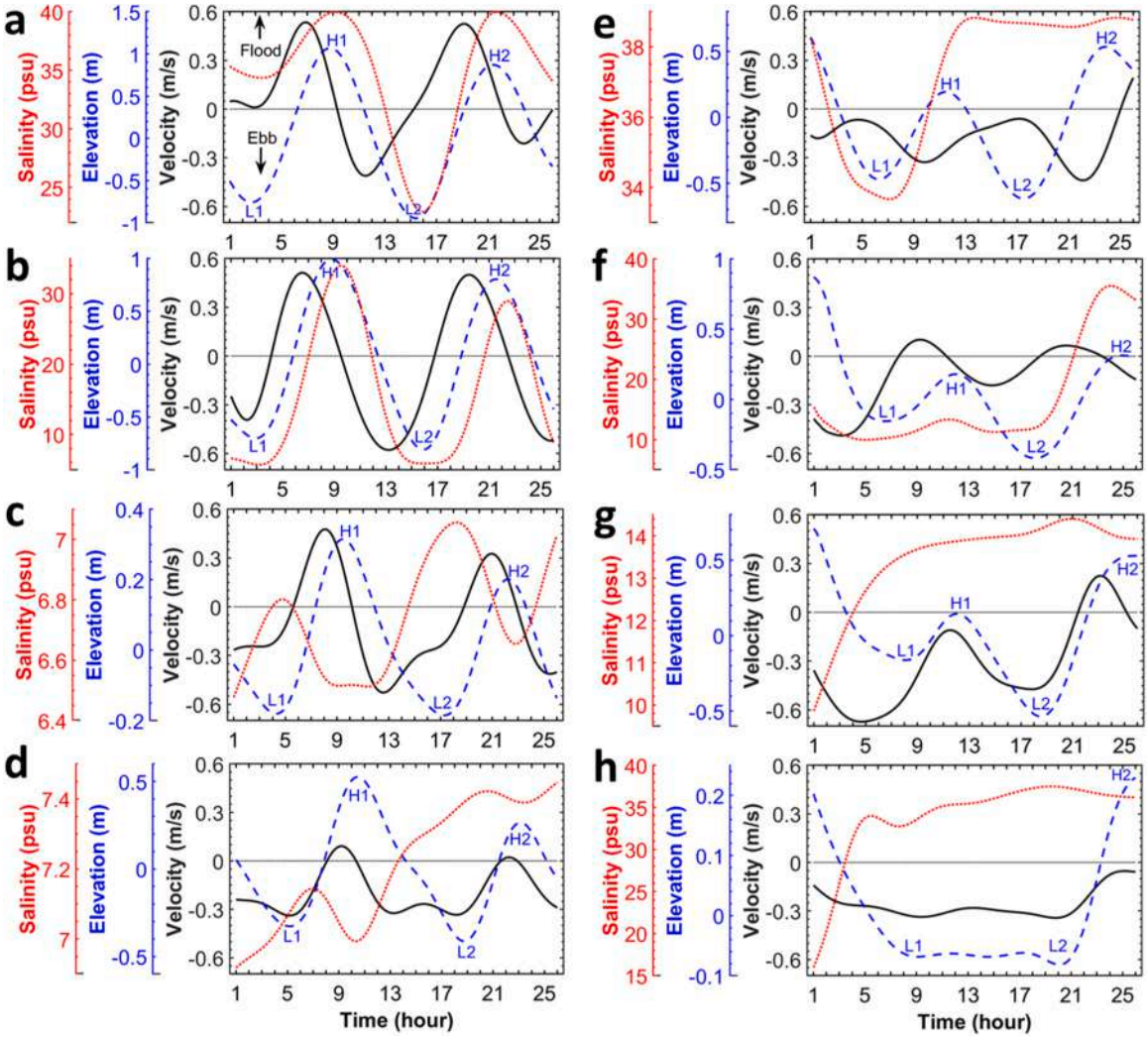

Fig. 4. Salinity, water-level and along-channel velocity variations over a tidal cycle at St1-St4 during the weak (a-d) and strong (e-h) FLE conditions.

3. Results

3.1. Analysis of observations

3.1.1. Time series data

The salinity, water level, and longitudinal velocity variations measured at St1 (near the mouth) to St4 (near the head of the estuary) over two 25-hour tidal cycles during both weak and strong FLEs are shown in Fig. 4. In this figure, high and low waters are denoted by H_i and L_i (i=1, 2) respectively.

During the weak FLE condition, salinity variations and tidal water levels were in phase at St1 and St2 (Fig. 4a, b), indicating the positive estuary. According to Fig. 4c, the salinity had a phase lag of ~180° with water-level fluctuation at St3. It indicated that salinity increases as one moves landward from St3, which is similar to an inverse estuary. Also, salinity varied from ~6.5 to ~7 psu at St3 which implied high (low) riverine water (seawater) content. The salinity variations were out of phase with water levels at St4 until L2, (Fig. 4d). Afterward, the salinity variations were insignificant (the change in salinity was less than 0.1 psu). This pattern was caused by hypersaline runoff occurring upstream of St4. Under this condition, the along-channel flows mostly became seaward at St4 although these flows fluctuated by tides. On the other hand, the first three stations (St1-St3) showed tidal low-water slacks and high-water slacks (zero velocities) close to low waters (L1 and L2) and high waters (H1 and H2), respectively. It shows a phase difference of ~90 ° between tidal velocity and elevation at St1-St3 signifying the presence of a standing wave in the Mond Estuary in the absence of any strong hypersaline runoffs. The standing wave is commonly formed in short and/or shallow estuaries with negligible reflection (Friedrichs, 2010). Similar results were reported for a tidal creek in the Bushehr Port, Persian Gulf by Hosseini et al. (2016).

During the 25-hour period of strong FLE condition, the along-channel velocities and the salinity variations were significantly affected by the strong hypersaline runoff (Fig. 4e-h). Therefore, the flows were mostly seaward at the four stations particularly at the head station (St4), which experienced no landward velocities (Fig. 4h). Also, tidally-induced oscillations of salinity undergo substantial deviations (Fig. 4e-h), in contrast to those during the weak FLE condition (see Fig. 4a-d). In addition, water levels, especially the lower high water (H1), were significantly dampened by the strong hypersaline runoff at St4 during the neap tidal period (see Fig. 4h). Since the amount of hypersaline runoff that attenuates the tidal waves cannot be determined from observations due to the observational limitations mentioned in Section 2.3.2, the five numerical scenarios are deployed to estimate a minimum value of this runoff amount (see Section 3.2.3).

According to Dyer (1997), who defines the estuary length (tidal intrusion length) as the distance from the mouth that is rarely reached by tidal waves, location S4 can be considered as the estuary-river boundary (see Figs. 4d and 4h). At this station, salinity increases from ~15.5 psu to ~37.5 psu due to saline water runoff from the watershed (see Fig. 4h). The highest range of salinity at measured stations was observed at St2 during both FLE conditions (see Fig. 4b and Fig. 4f), signifying the estuarine mixing zone (Dionne, 1963).

3.1.2. Net salt flux

The depth- and time-averaged velocity ($\langle\bar{v}\rangle$), and salinity, ($\langle\bar{s}\rangle$), measured along the estuary are presented in Table 3. At steady state condition, the net salt flux over a complete tidal cycle is zero because the advective flux balances the dispersive ones. Since the net salt fluxes, Q, shown in Table 4 are different from zero, one can conclude that the four stations (St1-St4) are in a non-steady state for the full tidal cycle (25 h) during both FLE states.

The advective flux (Q1) has the largest contribution to the net salinity flux among the four salinity flux components at all stations in this estuary, as shown in Table 4. Similar to the direction of $\langle\bar{v}\rangle$ (see Table 3), Q_1 is landward only near the mouth (St1) in the weak FLE condition (see Table 4). The strongest landward and seaward fluxes are respectively the advective terms (Q_1) at St1 during the weak FLE condition and at St4 (head of the estuary) during the strong FLE state, as Q_1 is directly related to the $\langle\bar{s}\rangle$ and $\langle\bar{v}\rangle$ (see Eqs. 4 and 5 and Tables 3 and 4).

Table 3
The depth- and time-averaged values of velocity and salinity ($\langle\bar{v}\rangle$, $\langle\bar{s}\rangle$) at different stations during the weak and strong FLE conditions in February 2014. Seaward and landward velocities are specified with positive and negative values respectively.

Station	Weak FLE condition		Strong FLE condition	
	$\langle\bar{v}\rangle$ (cm/s)	$\langle\bar{s}\rangle$ (psu)	$\langle\bar{v}\rangle$ (cm/s)	$\langle\bar{s}\rangle$ (psu)
St1	-7.9	34.53	17.9	37.19
St2	5.3	16.05	11.7	16.31
St3	9.9	6.74	31.8	13.50
St4	19.4	7.21	26.2	34.02

Among salt dispersive fluxes, Q_2 (tidal sloshing term) played the most important role in the salt transport at St2 during both FLE conditions (Table 4). Q_2 at St2 was slightly smaller in the strong FLE than the weak FLE because of lower range of tidal salinity variations in the strong FLE state (compare salinity ranges in Fig. 4b and Fig. 4f). The term Q_3 (the cross-correlation between water-level and salinity) was mostly the smallest term among the four salt flux components at all stations (see Table 4). This flux was directed similarly to $\langle\bar{v}\rangle$ and Q_1 at the downstream stations (St1 and St2), while it was directed in the opposite direction compared to $\langle\bar{v}\rangle$ and Q_1 at the upstream estuary (St3 and St4) during both FLE conditions (see Table 3 and Table 4). The reason for these peculiarities was the same patterns of time-varying salinity and water levels (S and H), especially during the weak FLE state at the downstream stations (in which the positive estuarine condition is dominated between marine salt water and freshwater lens). In the upstream stations located between the lens and the saltwater runoff, where the estuary basically acts as a quasi-inverse estuary, the parameters of S and H had opposite patterns (see Fig. 4). The salinity increases in the landward direction at inverse estuarine systems due to high evaporation while in the quasi-inverse estuarine zone, this increase occurred due to saltwater runoff.

The Stokes drift dispersion flux (Q4) was often directed upstream. (Table 4). The tidal sloshing (Q_2) and Stokes drift (Q_4) fluxes were the main terms which dispersed salt inside the Mond Estuary, especially close to St2 during the weak FLE condition (Table 4). The advective flux, Q_1, determined the direction of the net salt flux, Q, at all stations except at St2 during spring tide of weak FLE condition, in which the direction of Q was landward in contrast to the advective flux direction. The sum of the main dispersive landward terms (Q_2+Q_4) at St2 in the weak FLE condition was higher than seaward advective term (Q_1), due to the strong tidal forcing during spring tide and the weak salt-river flood (Table 4).

The presence of strong hypersaline runoff induced significant seaward net salt fluxes at all stations in the strong FLE condition. The seaward advective fluxes at upstream stations (St3 and St4) were ~6 times larger during the strong FLE condition compared to the corresponding fluxes during the weak FLE condition (Table 4). In the strong FLE condition, 680.18 psu cm/s is transported from the estuary mouth (St1) to the Persian Gulf (Table 4). On the other hand, the net salt flux becomes landward in the downstream stations (St1 and St2) in the absence of strong river discharge (during the weak FLE condition).

During spring tide, SIPS resulted in maximum salinity differences of ~ 9 psu and ~2 psu at the ends of ebb and flood tides, respectively. To estimate the effect of the vertical salinity gradient induced by SIPS on the salt flux results, the maximum salinity differences are used to calculate the salt fluxes for the spring 25-h period of weak FLE state at St1 (Table 5). The results are close to corresponding fluxes presented in Table 4 indicating the insignificant effect of SIPS. For instance, the landward advective salt flux (Q_1) decreases by about 6% (16.89 psu cm/

Table 4
Decomposed net fluxes of salt divided by the corresponding mean water depth, $\langle h \rangle$, (psu cm/s), in the weak and strong FLE conditions. Positive and negative values indicate the seaward and the landward directions, respectively.

Station	St1		St2		St3		St4	
FLE Condition	weak	strong	Weak	strong	weak	strong	Weak	strong
$\mathbf{Q}/\langle h \rangle$: $\langle \overline{hvs} \rangle / \langle h \rangle$	-291.95	680.18	-21.63	157.43	58.55	390.91	133.03	875.81
$\mathbf{Q_1}/\langle h \rangle$: $\langle \bar{v} \rangle \langle \bar{s} \rangle$	-272.97	667.24	85.20	190.47	66.40	429.06	139.68	889.05
$\mathbf{Q_2}/\langle h \rangle$: $\langle hVS \rangle / \langle h \rangle$	3.31	4.06	-69.72	-54.23	0.66	-14.84	0.07	5.19
$\mathbf{Q_3}/\langle h \rangle$: $\langle \bar{v} \rangle \langle HS \rangle / \langle h \rangle$	-3.37	0.47	7.45	4.65	-0.10	-2.28	-0.08	-3.93
$\mathbf{Q_4}/\langle h \rangle$: $\langle \bar{s} \rangle \langle HV \rangle / \langle h \rangle$	-18.92	8.42	-44.56	16.56	-8.41	-21.02	-6.63	-14.51

Table 5
Decomposed net fluxes of salt divided by the corresponding mean water depth, $\langle h \rangle$, (psu cm/s) at station 1 in weak FLE considering SIPS regime with linear distribution for salinity profile. Positive and negative values indicate seaward and landward flux directions, respectively.

	station 1 in weak FLE state
$\mathbf{Q}/\langle \mathbf{h} \rangle$: $\langle \overline{hvs} \rangle / \langle h \rangle$	-277.04
$\mathbf{Q1}/\langle \mathbf{h} \rangle$: $\langle v \rangle \langle \bar{s} \rangle$	-256.08
$\mathbf{Q2}/\langle \mathbf{h} \rangle$: $\langle hVS \rangle / \langle h \rangle$	0.79
$\mathbf{Q3}/\langle \mathbf{h} \rangle$: $\langle \bar{v} \rangle \langle HS \rangle / \langle h \rangle$	-4.00
$\mathbf{Q4}/\langle \mathbf{h} \rangle$: $\langle \bar{s} \rangle \langle HV \rangle / \langle h \rangle$	-17.75

s) due to the SIPS effect.

3.1.3. Advection vs. Diffusion

The advective transport dominates ($Pe > 1$) throughout the estuary except at St2 during the weak FLE condition under which *Pe* is less than 1 as shown in Table 6. In fact, the strong dispersive landward fluxes (Q_2+Q_4) overcome the seaward advective flux (Q_1) at St2 during the weak FLE condition (see Table 4). Moreover, St2 has the lowest value of *Pe* among all stations during both FLE states due to a considerably mixed condition between the freshwater lens and the marine salt water (see Section 3.1.1).

To be more specific, the Péclet numbers at stations 1–4 are approximately 3.6, 7.2, 1.3 and 3.2 times higher during the strong FLE than the weak FLE condition due to the advective transport induced by the salt-river flood during the strong FLE state.

3.2. Analysis of model data

3.2.1. Model evaluation

Fig. 5 illustrates the time series of tidal level from the FLE scenario (see Table 1) in the Mond Estuary and corresponding observations close to St1 (three kilometers from the estuary mouth) between 02 February 2014 and 04 March 2014. In this period, the time-averaged river discharge was ~7 m^3/s in the model. Although the tidal amplitude from the model is slightly lower than in the observations, the statistical parameters of correlation, model skill and RMSE are 0.984, 0.989 and 0.090 m respectively.

A comparison between the modeled velocities and salinities from the FLE scenario and the corresponding observations at St1 and St2 during the weak FLE condition is shown in Fig. 6. The statistical parameters indicates that the model agrees well with the observations (see Table 7). The validation of model is presented only for St1 and St2 in the weak FLE condition when these stations were not affected by hypersaline runoff. Under the weak FLE state (on 2–3 February 2014), a hypersaline runoff emerged at the estuary upstream, leading to a quasi-inverse estuarine condition at the up-estuary (as shown by a phase difference of ~180° between salinity and water-level fluctuation in Fig. 4c, d). At the same period, the model (FLE scenario) was forced by a low river inflow of 5.60 m^3/s with a salinity of 7 psu, which cannot impose a quasi-inverse estuary near the estuary head. This inconsistency is due to the limitations in the observed data, which are used to force the model. Similarly, the FLE scenario is forced by 6.15 m^3/s on 22–23 February 2014, (which coincided with the strong FLE state). However, tidal waves were dampened by a strong salt-river flood at the estuary head at the same time (see Fig. 4h). The Mond model can demonstrate an unsteady state of the FLE condition well when it is forced by a high-salinity river discharge (see next section). Also, a numerical estimation of reasonable hypersaline runoffs damping tidal waves is presented in Section 3.2.3.

3.2.2. The FLE system in the Mond Estuary

In order to investigate FLE dynamics in the Mond Estuary, we demonstrate tidally averaged longitudinal circulation and salinity from the numerically simulated FLE scenario when hypersaline runoffs enter the estuary. In an FLE system, a low-salinity lens is formed, followed by hypersaline runoff within a positive estuarine system. To illustrate this system, we arbitrarily focus on the duration of 19–21 January 2014 (see Table 2) in Fig. 7. During the first 15 hours of 19 January, the estuarine embayment acts as a positive estuary (see Fig. 7), in which the depth-averaged salinity decreases in the landward direction from the mouth (0 km) towards the head (about 18 km). Between about hour 15 and hour 40, a low-salinity lens is sandwiched by both the Persian Gulf water near the mouth and the saltwater flood close to the head, indicating the FLE system (Fig. 7). During the final 10 hours (from about hour 40 to hour 50), the FLE state completely dissipates and only the hypersaline water floods along the estuary. Throughout these 50 hours with about 100–200 m^3/s runoffs (see Table 2), the salinity from the Persian Gulf can only intrude about 3 km into the estuary and rarely exceeds St1 at high-water times (~ hours 17 and 30 in Fig. 7). Also, a high longitudinal salinity gradient is detected around St1 at low-water time of hour 10, when the Mond Estuary experiences a positive system (see Fig. 7). At this hour, salinity near St1 increases from 13 psu to 20 psu within a seaward distance of less than 1 km mainly owing to tidal straining. This occurs close to the end of ebb tide (low-water time), (see Fig. 7), when tidal wave strengthens the longitudinal salinity gradient and, consequently, the vertical stratification in a positive estuarine system. The deepest zone in the estuary is located near St1, where Hosseini and Siadatmousavi (2018) observed the impact of tidal straining.

Additionally, the low-salinity lens is quickly dissipated by hypersaline runoff in less than two days in the short and very shallow Mond Estuary (see Fig. 7). This indicates that the FLE system is an unsteady state inside a positive estuary imposed by a hypersaline runoff. It can

Table 6
The values of Péclet number (***Pe***) at all stations from station 1 (close to the mouth) to station 4 (close to the head).

Station	1		2		3		4	
FLE Condition	weak	strong	Weak	strong	weak	strong	weak	strong
Péclet Number	14.38	51.55	0.80	5.77	8.46	11.25	21.02	67.16

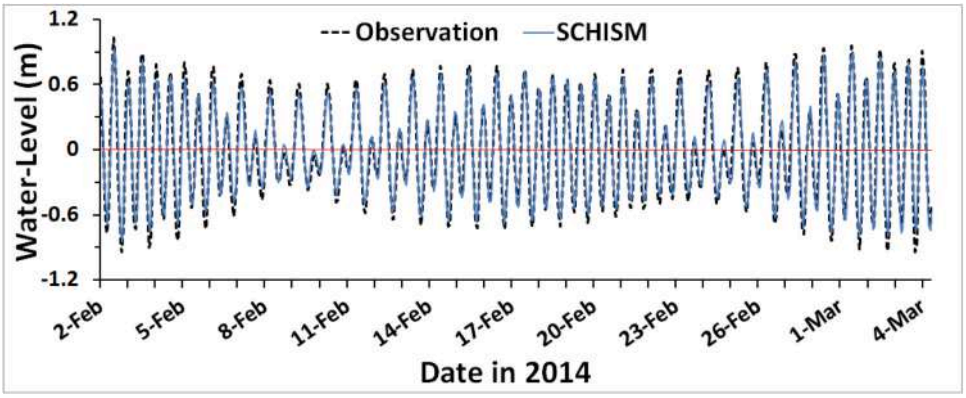

Fig. 5. Comparison between observed and simulated sea level from the FLE scenario (see Table 1) at the Mond River Estuary close to St.1 (See Fig. 1) from 02 February 2014–04 March 2014.

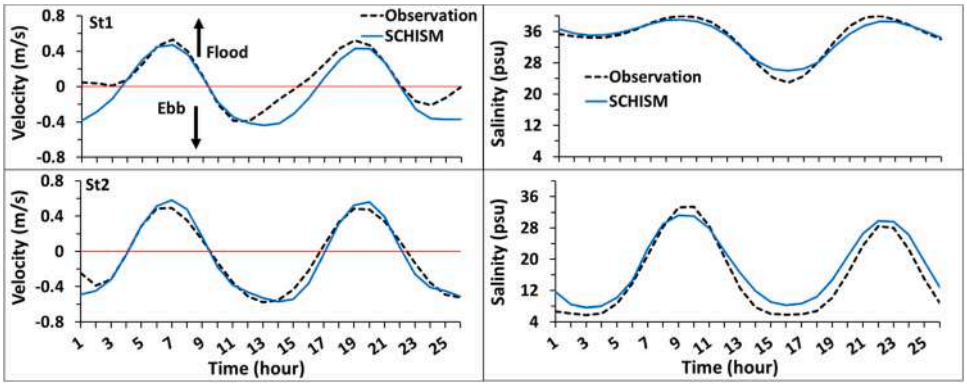

Fig. 6. Along-channel velocity (left panels) and salinity (right panels) variations from the observation and model over a tidal cycle at St1 and St during the weak FLE condition.

Table 7
The statistical parameters of correlation, model skill and RMSE between observed and modeled data presented in Fig. 6.

Station	Correlation		Skill		RMSE	
	Velocity (-)	Salinity (-)	Velocity (-)	Salinity (-)	Velocity (m/s)	Salinity (psu)
St1	0.92	0.98	0.91	0.98	0.18	1.21
St2	0.98	0.99	0.99	0.97	0.08	2.97

only be sustained for a few hours to a few days, but not for a long time. The persistence (residence time) of an FLE state depends on the amount of low-salinity mass and its subsequent hypersaline discharge, as well as the length of the estuary and other geometric characteristics. The FLE condition begins with emerging hypersaline runoff at the head of a positive estuary (defined as the weak FLE condition in this study) and ends by dissipating the low-salinity lens near the mouth (see hours close to hour 50 in Fig. 7). The salinity profile along the main channel axis (thalweg) of the FLE system, averaged from hour 10 to hour 34 of Fig. 7, shows that the Persian Gulf water barely reaches St1 (Fig. 8a). Also, the relatively freshwater (low-salinity lens) with a salinity of about 20 psu is surrounded by seawater (from the mouth to St1) and a saltwater flood (between St2 and the head), as shown in Fig. 8a. The relevant profile of axial velocity reveals a weakly normal (positive) circulation close to the estuary mouth due to the interaction between the low-salinity lens and dense waters of the Persian Gulf (Fig. 8b). The well-mixed condition combined with the existence of a salt-river flood of ~100–200 m^3/s in the FLE state, predominantly induce a seaward flow throughout the water columns along the estuary. Between 9 km and 15 km, axial velocities tend to approach zero at four locations due to the complex geometry and abrupt increases in water depths there (see Fig. 8b).

To display a developed FLE-circulation, the idealized basin is forced by the same FLE conditions as in the numerical FLE scenario discussed in Section 4.1.

Based on Table 2, hypersaline runoff can create FLE conditions during two periods in January 2014 (January 7th-8th and January 19th-20th) following a low-salinity lens. Time series variations of surface salinity at the estuary mouth (Fig. 9) show that the durations around January 7th and January 20th are characterized by rapid decreases in salinity (low-salinity lens). These low-salinity lenses exit the estuary almost coincidentally with spring tides (see Fig. 9).

3.2.3. *The role of hypersaline runoff on tidal damping*

This section estimates the contributions of both neap tide and saltwater runoff on tidal damping in the Mond Estuary using five numerical scenarios of Q10, Q100, Q200, Q400 and Q800 (see Table 1).

The tidal range decreases as the river discharge increases. For instance, the maximum tidal range of ~1.8 m in the Q10 scenario at the head of the estuary decreases to 1.1 m, 0.7 m, 0.3 m, and 0.1 m in the Q100, Q200, Q400 and Q800 experiments, respectively (Fig. 10). The estimated amount of hypersaline runoff is ~400 m^3/s during the strong FLE condition as the tidal range of strong FLE state is ~0.3 m at St4 (see Fig. 4h, 10).

The ratios of maximum tidal amplitudes at the estuary head from Q100, Q200, Q400 and Q800 scenarios to that from Q10 (Ar) against corresponding normalized river discharges by 10 m^3/s discharge of Q10 (Dr) are plotted in Fig. 11 (denoted by black line with circle). The polynomial trend line (dotted red line in Fig. 11) quantifies the reverse

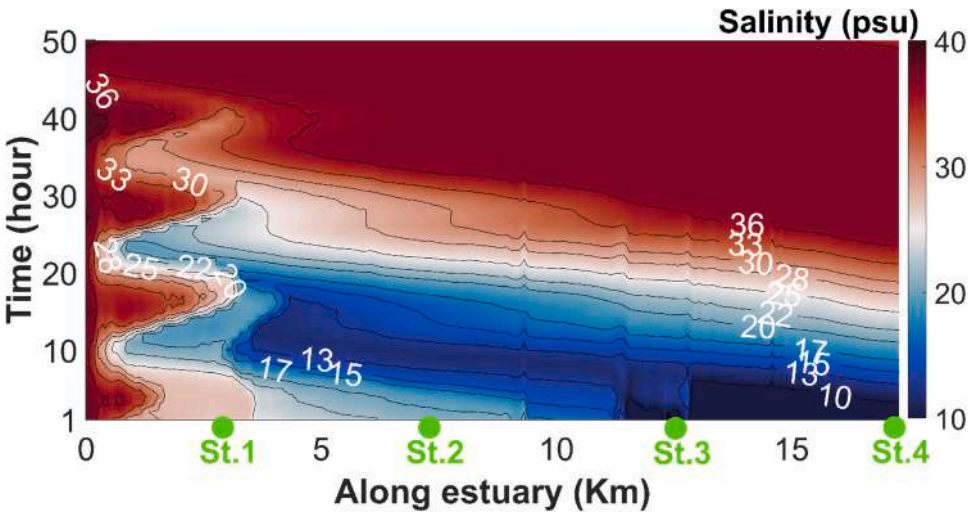

Fig. 7. Hovmöller diagram of depth-averaged salinity along the main axis of the Mond River Estuary during 50 hours from 19 January 2014 representing both simulations of positive estuary and FLE system from the FLE scenario (see Table 1).

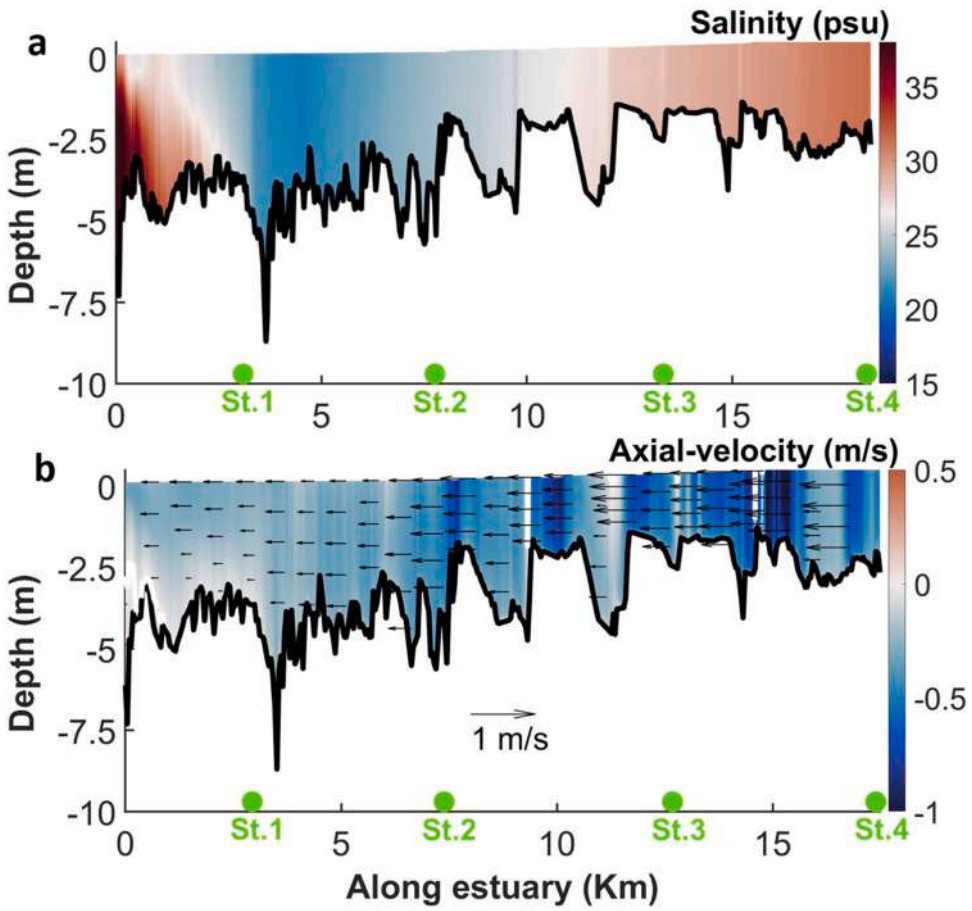

Fig. 8. Along-channel profiles of the time (25 hours) averaged (**a**) salinity and (**b**) axial velocity over the deep channel-axis of the estuary during 25 hours on 19 and 20 January 2014 from the FLE scenario (see Table 1).

relationship between the tidal range and river discharge values well. The relevant correlation-squared C^2 between the Ar-Dr plot and the regression trend tends to 1.

3.2.4. *Time-dependent estuarine variability*

The simulation of the time-dependent estuarine variability (Fig. 12) demonstrates that the numerical model accurately reproduces the basic dynamics and temporal changes observed in the Mond Estuary. Fig. 12 shows the evolution of the daily mean and depth-averaged salinity presented as time (January 1st 2014 to September 30th 2014) versus distance from the mouth of the Mond Estuary along the main axis of the estuary. This figure illustrates the transition from a positive estuary (from early winter to the end of spring) to an inverse estuarine system (in July) followed by a salt-plug estuary (after July). As demonstrated in

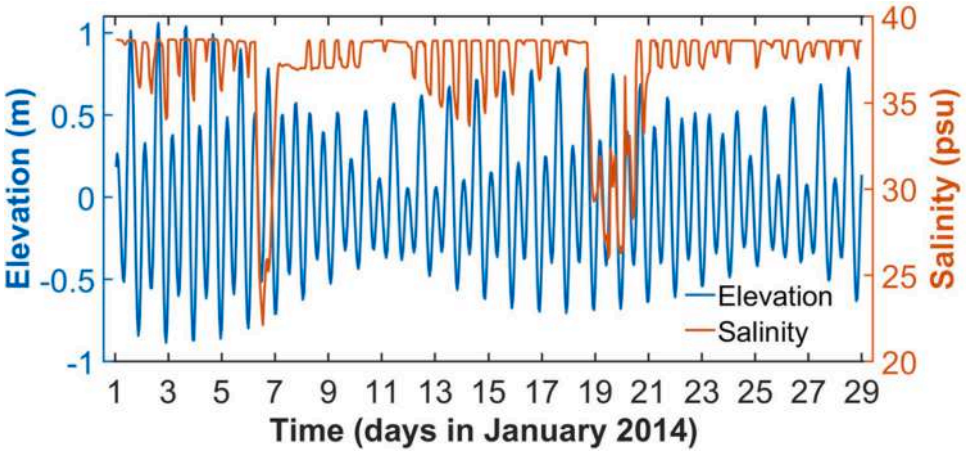

Fig. 9. Time series of tidal water-level and surface salinity at the estuary mouth over 28 days from 1 January 2014 resulted from the FLE scenario in the Mond River Estuary.

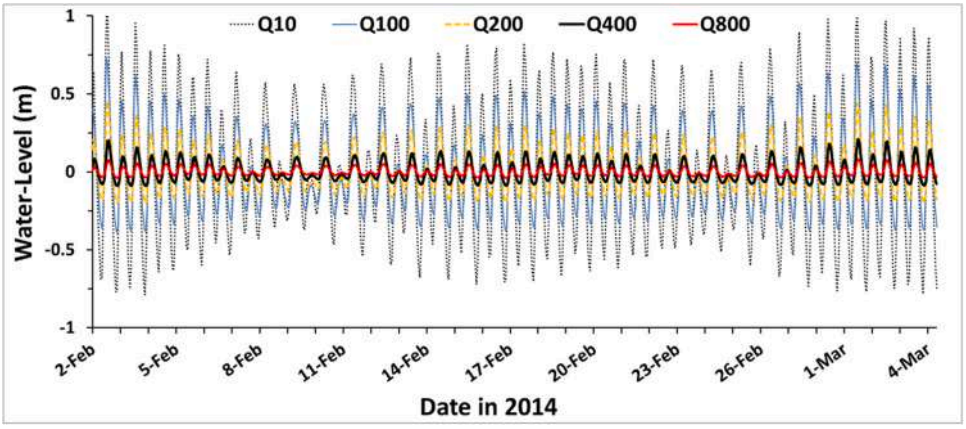

Fig. 10. tidal levels at the head of estuary from 5 scenarios of Q10, Q100, Q200, Q400 and Q800 in time period from 2 Feb to 5 March 2014.

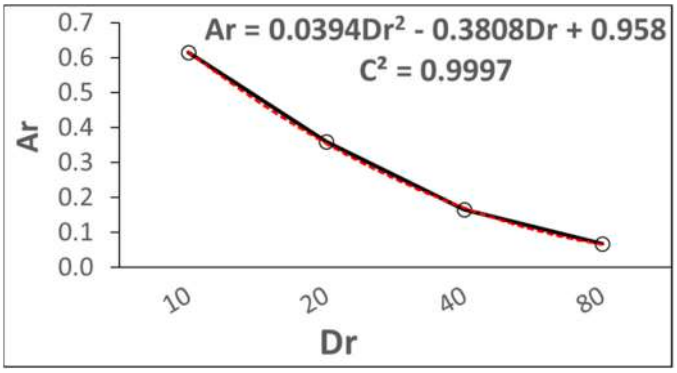

Fig. 11. The relationship between different river discharges of the four scenarios Q100, Q200, Q400 and Q800 (see Table 1) normalized by 10 m^3/s discharge of Q10 (Dr) and their consequent normalized maximum amplitudes at the estuary head Ar (black line with circle). The vertical and horizontal axes present the relative maximum amplitude Ar and the relative discharge Dr respectively. The regression trend of the relationship is denoted by the dotted red line. The regression formula and the correlation- squared C^2 are presented on the figure.

Fig. 2, July 2014 was the hottest and driest month in the one-year period from October 2013 to September 2014. During July 2014, the salinity slightly increased from the mouth towards the head, indicating the inverse estuary. Following this, a zone of maximum salinity is formed in the middle of the estuary (the salt-plug estuary), which persists for a longer duration than the inverse condition (see Fig. 12).

Also, two rapid increases in the longitudinal salinity in January 2014 (around January 7th and January 20th) resulted from entering hypersaline runoffs into the positive estuary, producing the two FLE regimes (see Fig. 12).

Different riverine forcings containing occasional high-salinity water floods, and seasonal variations in precipitation and evaporation result in the estuarine transitions between positive, FLE state, inverse, and salt-plug systems at the Mond Estuary.

Of particular importance is that with the prescribed forcings, observational studies reported that the Mond Estuary in the wet month of February 2014 could behave as both an FLE system (Hosseini and Siadatmousavi, 2018) and a positive estuary (Ghaemi and Gholamipour, 2017). Also, this estuary showed a salt-plug estuarine condition (with an SMZ forming at the mid-estuary) in the dry month of September 2014 (Ghaemi and Gholamipour, 2017).

4. Discussion

4.1. Modeling an idealized FLE-circulation

A question remains as to whether the opposite salinity patterns would imply a reversal in the dynamics between salt-plug and freshwater lens estuaries. This is answered by utilizing numerical modelling on the idealized estuarine basin. The longitudinal circulation in the idealized FLE system (from this study) is compared with the

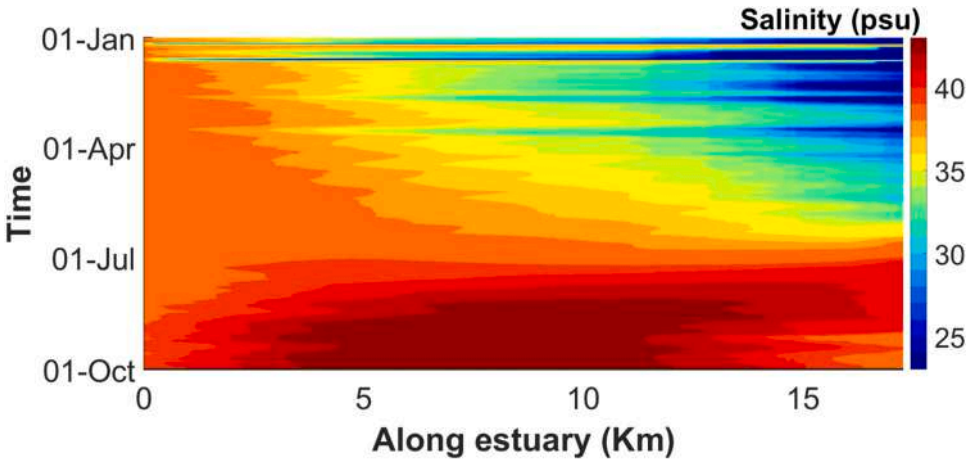

Fig. 12. Hovmöller diagram of daily mean depth-averaged salinity along the main axis of the Mond River Estuary during the first nine months of 2014 from the FLE scenario (see Table 1), which represents a strong temporal estuarine variability transferring from the positive system in wet months to the inverse and salt-plug estuaries in dry months.

corresponding circulation in the idealized salt-plug estuary (from the study by Hosseini et al., 2023).

Implementing the FLE scenario (see Table 1) on the idealized basin illustrates that during 25 hours between 20 and 21 January 2014 (see Table 2), an FLE system can be created (Fig. 13). In this system, low-salinity waters with salinities lower than 24 psu are sandwiched at around 80 km between high-salinity waters from the ocean and hypersaline river floods (see Fig. 13a). The longitudinal profiles of axial velocity averaged over two M2 tidal cycles (Fig. 13c) exhibit a double (twin) subtidal positive estuarine circulation: one cell is formed from the mouth to 40 km, and another cell extends from 50 km towards the low-salinity lens close to 80 km (see Fig. 13b, c). In the zone between 40 and 50 km, the longitudinal and vertical salinity changes are small (see Fig. 13a, b). The potential energy anomaly ∅ shows clear minima (∅<0.75 J/m^3) in this zone (Fig. 13d), indicating weak stratification or high mixing (well-mixed water) there. ∅ (J/m^3) is defined as the energy required to change the density profile$\rho(z)$ to vertically averaged density $\overline{\rho}$ (Simpson, 1981): $\varnothing = \frac{g}{D}\int_0^D [\overline{\rho} - \rho] z dz$, where $\overline{\rho} = \frac{1}{D}\int_0^D \rho(z) dz$ and g is the gravity acceleration, D is the total water depth at each model time step. Thus, larger values of ∅ indicate a more stratified water column.

In fact, this high mixing zone between 40 and 50 km separates the two positive estuarine circulations with maximum values of ∅ ($\varnothing > 18 J/m^3$ near the mouth and $\varnothing > 7.5 J/m^3$ between ~60–70 km), (see Fig. 13c, d). In other words, the FLE system comprises two positive estuarine cells on either side of the zone of minimum stratification (maximum mixing). In this 10-km (between 40 and 50 km) interval of high mixing, ∅ is approximately 24 times and 10 times lower than those in the seaward and landward positive estuarine segments, respectively (Fig. 13d). The idealized FLE-system experiences another high mixing zone ($\varnothing < 0.75 Jm^{-3}$) close to the estuary head, which is affected by the hypersaline runoff (see Fig. 13b, d). The maximum mixing zone at the mid-estuary separates the twin positive estuarine circulations in an FLE system, while the similar high mixing zone in a salt-plug estuary (occurred in the area of maximum salinity) splits up the inverse and positive estuarine segments.

Thus, two notable differences between the FLE and salt-plug systems are their opposite longitudinal salinities and dissimilar subtidal circulations.

4.2. *Impacts of rising sea-level on the Mond River Estuary*

According to Fig. 12, the four 25-hour tidal cycles possessing different time-dependent estuarine states are selected to examine the impact of a sea level rise of 20 cm on along-channel estuarine salinity.

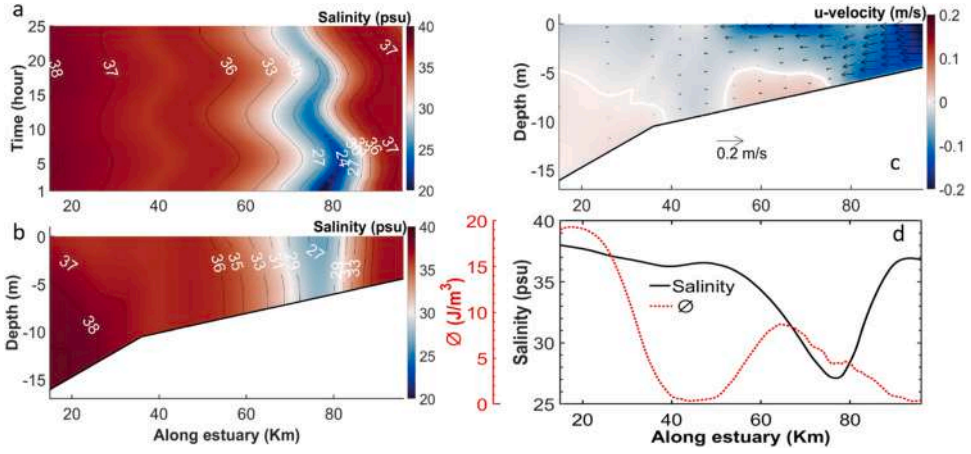

Fig. 13. (**a**) Time versus distance from the mouth along the axis of the idealized FLE diagram of depth-averaged salinity during 25 hours on 20 and 21 January 2014. Along-channel profiles of the 25-hour averaged (**b**) salinity and (**c**) axial velocity. (**d**) Time- and depth-averaged salinity and the potential energy anomaly (Ø) along the main channel axis of the idealized FLE state. The two positive estuarine circulation cells (in c) are separated by the minimum stratification (maximum mixing) zone in the middle of the estuary, which is shown in (d).

The two estuarine states are in the wet season including the FLE condition (on 19–20 January 2014) and positive estuary (on 10–11 March 2014). The two others occur in dry months: the inverse estuary on 10–11 July and the salt-plug estuary on 10–11 September 2014.

The sea-level rise of 20 cm at the FLE system of the Mond Estuary results in an increase of 2 psu in salinity at the lower estuary between the mouth and St1 (see around 3 km in Fig. 14a, e). Subsequently, the salinity increase driven by the sea-level rise of 20 cm tends to zero between St1 and St2 (~5 km). Moving from this zone (~5 km) towards the head, the sea-level rise causes an insignificant decrease in the estuarine salinity (see Fig. 14a, e). The salinity in the lower estuary (mouth – 5 km) increases because of longer intrusion of the Persian Gulf water imposed by rising sea-level. Before the sea-level rise, seawater rarely intrudes St1 (see Figs. 8a and 14a), but now it intrudes up to 5 km beyond St1 (see Fig. 14e). The energy of the sea-level rise and the resulting longer seawater intrusion push the low-salinity lens landward and consequently impose a slight decrease in salinity (< 0.5 psu). The salinity decrease is more pronounced in the narrow areas around St2 (see Fig. 14e). It is associated with the shallowness and complex geometry of the Mond Estuary, which causes minor changes in the longitudinal flows throughout the estuary.

In the positive estuary (Fig. 14b), the Persian Gulf water intrudes St3 (11 km) and dilutes by 34 psu. The sea-level rise enhances estuarine salinity in the landward direction (Fig. 14f), particularly salinity at St3 increases by 1 psu influenced by 20 cm rising sea-level.

The summertime inverse (Fig. 14c) and salt-plug (Fig. 14d) estuaries are respectively characterized by a landward increase in salinity (from ~38.5 psu at the mouth to 40.5 psu at the head), and a salinity maximum zone (~42 psu) at the mid-estuary. These two estuaries show lower impacts from the sea-level rise (Fig. 14g, h) in comparison to the others (FLE system and positive estuary) in wet months (Fig. 14e, f). The estuarine salinity decreases by 0.25 psu due to the sea-level rise in the summertime estuaries (Fig. 14g, h), especially in the up-estuary of the inverse system (Fig. 14g). Rising sea-level tends to decrease salinity within inverse and salt-plug estuaries, in contrast to the salinity-increasing impact inside the FLE and Positive systems. The salinity decrease (dilution) caused by the sea-level rise occurs in the inverse and salt-plug estuaries, as their estuarine waters are typically saltier than ocean waters.

5. Conclusion

This study shows that the along-channel salinity variation in the Mond Estuary indicates a positive estuarine system in wet months, which transforms into inverse and salt-plug estuaries during warm months. Also, the positive system of this estuary is influenced by occasional heavy rains induced hypersaline runoffs resulting in the confinement of a low-salinity water mass (lens) by both marine and riverine saltwater sources. This highly unsteady state is denoted freshwater lens estuary (FLE), which has a longitudinal salinity gradient opposite to that in a salt-plug estuary. Therefore, the Mond Estuary exhibits different time-dependent salinity fields, with a considerable range of time scales from hour-day (in the FLE condition) to month-season (in the positive, inverse and salt-plug estuaries). During the strong FLE conditions induced by the hypersaline discharge, the advective salt flux dominates the other flux terms resulting in a seaward net salt transport throughout the estuary. In this unsteady state, the seaward salt transport by advection at the estuary head is ~6 times higher than the corresponding value during the weak FLE state (immediately before a hypersaline runoff). Under weak FLE conditions, the phase difference between the tidal velocity and elevation is close to 90°, indicating the presence of standing waves in the estuary. Also, under such conditions, the salt flux Q3 (dependent on the cross-correlation between sea-level and salinity) is in phase with the depth- and time-averaged velocity in the positive estuarine segment (near the mouth). In contrast, this flux is out of phase with the mean velocity near

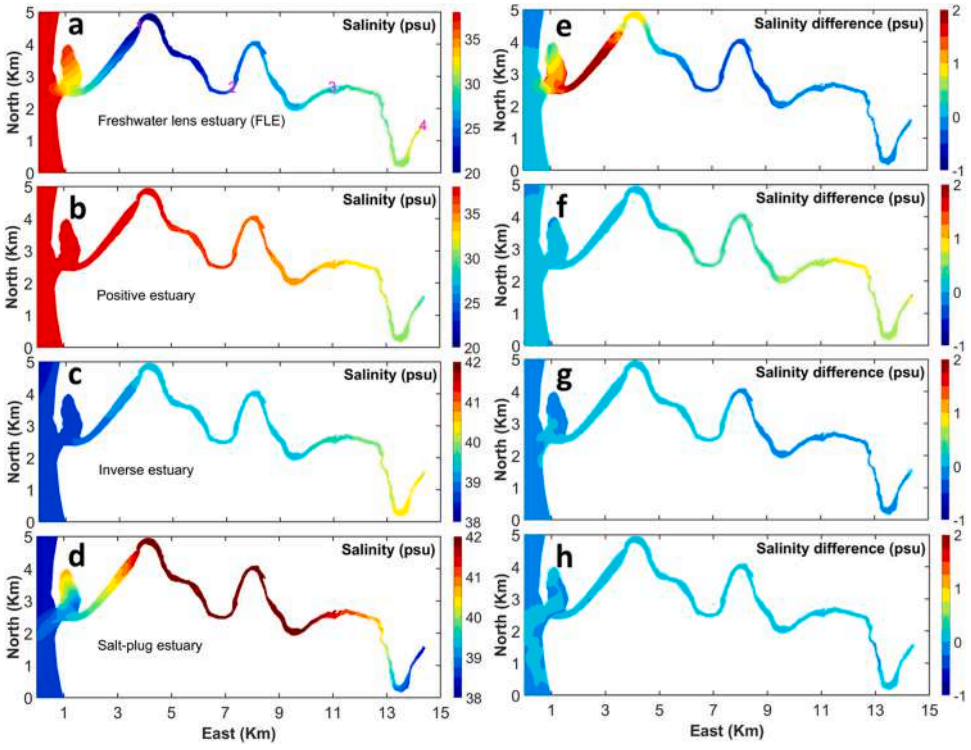

Fig. 14. Depth- and time-averaged salinities during 25 hours in different time-dependent estuarine states of (a) FLE condition on 19–20 January, (b) positive estuary on 10–11 March, (c) inverse estuary on 10–11 July and (d) salt-plug estuary on 10–11 September 2014 at the Mond River Estuary. (**e-f**) The salinities same as (a-d) including 20 cm sea level rise at the marine open boundary, which are subtracted from the corresponding FLE, positive, inverse and salt-plug estuarine systems. The numbers 1 – 4 in (a) stand for observational stations 1 – 4.

the head where salinity increases in the landward direction owing to the hypersaline runoff (the quasi-inverse estuarine segment). The analysis of Péclet number *Pe* indicates that the advective transport is more significant than the diffusive (mixing) transport ($Pe > 1$) at all stations except St2 during the weak FLE condition, where diffusive dispersion is significant ($Pe < 1$). Furthermore, results from numerical simulations show that a hypersaline runoff with a discharge of at least 400 m^3/s is required to dampen the tidal level at the head. In the idealized funnel-shaped estuarine experiment, the longitudinal flows include two positive subtidal estuarine circulation cells, separated by a mixing maximum zone where the potential energy anomaly is lower than 0.75 J/m^3. Rising sea-level tends to decrease salinity within inverse and salt-plug estuaries, in contrast to the salinity increasing impact inside the FLE and Positive systems. However, the impact of sea-level rise is lower in summertime inverse and salt-plug estuaries compared to wintertime estuaries (FLE and positive systems) in the Mond Estuary.

Funding

This study contributes to theme "C3: Sustainable Adaption Scenarios for Coastal Systems" of the Cluster of Excellence EXC 2037 'CLICCS - Climate, Climatic Change, and Society' – Project Number: 390683824 funded by the Deutsche Forschungsgemeinschaft (DFG, German Research Foundation) under Germany's Excellence Strategy.

CRediT authorship contribution statement

Seyed Mostafa Siadatmousavi: Writing – review & editing, Investigation, Conceptualization. **Emil Stanev:** Writing – review & editing, Supervision, Investigation. **Seyed Taleb Hosseini:** Writing – review & editing, Writing – original draft, Software, Methodology, Investigation, Formal analysis, Conceptualization. **Johannes Pein:** Writing – review & editing, Software, Methodology. **Corinna Schrum:** Funding acquisition, Supervision, Writing – review & editing.

Declaration of Competing Interest

The authors declare that they have no known competing financial interests or personal relationships that could have appeared to influence the work reported in this paper.

Data availability

The authors do not have permission to share data.

Acknowledgements

This study used data from the DHI (Cheng and Andersen, 2010), CMEMS (https://doi.org/10.48670/moi-00021) and ECMWF (DOI: 10.24381/cds.adbb2d47).

References

Ali, A., Lemckert, C.J., Dunn, R.J., 2010. Salt fluxes within a very shallow subtropical estuary. J. Coast. Res. 26, 436–443.
Aristizábal, M.F., Chant, R.J., 2015. An observational study of salt fluxes in Delaware Bay. J. Geophys. Res.: Oceans 120, 2751–2768.
Bagnell, A., DeVries, T., 2023. Global mean sea level rise inferred from ocean salinity and temperature changes. J. Geophys. Res. Lett. 50, e2022GL101004.
Banas, N., Hickey, B., MacCready, P., Newton, J., 2004. Dynamics of Willapa Bay, Washington: A highly unsteady, partially mixed estuary. J. Phys. Oceanogr. 34, 2413–2427.
Baubekova, A., Akbari, M., Etemadi, H., Ashraf, F.B., Hekmatzadeh, A.T., 2023. Causes & effects of upstream-downstream flow regime alteration over Catchment-Estuary-Coastal systems. J. Sci. Total Environ. 858, 160045.
Bhuiyan, M.J.A.N., Dutta, D.J.E., Coastal, Science, S., 2012. Assessing impacts of sea level rise on river salinity in the Gorai river network, Bangladesh. 96, 219-227.
Biemond, B., de Swart, H.E., Dijkstra, H.A., Díez-Minguito, M., 2022. Estuarine salinity response to freshwater pulses. J. Geophys. Res.: Oceans 127, 1–18.
Bowden, K.F., 1963. The mixing processes in a tidal estuary. Int. J. Air Water Pollut. 7, 343–356.
Bowden, K.F., 1967. Stability effects on turbulent mixing in tidal currents. J. Phys. Fluids 10, S278–S280.
Chanson, H., 2008. Field observations in a small subtropical estuary during and after a rainstorm event. Estuar. Coast. Shelf Sci. 80 (1), 114–120.
Cheng, Y., Andersen, O.B., 2010. Improvement in global ocean tide model in shallow water regions. Poster, SV 45, 1–68.
Dionne, J.J.Zf.G., 1963. Towards a more adequate definition of the St. Lawrence Estuary 7, 36–44.
Dyer, K.J.N.Y., 1997. Estuaries: a physical introductionWiley. 1..
Etemadi, H., Smoak, J.M., Abbasi, E.J.O., 2021. Spatiotemporal pattern of degradation in arid mangrove forests of the Northern Persian Gulf. 63, 99-114.
Friedrichs, C.T., 2010. Barotropic tides in channelized estuaries. Contemp. Issues Estuar. Phys. 27–61.
Funahashi, T., Kasai, A., Ueno, M., Yamashita, Y., 2013. Effects of short time variation in the river discharge on the salt wedge intrusion in the Yura estuary, a micro tidal estuary, Japan.
Ghaemi, M., Gholamipour, S.J.Jo.O., 2017. Seasonal measurement of nutrient concentrations and total alkalinity in the Mond Estuary ecosystem. 8, 11-18.
Hosseini, S.T., Chegini, V., Sadrinasab, M., Siadatmousavi, S.M., Yari, S., 2016. Tidal asymmetry in a tidal creek with mixed mainly semidiurnal tide, bushehr Port, Persian Gulf. Ocean Sci. J. 51, 195–208.
Hosseini, S.T., Siadatmousavi, S.M.J.E., 2018. Coastal, Science, S., 2018. Field observations of hypersaline runoff through a shallow estuary. 202, 54-68.
Hosseini, S.T., Stanev, E., Pein, J., Levinson, A., Schrum, C., 2023. Longitudinal and lateral circulation and tidal impacts in salt-plug estuaries. J. Front. Mar. Sci. 10, 1152625.
Hunkins, K., 1981. Salt dispersion in the Hudson Estuary. J. Phys. Oceanogr. 11, 729–738.
Janardanan, V., Amaravayal, S., Revichandran, C., Manoj, N., Muraleedharan, K., Jacob, B., 2015. Salinity response to seasonal runoff in a complex estuarine system (Cochin estuary, west coast of India). J. Coast. Res. 31, 869–878.
Kjerfve, B., Knoppers, B.A.J.Th, 1991. Tidal choking in a coastal lagoon. 1, 169..
Largier, J., 2010. Low-inflow estuaries: hypersaline, inverse, and thermal scenarios. Contemp. Issues Estuar. Phys. 247–272.
Masson-Delmotte, V., Zhai, P., Pirani, A., Connors, S.L., Péan, C., Berger, S., Caud, N., Chen, Y., Goldfarb, L., Gomis, M.J.CowgIttsarotipocc, 2021. Climate change 2021: the physical science basis. 2.
Normand, J.C., Heggy, E., Castellazzi, P., 2023. Nationwide Subsidence in Bahrain Island: Drivers and Implications for Relative Sea Level Rise. IEEE J. Sel. Top. Appl. Earth Obs. Remote Sens.
Pritchard, D.W., 1954. A Study salt Balance A Coast. plain Estuary.
Restrepo, J.D., Kjerfve, B., 2002. The San Juan Delta, Colombia: tides, circulations, and salt dispersion. J. Cont. Shelf Res. 22, 1249–1267.
Savenije, H.H., 2005. in alluvial estuaries. Gulf Professional Publishing. Salin. tides.
Simpson, J., 1981. The shelf-sea fronts: implications of their existence and behaviour. J. Philos. Trans. R. Soc. Lond., Math. Phys. Sci. 302, 531–546.
Talbot, C., Jarvis, R., 1984. Age, budget and dynamics of an active salt extrusion in Iran. J. Struct. Geol. 6, 521–533.
Talbot, C.J., Rogers, E.A.J.S., 1980. Seasonal movements in a salt glacier in Iran. 208, 395-397.
Talbot, C.J.G.S., London, Special Publications, 1981. Sliding and other deformation mechanisms in a glacier of salt, S Iran. 9, 173-183.
Valle-Levinson, A., 2010. Contemporary issues in estuarine physics. Cambridge University Press.
Valle-Levinson, A., 2022. Introduction to Estuarine Hydrodynamics. Cambridge University Press.
Valle-Levinson, A., Li, M., 2023. Climate change and saltwater intrusion in estuaries. Climate Change and Estuaries. CRC Press, pp. 99–112.
Valle-Levinson, A.J.Toe, science, c, 2011. 1.05 Classification of estuarine circulation. 75-86.
Vijith, V., Shetye, S., Baetens, K., Luyten, P., Michael, G.J.E., Coastal, Science, S., 2016. Residual estuarine circulation in the Mandovi, a monsoonal estuary: A three-dimensional model study. 173, 79-92.
Vijith, V., Sundar, D., Shetye, S.J.E., Coastal, Science, S., 2009. Time-dependence of salinity in monsoonal estuaries. 85, 601-608.
Zhang, Y.J., Ye, F., Stanev, E.V., Grashorn, S.J.O.M., 2016. Seamless cross-scale modeling with SCHISM. 102, 64-81.

4 Study III: Hydrodynamics of the Persian Gulf, as an inverse estuary

This chapter contains the third paper, which is submitted to Journal of "Ocean Dynamics":

Hosseini, S.T., Stanev, E., Pein, J., Schrum, C. and Benjamin Jacob (2024). ***Tidal Impacts on Volume Transports through the Strait of Hormuz and on Persian Gulf Salinity***.

Author contributions:

STH and BJ developed the model set-up. STH implemented different numerical experiments, performed the data analysis and wrote the manuscript. All authors contributed to the conception and design of the study. ES, JP and CS contributed to the analysis of results and discussion. STH and ES revised and approved the manuscript.

Tidal Impacts on Volume and Salt Transport through the Strait of Hormuz and on Persian Gulf Salinity

Seyed Taleb Hosseini,[a] Emil Stanev,[a] Johannes Pein,[a] Corinna Schrum,[a,b] Benjamin Jacob[a]

[a] *Institute of Coastal Systems - Analysis and Modeling, Helmholtz-Zentrum Hereon, Geesthacht, Germany*

[b] *Institute of Oceanography, Center for Earth System Research and Sustainability, Universität Hamburg, Hamburg, Germany*

Corresponding author: Seyed Taleb Hosseini, seyed.hosseini@hereon.de

Abstract

This modeling study investigates tidal impacts on volume and salt transport at the Strait of Hormuz (SOH) and salinity distribution in the Persian Gulf (PG). Exchange flows through the SOH are quantified resolving high and low frequencies, and salinity classes. In the PG, tidal forcing dominates over density gradients (tidal Froude number $T_f > 1$). Tides increase the annual inflow-outflow rates at the SOH to ~±0.54 Sv compared to non-tidal experiments. Tidal mixing weakens residual flows in the SOH. The salt flux by shear dispersion is always seaward in the PG, as in other inverse estuaries. The small tidal pumping salt flux also becomes seaward, as the covariance between tidal velocity and salinity is negative over annual time-scales. Conversely, the advective salt flux is landward, similar to the landward net volume transport. Therefore, the net salt flux is seaward (landward) if the seaward salt transports (shear dispersion and tidal oscillation) are stronger (weaker) than the landward advective component. Without wind, the landward advection mainly overcomes the two seaward fluxes and drives a landward net salt flux in the PG. This leads to an increase in the PG-salinity. The landward tidal advection decreases towards the PG-head coinciding with a decrease in mean tidal height. High salinities and $T_f > 10$ coincide with the formation of tidal standing waves in the northwestern and southern coasts.

Keywords: tidal mixing, tidal Froude number, net salt flux, Knudsen relationship, total exchange flow, inverse estuary

1. Introduction

The Persian Gulf (PG) is a shallow, semi-enclosed marginal sea located in the arid region of the southwesterly Asian Continent at 23°N to 31°N and 47°E to 56°E. It connects to the Oman Sea and the Indian Ocean through the Strait of Hormuz (SOH) (Fig. 1). The PG is separated from the Red Sea by the Arabian Peninsula, and both marginal seas inject dense waters into the Indian Ocean. Their water masses are characterized by the highest salinity of the world's oceans (Beal et al., 2000; Reynolds, 1993). Additionally, the PG is accounted for as the warmest estuarine water mass during the summer in the world (Alosairi et al., 2020).

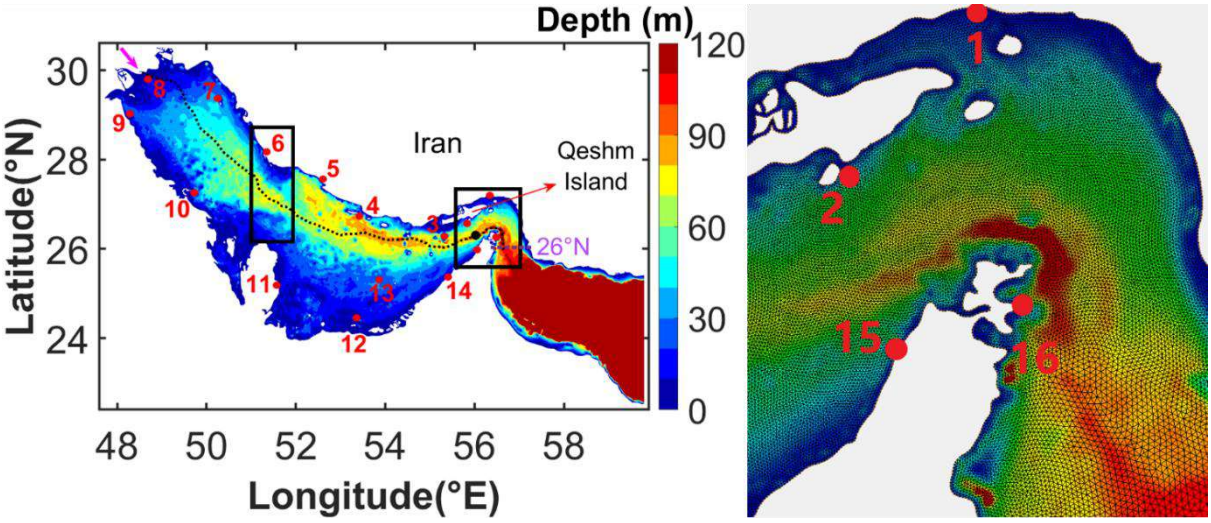

Fig. 1- Bathymetry of the Persian Gulf (PG) and the Strait of Hormuz (SOH). The locations of the river input and observations from Johns et al. (2003)'s study are marked by one arrow at the northwesterly coast and black circle at the SOH, respectively. The black dotted line along the main axis of PG identifies the PG-thalweg. The cross-section at the SOH (latitude 26 °N) is detected by a dashed line. The two black boxes show the location where temperature-salinity diagrams have been analyzed for comparison with earlier observations and studies. The sixteen red circles 1-16 mark the locations of tidal stations. The black box at the SOH including grid cells and four of the sixteen tidal stations is shown on the right side.

The PG is characterized by high evaporation rates that significantly exceed the rates of precipitation and river runoff. As a result, the PG behaves as an inverse (Johns et al., 2003; Kämpf and Sadrinasab, 2006; Lorenz et al., 2020) with its net volume transport almost always exhibiting net-inflow rates. These net-inflows are associated with more significant low-density inflows from the Indian Ocean Surface Water (IOSW) than the near-bottom dense Persian Gulf Water (PGW) outflows. Density gradients and Coriolis force shape the PG-general circulation, forming a basin-scale cyclonic gyre.

Besides the density gradients, winds and tides act as additional forcing factors. In the north of the PG, Iran's Zagros Mountains channel the winds to the southeast (Reynolds, 1993). Consequently, the PG experiences northwesterly winds throughout the year. The summer winds are mild and continuous, while the winter winds are sudden and violent, associated with synoptic weather systems (Perrone, 1979; Reynolds, 1993). Tides in the PG are complex, with the predominant pattern changing from semi-diurnal to diurnal tidal regimes. The semi-diurnal tides have two amphidromic points, while the diurnal tides have only one (Reynolds, 1993).

The observation-based study by Azizpour et al. (2016) found that tides have a significant impact on the flow throughout the water column at the SOH, where partially progressive tidal waves propagate. In the study of the same authors, the highest axial tidal flows of about 1 m/s were measured at the SOH, particularly on the western side of the strait (inside the PG close to the SOH). Furthermore, they observed flood-dominated asymmetry on the eastern side of the SOH (outside the PG). In contrast, the measuring mooring located on the western side of the SOH (inside the PG) indicated an ebb-dominated asymmetry. Another observational study by Khosravi et al. (2018) demonstrated that the maximum axial tidal velocities peak at 1.8 m/s during spring tides at the SOH between Qeshm Island and Iranian coasts (for the positions of geographic locations, see Fig. 1). The same authors also revealed that large lateral shears can be generated by tides and are associated with local bathymetric changes where the across-channel momentum balance is strongly ageostrophic. Also, using a barotropic model, Mashayekh Poul et al. (2016) found that tide-induced residual flows are strong at the SOH and along the coastal areas of the PG. Therefore, the strong tidal flows in the SOH can efficiently mix the PGW with the IOSW masses (Pous et al., 2012), potentially affecting volume and salt transports between the PG and the Indian Ocean.

Temporal variations in density gradient and wind associated with tides and local bathymetry inside the SOH might affect inflow and outflow rates. According to various literature reviews, such as Chao et al. (1992), Kämpf and Sadrinasab (2006), Yao and Johns (2010b), and Campos et al. (2020), the density gradient between the PG and the Indian Ocean controls volume transports through the SOH. To estimate the volume transports, earlier observational and numerical studies (Table 1) mainly considered residual (time-averaged) or non-tidal variabilities in the Eulerian framework. The distinct method of total exchange flow (TEF) was employed by Lorenz et al. (2020).

A precise analysis of tidal effects on inflowing-outflowing volume and salt transports through the SOH is still missing, prompting us to implement this modeling study. The present study benefits from high horizontal and vertical resolutions to calculate volume and salt exchanges through the SOH using (1) Eulerian, (2) TEF, and (3) absolute methods (see Section 2b). The latter approach (the absolute method) can calculate the instantaneous exchanges before temporal averaging, which clarifies tidal impact on the inflowing-outflowing volume and salt transports. The results of this study not only provide a comprehensive understanding of volume and salinity exchanges but also quantify tidal impacts on volume and salt transports, particularly through the utilization of the absolute method.

Table 1- Annually averaged volume transports (Sv) through the Strait of Hormuz estimated in previous observational and model-based studies. NA means not applicable.

Previous studies	Observation-based study	Model-based study	Incoming volume transport	Outgoing volume transport	Net volume transport
Ahmad and Sultan (1991)	×		0.186	-0.169	0.017
Ackleson et al. (1992)	×		0.107	-0.099	0.008
Johns et al. (2003)	×		0.23±0.04	Lower layers: -0.15 ± 0.03 Upper layers: -0.06 ± 0.02	0.02
Sadrinasab and Kämpf (2004)		×	0.177	-0.163	0.014
Yao and Johns (2010b)		×	NA	-0.12	NA
Hassanzadeh et al. (2012)		×	0.2	-0.17	0.03
Pous et al. (2015)		×	0.193	-0.185	0.008
Vasou et al. (2020)		×	0.22 ± 0.01	-0.147 ± 0.01	0.073
Campos et al. (2020)		×	0.272	-0.26±0.05	0.0122
Lorenz et al. (2020)		×	0.155	-0.138	0.02
Al-Shehhi et al. (2021)		×	NA	-0.14	NA

During the warmer months, the IOSW intrudes to a longer length into the PG and penetrates along the northern Iranian coasts to the head of the PG (Kämpf and Sadrinasab, 2006). This is caused by the increased density difference between the PG and the Oman Sea and the strong stratification (weak mixing condition) resulting from summer heating (Thoppil and Hogan, 2010). Consequently, the northern Iranian side close to the PG-head experiences a lower salinity in the warm months. Any variation in salinity distribution of the PG can be linked to changes in inflow-outflow through the SOH. For instance, interannual fluctuations in salinity over the PG affect the density difference between the PG and the Indian Ocean, resulting in similar interannual oscillations in water exchanges through the SOH (Pous et al., 2015).

The literature reviews considered the PG-circulation influenced by tides e.g. (Pous et al., 2012) and winds as in the studies by (Pous et al., 2013; Thoppil and Hogan, 2010). In particular, Pous et al. (2012) noted that tide-induced residual currents have a weak influence (about 0.02 m/s) on the overall circulation.

To the best of our knowledge, salinity transport within the PG through different mechanisms, particularly affected by tidal forcing, has rarely been investigated by earlier observational and numerical studies. The present study aims to fill this gap.

The paper is structured as follows: Section 2 presents the model description and different setups, addresses various methods for calculating inflowing and outflowing volume and salt transports, along with decompositions of their net fluxes, and the definition of tidal Froude number. Section 3 evaluates model results against observations (temperature, salinity, velocity and tidal elevations), remote sensing SST data, and heat and freshwater fluxes from earlier studies. Subsequently, Section 4 quantifies the volume and salt transports through the SOH with and without tidal forcing using different methods. It also outlines the Knudsen relationship and tidal impacts on salinity distribution and vertical stratification at the PG. In section 5, the influence of tides on salinity transports and its distribution at the PG associated with tidal mixing at the SOH is discussed, using salt flux decomposition and non-dimensional numbers. The paper ends with a conclusion.

2. Methods

a. Numerical model

We employed the Semi-implicit Cross-scale Hydroscience Integrated System Model, SCHISM, (Zhang et al., 2016). This model uses a highly efficient semi-implicit finite-element and finite-volume method with an Eulerian-Lagrangian algorithm to solve the Reynolds averaged Navier–Stokes equations under the hydrostatic approximation.

The model domain encompasses the entire PG, SOH, and the Oman Sea, with the open ocean boundary set at 59.796° E (Fig. 1). The bathymetry utilized in the model is derived from ETOPO1 data. The horizontal grid comprises 244612 surface triangular and quadrangular cells, with a horizontal resolution ranging from 0.1° (~10 km) in the deep open ocean to 0.01° (~1 km) in the SOH and shallow areas in the PG. Vertically, the flexible sigma coordinate of LSC^2 (Localized Sigma Coordinates with Shaved Cell) is used, with the number of layers varying from 47 along the deep open boundary (deeper than 3300 m) to 24 at SOH (~100 m depth) and decreasing to 21 layers for depths shallower than 50 m. The vertical system LSC^2 resolves steep slopes and skew elements.

All numerical simulations are conducted for a period of nine years (1993-2001). The atmospheric forcing is based on hourly meteorological data with a 0.25° horizontal resolution obtained from the European Centre for Medium-Range Weather Forecasts (ECMWF, https://cds.climate.copernicus.eu). Sea surface height, velocity, temperature and salinity at the open boundary were taken from the daily reanalysis data (1/12° horizontal resolution, 50 vertical levels) of the PG provided by the Copernicus Marine Environment Monitoring Service (CMEMS, https://resources.marine.copernicus.eu) for the period of 1993-2001.

Three numerical experiments were performed: one control run (CRM) with all forcings turned on, and two experiments in which either the wind (non-wind model, NWM) or the barotropic tidal forcing (non-tidal model, NTM) was turned off.

The tidal forcing utilizes ten tidal constituents (Q1, O1, P1, S1, K1, N2, M2, S2, K2 and M4) along the open boundary from FES (Finite Element Solution)- Global tidal model (Lyard et al., 2017) on a 1/16°x1/16° grid resolution.

The primary river discharge into the PG is from the Shatt-Al-Arab located at the PG head and comprises the Euphrates, Tigris, and Karun rivers. The river discharge is forced in the model (shown with the pink arrow on the northwesterly coast in Fig. 1), oscillating sinusoidally with minimum and maximum values occurring in October and April, respectively (Kämpf and Sadrinasab, 2006). Literature reviews reported different values for the river inflow of Shatt-Al-Arab, ranging widely from a peak of ~1400 m^3/s (for example, in the studies of Pous et al., 2015) to 650 m^3/s in the studies of Kämpf and Sadrinasab (2006); (Vasou et al., 2020) which can fall as low as 80 m^3/s (Alosairi and Pokavanich, 2017). All of these values of river discharges locally (or regionally in seldom extreme events) influence the PG hydrodynamics (Alosairi et al., 2019). Since 50 - 60 years ago, the historical annual mean discharge has experienced a decreasing trend from 1456 m^3/s to 40 m^3/s (Alosairi et al., 2019; Alosairi and Pokavanich, 2017) primarily due to anthropogenic pressure of dam constructions in the estuary upstream. This study considered three sinusoidal daily discharge conditions with annual means of 1060 m^3/s (with a maximum of 1456 m^3/s and a minimum of 837 m^3/s), 470 m^3/s (with a maximum of 650 m^3/s and a minimum of 350 m^3/s), and 60 m^3/s (with a maximum of 80 m^3/s and a minimum of 46 m^3/s) in the three periods of 1993-1999, 2000-2009 and 2010-2022, respectively. The maximum daily values occurred in April and the minimum ones in October following (Kämpf and Sadrinasab, 2006).

We also used the CMEMS data as the initial condition and finally analyzed the hourly results of CRM, NWM and NTM in the last 5-year runs (1997 – 2001).

b. Calculations of volume and salt fluxes

This study investigates the potential variations in inflowing and outflowing transports at the SOH that may result from changing the calculation method from the Eulerian and TEF approaches (which have been found to

be less than 0.27 Sv in previous studies) to the absolute case influenced by tides. Modifying the water exchange between the PG and the Oman Sea would certainly enhance the relevant exchange of salt.

This section presents three methods for estimating volume and salt transport in an estuarine system: Eulerian, absolute, and TEF. SCHISM can compute volume and salinity fluxes using the absolute method. The model results are then used to apply the three methods to compute the fluxes at the SOH.

The volume influx (Q_{in}), volume outflux (Q_{out}), salt influx (Q^{s}_{in}), and salt outflux (Q^{s}_{out}), are defined based on the traditional Eulerian framework (Kuo et al., 1992; Xiong et al., 2021a) as equation (1):

$$Q_{in}^{Eul} = \iint_A \langle U^+ dA \rangle \, , \, Q_{out}^{Eul} = \iint_A \langle U^- dA \rangle$$

$$Q_{in}^{s,Eul} = \iint_A \langle U^+ S dA \rangle \, , \, Q_{out}^{s,Eul} = \iint_A \langle U^- S dA \rangle \quad (1)$$

where $U(y,z,t)$, $S(y,z,t)$, and $dA(dy, \mathrm{d}z, t)$ are respectively the normal velocity, salinity and area of gridded cells on each cross-section with area A. The time-varying area integration A ($\iint_A dA$) extends vertically from the bottom to the surface (z), and laterally from 0 to the cross-sectional width (y). U^+ and U^- indicate inflow to the PG (with positive values) and outflow from the PG (with negative quantities), respectively. The brackets $\langle \ \rangle$ indicate the tidally (time-) averaged value.

The absolute method integrates (sums) all inflowing and outflowing fluxes before temporal averaging $\langle \ \rangle$ (Lorenz et al., 2019):

$$Q_{in}^{Abs} = \langle \iint_A U^+ dA \rangle \, , \, Q_{out}^{Abs} = \langle \iint_A U^- dA \rangle$$

$$Q_{in}^{s,Abs} = \langle \iint_A U^+ S dA \rangle \, , \, Q_{out}^{s,Abs} = \langle \iint_A U^- S dA \rangle \quad (2)$$

In fact, the Eulerian method (equation 1) uses residual (time-averaged) flows, while the absolute analysis (equation 2) utilizes the tidal (instantaneous) velocities to calculate the fluxes.

In the TEF approach (MacCready, 2011), the instantaneous volume flux $Q(s)$ and salt flux $Q^s(s)$ through a cross-section are classified as a function of salinity class s:

$$Q(s) = \iint_{A(s)} U dA \, , \, Q^s(s) = \iint_{A(s)} U S dA \quad (3)$$

where $A(s)$ is the instantaneous area of a cross-section with salinity greater than s.

The volume and salinity fluxes in a specific salinity class (isohaline volume and salt transports) can be obtained through differentiating related functions $Q(s)$ and $Q^s(s)$ with respect to salinity:

$$-\frac{\partial Q}{\partial s} = -\lim_{\delta s \to 0} \frac{Q(s+0.5\delta s) - Q(s-0.5\delta s)}{\delta s} \ , \ -\frac{\partial Q^s}{\partial s} = -\lim_{\delta s \to 0} \frac{Q^s(s+0.5\delta s) - Q^s(s-0.5\delta s)}{\delta s} \quad (4)$$

in which the minus sign indicates that positive values of $-\frac{\partial Q}{\partial s}$ and $-\frac{\partial Q^s}{\partial s}$ correspond to inflowing transports for a given salinity class. Following Wang et al. (2017), the TEF volume influx (Q_{in}^{TEF}) and volume outflux (Q_{out}^{TEF}), and similarly the corresponding salt fluxes ($Q_{in}^{s,TEF}, Q_{out}^{s,TEF}$) can be calculated as:

$$Q_{in}^{TEF} = \int \langle -\frac{\partial Q}{\partial s} \rangle |_{in} \ ds \, , \, Q_{out}^{TEF} = \int \langle -\frac{\partial Q}{\partial s} \rangle |_{out} \ ds$$

$$Q_{in}^{s,TEF} = \int \langle -\frac{\partial Q^s}{\partial s} \rangle |_{in} \ ds \, , \, Q_{out}^{s,TEF} = \int \langle -\frac{\partial Q^s}{\partial s} \rangle |_{out} \ ds \quad (5)$$

To reduce the sensitivity of the inflowing (Q_{in}^{TEF}, $Q_{in}^{s,TEF}$) and outflowing (Q_{out}^{TEF}, $Q_{out}^{s,TEF}$) transports to the number of salinity bins in the inverse estuary of the PG, the salinity at which $Q(s)$ (or $Q^s(s)$) is minimum (the largest negative value) is first determined. Then the inflowing and outflowing exchanges (equation 5) are presented with the integrals of the transports in the salinity bins below and above the minimum salinity, respectively. In the salinity range from 34 psu to 42 psu, TEF values are insensitive to the number of salinity bins over a range from 100 ($\delta s = 0.08$ psu) to 1600 ($\delta s = 0.005$ psu) in the SOH. Therefore, 100 bins are considered to calculate $Q(s)$ and $Q^s(s)$ using hourly model outputs over the five years (1997 – 2001).

In this study, we consider the classical Eulerian framework (equation 1) without binning into salinity classes which may differ from the Eulerian version of TEF based on isohaline coordinates used in previous studies e.g. (Burchard et al., 2018; MacCready, 2011; Xiong et al., 2021b).

The flux-weighted salinities through a cross-section from the three methods (Eulerian, absolute and TEF), are defined as the fractions between their salinity fluxes $Q_{in}^{s,method}$ and $Q_{out}^{s,method}$, and the corresponding volume fluxes Q_{in}^{method} and Q_{out}^{method}, respectively:

$$S_{in}^{method} = \frac{Q_{in}^{s,method}}{Q_{in}^{method}}$$

$$S_{out}^{method} = \frac{Q_{out}^{s,method}}{Q_{out}^{method}} \quad (6)$$

in which "$method$" indicates the three methods of Eulerian (equation 1), absolute (equation 2) and TEF (equation 5) approaches.

Also the net volume (Q_{net}^{method}) and salt ($Q_{net}^{s,method}$) fluxes in each of the three methods can be obtained as:

$$Q_{net}^{method} = Q_{in}^{method} + Q_{out}^{method}$$

$$Q_{net}^{s,method} = Q_{in}^{s,method} + Q_{out}^{s,method} \quad (7)$$

c. Decompositions of net salt and volume fluxes

The tidally averaged (net) salt flux (in the absolute approach) can be decomposed into three main components: advective, sheared, and tidal salt fluxes (Lerczak et al., 2006) at any cross-section. To implement the salt flux decomposition, the normal velocity $U(y,z,t)$ and salinity $S(y,z,t)$ over each section should first be decomposed into three orthogonal components: tidally and cross-sectionally averaged u_a and s_a, tidally averaged and cross-sectionally varying $u_{sh}(y,z)$ and $s_{sh}(y,z)$, and tidally and cross-sectionally varying $u_t(y,z,t)$ and $s_t(y,z,t)$ (Lerczak et al., 2006). The three components of the velocity decomposition (the decomposition of salinity is also the same) are presented in equation (8).

$$u_a = \frac{\langle \iint_A U(y,z,t)dA \rangle}{\langle \iint_A dA \rangle}$$

$$u_{sh}(y,z) = \frac{\langle U(y,z,t)dA \rangle}{\langle dA \rangle} - u_a$$

$$u_t(y,z,t) = U(y,z,t) - u_{sh}(y,z) - u_a \quad (8)$$

The tidally averaged total salt flux or the net salt flux $\langle Q_{net}^s \rangle$ can then be decomposed into its three components: Q_a^s (advection), Q_{sh}^s (shear dispersion), and Q_t^s (tidal oscillation), using equations (9) and (10):

$$\langle Q_{net}^{s} \rangle = \langle \iint_A U(y,z,t)S(y,z,t)dA \rangle = Q_a^s + Q_{sh}^s + Q_t^s$$

$$Q_a^s = u_a s_a \iint_A \langle dA \rangle$$

$$Q_{sh}^s = \iint_A [u_{sh}(y,z)s_{sh}(y,z)] \langle dA \rangle$$

$$Q_t^s = \iint_A \langle u_t(y,z,t)s_t(y,z,t)dA \rangle$$

(9) (10)

The advective salt flux (Q_a^s) is generally related to transports by river discharge and wind forcing (Valle-Levinson, 2022). In the CRM, the advective term is mainly due to residual tidal flows and wind forcing. The NWM was defined to account for advective salt transport driven by tides only. The direction of Q_a^s is determined by cross-sectionally and tidally averaged velocity u_a which is directly related to the net volume transport $\langle \iint U(y,z,t)dA \rangle$ (see u_a in equation 8). Thus, each cross-section's salt transport by advection is related to the corresponding net volume flux. Along-channel density (salinity) gradients drive the sheared salt transport (Q_{sh}^s) (Lerczak et al., 2006), which is typically landward in positive estuaries (Aristizábal and Chant, 2015; Valle-Levinson, 2022). Also, sheared wind-driven or tidal residual flows can be linked to Q_{sh}^s(Valle-Levinson, 2022), which can dominate the net salt flux in partially mixed estuaries (Lerczak et al., 2006). Salt transport by tidal pumping (Q_t^s) depends on the covariance between salinity and velocity on tidal time scales. The covariance and the resulting tidal oscillatory salt flux are zero when salinity and velocity are 90° out of phase (in quadrature), (Aristizábal and Chant, 2015). The 90° phase difference is imposed exclusively by the along-channel advection of the tidal currents. On the other hand, the phase difference becomes out of quadrature under some processes such as mixing and lateral (cross-channel) advection which enhance the tidal pumping salt flux (Aristizábal and Chant, 2015).

The time- and depth-averaged net volume transport per unit width through a water depth H is given in this study by $F(m^2 s^{-1})$. F is decomposed into the two components of the non-tidal (residual) drift (F_{nt}) and the Stokes (tidal pumping) drift associated with the non-zero correlation between tidal fluctuations in water depth and velocity (F_{Stokes}), (Sylaios et al., 1998; Uncles et al., 1986; Uncles et al., 1979):

$$F = F_{nt} + F_{Stokes} = \langle \mathrm{H} \rangle \langle \bar{\mathrm{U}} \rangle + \langle \acute{\mathrm{H}} \rangle \langle \acute{\mathrm{U}} \rangle$$

(11)

where the overbar $\bar{}$ identifies a depth-mean value, and the prime $\acute{}$ denotes the depth-average instantaneous deviations from the tidal mean ($\acute{\mathrm{H}} = H - \langle \mathrm{H} \rangle$ and $\acute{\mathrm{U}} = \bar{\mathrm{U}} - \langle \bar{\mathrm{U}} \rangle$). The effect of barotropic tides on the net volume transport can be interpreted in terms of its Stokes drift.

d. Tidal Froude number diagnosed by the model

The non-dimensional tidal Froude (T_f) number summarizes the relative strength of the density gradient versus the tidal stress (resulting from advective acceleration) in driving residual flows. In this study, T_f is calculated using annual mean depth-averaged advective and baroclinic terms from horizontal momentum balances (in x- and y-directions) in the CRM (equation 12).

$$T_f = \frac{Advection}{Baroclinicity} = \frac{\langle \sqrt{\overline{\left(u\frac{\partial u}{\partial x} + v\frac{\partial u}{\partial y} + w\frac{\partial u}{\partial z}\right)^2 + \left(u\frac{\partial v}{\partial x} + v\frac{\partial v}{\partial y} + w\frac{\partial v}{\partial z}\right)^2}} \rangle}{\langle \sqrt{\overline{\left(\frac{g}{\rho}\int_{-H}^{z}\frac{\partial \rho}{\partial x}dz\right)^2 + \left(\frac{g}{\rho}\int_{-H}^{z}\frac{\partial \rho}{\partial y}dz\right)^2}} \rangle}$$

(12)

where $\boldsymbol{u}$, $\boldsymbol{v}$ and $\boldsymbol{w}$ are the velocity components in the $\boldsymbol{x}$, $\boldsymbol{y}$ and $\boldsymbol{z}$ directions, respectively. $\boldsymbol{g}$ is the gravity acceleration, $\boldsymbol{\rho}$ is density. Both advection and baroclinicity terms are computed directly by the model in each grid cell.

Based on the relative strength of tidal forcing and baroclinicity, Valle-Levinson (2022) classified semi-enclosed basins into three categories: $\boldsymbol{Log(T_f) < -1}$ and $\boldsymbol{Log(T_f) > 1}$ indicate density-driven and tidally-driven (tidal residual) flows, respectively. In the intermediate range $\boldsymbol{-1 < Log(T_f) < 1}$ (tidally & density-driven basin), residual flows are driven by both tidal forcing and density gradient.

3. Model evaluation

a. Temperature, salinity and velocity

An available long-term measurement set in the SOH includes about 1-year ADCP-velocity, temperature and salinity data from Johns et al. (2003) 's study. The observation site is denoted by a black circle in Fig. 1.

The thermohaline structure and spatial-temporal distribution of the velocity components from the CRM are in close agreement with Johns et al. (2003), (Fig. 2). Both temperature profiles demonstrate the presence of a seasonal thermocline during summer and significant cooling throughout the water column during winter (see Fig. 2a, c). The deep PGW mass is denser in winter than in summer because of lower temperature and higher salinity in the winter (see Fig. 2a-d). The vertical overturning of high-saline water is detected from July to November and an upwelling of the halocline is evident in both observations and the model (see Fig. 2b, d). The dense PGW mass in both datasets exhibits a substantial velocity primarily at depths greater than 50 m, where positive values of both zonal and meridional velocities indicate a high northeastward outflow (see velocity observations in Fig. 2e, f and the corresponding model-results in Fig. 2g, h). The modeled dense PGW shows slightly higher v-velocities than those observed (see Fig. 2f, h). On the other hand, the inflowing IOSW appears to be weaker than outflowing PGW, which is supported by the presence of southwestward velocities (negative values of u and v) mostly at depths above 40 m in both observations (Fig. 2e, f) and model (Fig. 2g, h).

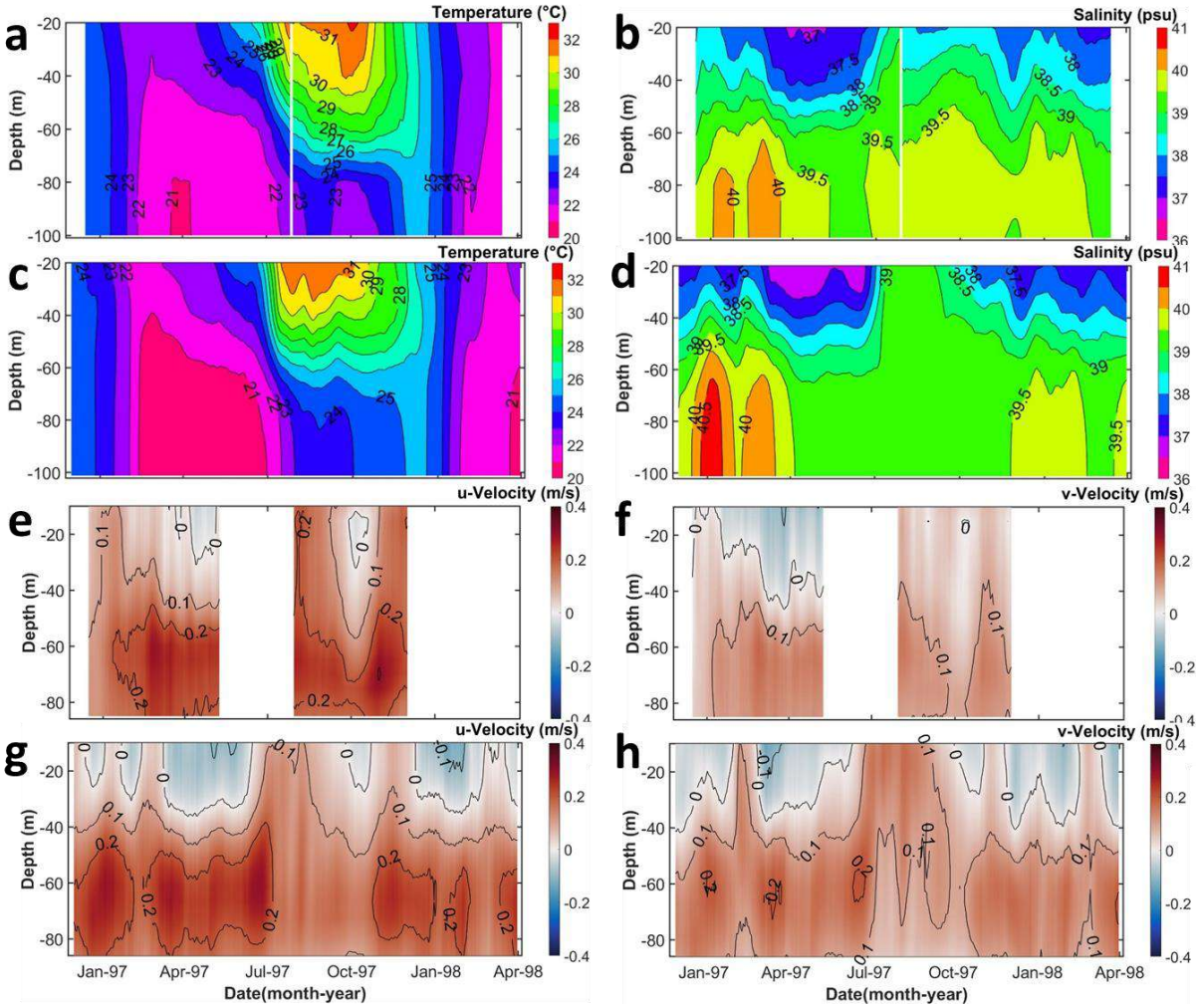

Fig. 2- Hovmöller diagrams of daily temperature (**a**, **c**), salinity (**b**, **d**), u- (**e**, **g**) and v- (**f** , **h**) velocities from observations (**a**, **b**, **e**, **f**) and from the CRM (**c**, **d**, **g**, **h**) at the mooring site of Johns et al. (2003)'s study. A moving average of 28 days is applied in all figures. The model data span the period from December 1996 to March 1998. There are a 2-day gap in observational data of temperature and salinity (a, b) and about 3-month gap in the relevant velocity records (e, f).

The central part of the PG and the SOH (see the two black boxes in Fig. 1) effectively demonstrate the seasonal fluctuations in thermohaline characteristics (Fig.3), which are consistent with earlier observed data (Alessi et al., 1999) and modeling studies by (Kämpf and Sadrinasab, 2006) and (Pous et al., 2015).

In cold months, stratification is notably week at the study area, with vertical temperature exhibiting a near homogenous distribution, which is consistent with the earlier studies of Alessi et al. (1999), (Kämpf and Sadrinasab, 2006) and Pous et al. (2015).

As spring arrives, the upper layers becomes warmer, and consequently, vertical stratification reinforces, especially at the SOH. The density in the SOH increases from 1024 kg/m3 in the surface layer to 1028 kg/m3 at depths of 60 m – 80 m due to the PGW mass (see Fig. 3). The maximum stratification occurs in summer characterized by surface temperatures warmer than 30°C and top-to-bottom temperature gradients higher than 12°C especially at the center part of the PG. In this part, the upper layers are fresher and warmer (originating from IOSW), compared to the saltier and colder dense water masses at lower depths (indicating PGW). During autumn, the surface waters tend to cool down, which coincides with a weakening of stratification (enhancing mixing). As shown in Fig.3, three water masses mix together particularly during winter (1) low-salinity surface water originating from the IOSW, (2) high-salinity surface water formed in coastal areas, especially on the

southern shallow banks around the Qatar Peninsula, and (3) deep PGW. It is worth mentioning that throughout the year, the central part of the PG (upper panels in Fig.3) is consistently saltier than the SOH (lower panels in Fig.3), which suggests an inverse estuarine system in the PG.

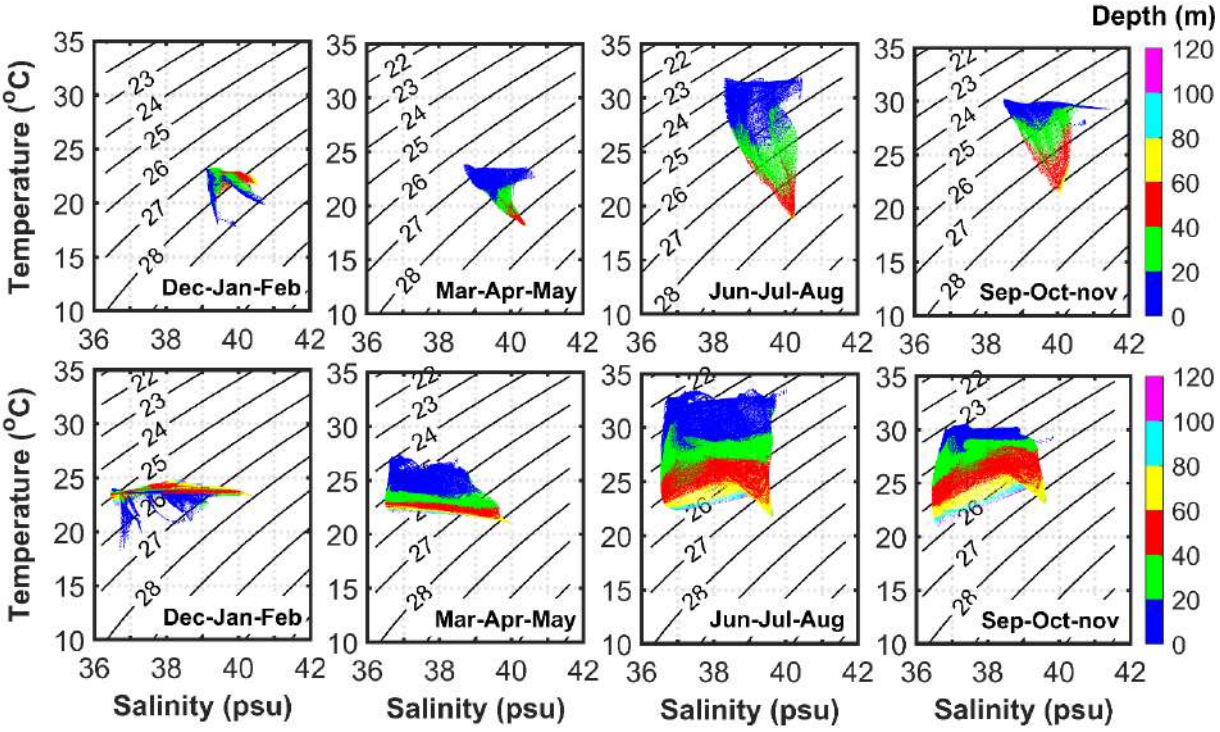

Fig. 3- Seasonal mean temperature-salinity diagram in 1997 – 2001 at the two regions of the PG-center (**top**) and the SOH (**bottom**). Colors indicate different depths with an interval of 20 m. These two regions are detected by two boxes in Fig. 1.

b. Sea surface Temperature

The seasonal (winter and summer) and annual averages of sea surface temperatures in 2001 from the CRM and MODIS satellite data are compared in Fig. 4. The comparison shows good agreement between the model and observations. The statistical parameters of the correlation R, the root-mean-square error (RMSE), and the Bias quantitatively confirm the agreement (see Table 2). The CRM illustrates more accurate SST in winter than in summer and on the annual average (see Fig. 4 and Table 2). In winter, both model and observations show colder coasts at the PG head, temperate SST in the shallow southern banks, and warmer SST towards the SOH (see Fig. 4a, d). During the summer season, the middle part of the PG experiences warm temperatures, particularly on the southern coast, while colder temperatures are observed towards the PG-head and the Oman Sea (Fig. 4b, e). On average, the eastern part of the PG has warmer SST than the western part in both datasets, as shown in Fig. 4c, f. The modeled SSTs in the SOH are slightly warmer (less than 1°C) than the corresponding observations in this area, especially in the annual average.

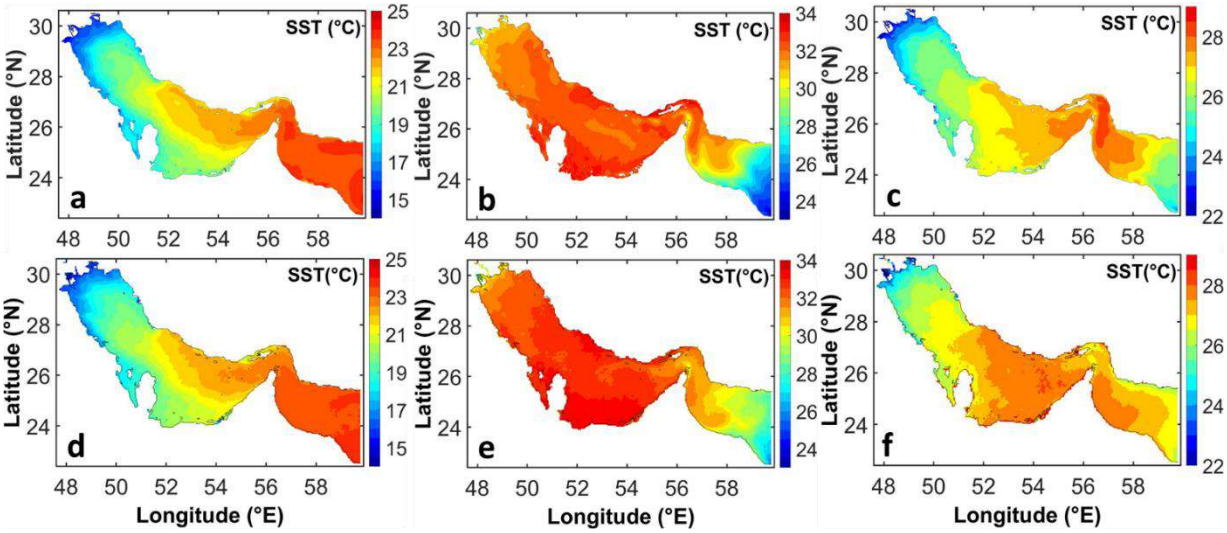

Fig. 4- Comparison of the sea surface temperature (SST) of the CRM (**a, b, c**) with MODIS data (**d, e, f**) in seasonal averages of winter (**a, d**) and summer (**b, e**) and annual mean (**c, f**) in 2001.

Table 2- The correlation R, the root-mean-square error (RMSE), and the Bias in comparison of the seasonal and annual averaged sea surface temperature of the CRM with MODIS in 2001.

	R	**RMSE (°C)**	**Bias (°C)**
winter	0.99	0.21	-0.04
summer	0.91	0.49	-0.14
annual	0.90	0.48	-0.18

c. Tides

To assess the quality of the tides generated by the CRM, we compare the amplitudes and phases of the four main tidal constituents M2, S2, K1 and O1 from this model at 16 stations (see Fig.1) with the corresponding modeled and observed values that reported by Pous et al. (2012) in Table 3.

Overall, the CRM shows good agreement with the two references provided by Pous et al. (2012). The amplitude and phase differences between the CRM and both references are typically within a few centimeters and degrees, respectively, indicating a high level of consistency. Notably, the differences significantly decrease at the SOH, which is the primary area of focus for calculating volume and salt exchanges. For example, at stations 1 (Bandar Abbas) and 16 (Ras Dillah), the differences between the CRM and observations do not exceed 5 cm and 28 degrees.

Table 3- Amplitudes (A) and phase (P) of four main tidal components M2, S2, K1 and O1 from the CRM in 2001 at stations 1-16 detected in Fig. 1 comparing with model results (P-2012) and observations (Obs) reported by Pous et al. (2012). The names of the stations presented in the last row are the same used by Pous et al. (2012).

#	Lat / Lon (° ')	M2 [A (cm) / P (°)]			S2 [A (cm) / P (°)]			K1 [A (cm) / P (°)]			O1 [A (cm) / P (°)]		
		CRM	P-2012	Obs	CRM	P-2012	Obs	CRM	P-2012	Obs	CRM	P-2012	Obs
1	27°11'/56°17'	105/179	95/196	100/197	40/201	33/231	36/229	30/353	34/15	34/11	16/10	20/6	21/3
2	26°41/55°54	71/191	70/221	74/204	27/211	24/261	25/247	21/10	30/46	29/28	13/28	18/22	20/14
3	26°16'/55°18'	55/218	55/239	59/232	20/238	19/283	20/269	17/42	30/65	29/66	15/51	16/33	19/39
4	26°48'/53°23'	28/325	33/350	30/335	10/348	10//34	12/10	19/98	27/91	29/94	13/91	11/58	15/55
5	27°28'/52°37'	35/20	52/28	51/19	12/44	17/83	17/57	16/116	18/117	24/115	10/113	8/90	12/89
6	28°15'/51°16'	42/87	38/63	50/68	14/121	15/120	18/117	13/204	21/207	25/209	11/202	12/171	18/171
7	29°19'/50°20'	34/164	30/169	36/149	12/197	10/223	13/196	22/238	36/230	39/233	17/228	18/190	26/192
8	29°50'/48°43'	72/258	74/217	84/221	23/295	26/279	29/279	30/261	46/244	50/250	23/247	22/203	30/205
9	29°04/48°10	48/284	64/237	63/248	15/321	22/299	17/312	28/271	44/252	43/263	21/256	21/211	29/215
10	27°13'/49°43'	42/72	43/33	44/37	14/107	17/98	16/107	7/297	18/262	17/273	8/277	10/219	14/227
11	25°18/51°31	30/18	36/67	32/51	12/42	9/109	11/82	25/85	27/59	36/72	16/67	10/12	16/28
12	24°27/53°22	35/293	32/251	28/261	13/329	14/310	13/315	24/120	33/83	43/102	17/100	14/38	23/52
13	25°14'/53°51'	33/277	25/267	31/262	12/307	11/316	13/296	18/104	29/81	34/90	14/89	13/39	20/43
14	25°15'/55°16'	35/237	42/247	44/237	12/258	16/297	16/281	8/99	27/80	23/91	9/87	14/37	16/42
15	25°58/56°03	55/192	61/220	62/210	21/212	20/262	20/250	11/357	23/53	21/29	8/36	15/23	16/28
16	26°08/56°28	75/153	74/171	72/174	28/174	27/202	27/202	31/329	34/345	31/341	14/341	18/349	19/353
1- Bandar Abbas, 2- Hengam Island, 3- Tunb Island, 4- Lavan Island, 5- Asaluyeh, 6-Lavar, 7- Khark Island, 8- Shatt al Arab, 9- Mina al Ahmadi, 10- Berri, 11- Ad Dawhah, 12- H. al Mubarras, 13. M1, 14. Dubai, 15- Khor Khwair, 16- Ras Dillah													

d. Heat and freshwater fluxes

The annual mean and basin-averaged heat fluxes, evaporation and precipitation rates in this modeling study are consistent with those in other studies (see Table 4). A positive net heat flux indicates that the PG gains heat at the air-sea boundary layer and releases it through the SOH. The significant difference in evaporation and precipitation rates (E-P) determines the net volume flux entering the inverse system of the PG via the SOH.

The difference between evaporation and precipitation rates (1.32 m/yr) in the PG (see Table 4) is comparable to 1.46±0.24 m/yr in the Red Sea (Nagy et al., 2021).

Table 4- The annual mean values of heat fluxes (W/m^2), evaporation and precipitation rates (m/yr) averaged in the area of the PG (47.6 °E – 56.25 °E) from the CRM in 1997-2001 comparing with those annual mean basin averaged values in earlier studies. Positive and negative values indicate downward and upward directions. Also, NA means not applicable.

	Shortwave	Latent	Sensible	Longwave	Net	Evaporation	Precipitation
Johns et al. (2003)	211	-122	-7	-78	−7±4 to 4	1.58	0.15
Pous et al. (2015)	216.2 to 221.1	-120.1 to -127.3	-6.9 to 9	-80 to -81.8	16.9 to 28.5	1.51 to 1.61	0.21 to 0.24
Rezaei-Latifi et al. (2015)	219	-136	-14	-75	-6	NA	NA
Xue and Eltahir (2015)	257	-146.1	-0.6	-107.6	2.7	1.84	0.08
Lorenz et al. (2020)	209.8	-127.8	-3.0	-83.7	-4.7	1.62	0.11
This study (CRM)	216.16	-114.65	2.05	-93.97	9.59	1.45	0.13

4. Results

a. Volume and salt transports through the Strait of Hormuz

The absolute method (equation 2) indicates that the volumetric inflow-outflow rates at the SOH are higher in the CRM (Fig. 5a) than in NTM (Fig. 5b). This is due to the stronger instantaneous tidal flows compared to the corresponding non-tidal velocities (see Section 5b). The flow rates in the CRM and NTM fluctuate around their time-averaged values of ~ 0.5 Sv and ~ 0.25 Sv, respectively (see Fig. 5a, b). The annual mean isohaline volume transport ($\langle -\frac{\partial Q}{\partial s} \rangle$) at the SOH (Fig.5c) indicates that the exchange flow drives incoming low-salinity water (fresher than 37.68 psu in NTM and 37.92 psu in CRM) into the PG and outgoing high-salinity water (saltier than 37.68 psu in NTM and 37.92 psu in CRM) from the PG. This demonstrates the inverse estuarine system of the PG. These two strong stratified layers originate from the low-salinity IOSW and the high-salinity (dense) PGW masses. Both extreme inflowing and outflowing transports in the TEF analysis are stronger in the NTM than in CRM (see Fig.5c). This is attributed to the NTM having higher stratification, which results in stronger residual (time-averaged) velocities than the CRM at the SOH (see Section 5b). Consequently, the time-averaged inflow-outflow rates exhibit a slight increase from the CRM to NTM in both Eulerian and TEF methods in 1997-2001 (see Table 5).

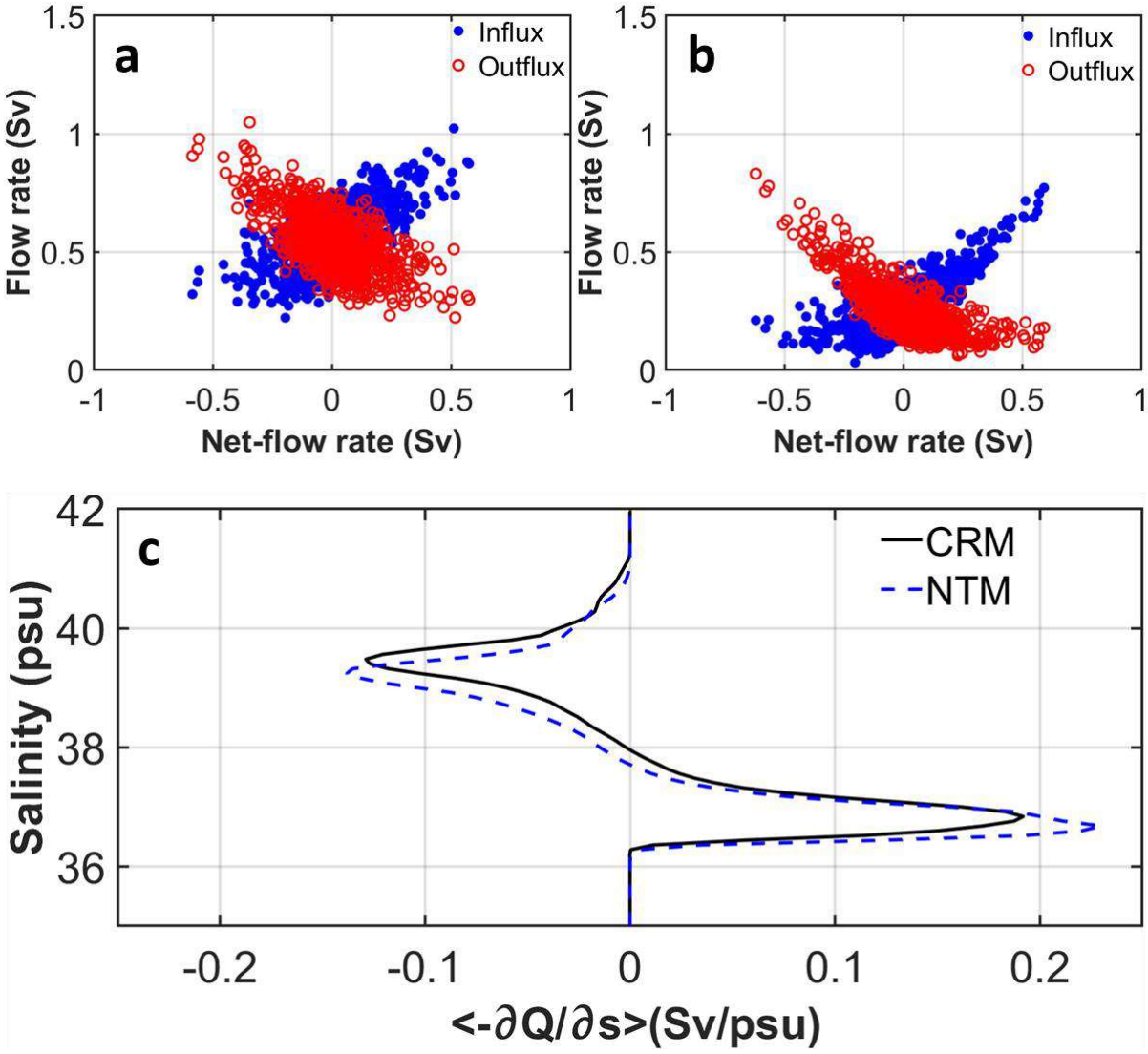

Fig. 5- Volumetric 2-day-mean flow rates resulted from the absolute method of the model runs at the SOH across latitude 26° N during the last 5 years (1997-2001) for the CRM (**a**) and NTM (**b**). The time-averaged isohaline volume transports from the TEF method for the CRM (black line) and NTM (blue dashed line) at the SOH in 1997-2001 (**c**). See the location of the cross-section in Fig. 1. Positive values in (c) mean landward (inflowing waters to the PG). There is no salinity lower than ~36.2 psu and higher than ~41.2 psu at the SOH so $\langle -\frac{\partial Q}{\partial s} \rangle$ equals zero.

The salt flux values are calculated by multiplying the corresponding flow rates (Fig. 5a, b, c) by their salinities. The variations in the salt fluxes and relevant flow rates are nearly identical, therefore are not displayed.

Table 5 confirms that the time-averaged absolute inflow-outflow rates (presented in Fig. 5a, b) and their relevant salt fluxes are more than doubled by adding tidal forcing in 1997 – 2001.

Both CRM and NTM show higher Eulerian annual mean in- and out-fluxes compared to the TEF method (see Table 5). This is attributed to a significant compensation (zero transport) close to the intermediate salinity of 38 psu averaged over the five years (1997 – 2001), resulting in very small transports for salinity classes around 38 psu (see Fig. 5c). However, this compensation is absent in the classical Eulerian approach.

Furthermore, the inflowing and outflowing fluxes are stronger in the absolute approach compared to the Eulerian and TEF methods, especially in the CRM due to the deployment of higher instantaneous (high-frequency) flows.

Table 5- The time-averaged values of flow rates (Sv) and salt fluxes (Sv psu) and the relevant salinities of inflowing and outflowing waters (in-salinity and out-salinity) computed by the absolute, Eulerian and TEF methods through the SOH for the CRM and NTM in 1997-2001. The landward direction (toward the PG) is positive.

Model	NTM			CRM		
Method	Abs.	Eul.	TEF	Abs.	Eul.	TEF
volume influx $\langle Q_{in} \rangle$	0.26	0.18	0.15	0.55	0.17	0.14
volume outflux $\langle Q_{out} \rangle$	-0.25	-0.17	-0.14	-0.54	-0.16	-0.13
net volume flux $\langle Q_{net} \rangle$	0.01	0.01	0.01	0.01	0.01	0.01
salt influx $\langle Q_{in}^{s} \rangle$	9.79	6.82	5.63	20.50	6.44	5.11
salt outflux $\langle Q_{out}^{s} \rangle$	-9.78	-6.81	-5.62	-20.52	-6.46	-5.13
net salt flux $\langle Q_{net}^{s} \rangle$	0.01	0.01	0.01	-0.02	-0.02	-0.02
in-salinity S_{in}	37.07	37.00	36.76	37.56	37.10	36.87
Out-salinity S_{out}	38.42	38.96	39.14	38.17	39.16	39.36

The annual mean in- and out-volume fluxes presented in Table 5, excluding the absolute results from the CRM, agree well with those suggested by previous studies (see Table 1). In particular, the volume exchanges resulting from the absolute method in NTM (see Table 5) are close to the corresponding values in the study by Campos et al. (2020), who calculated volume transports using a non-tidal model at the same cross-section of 26 °N (see Table 1). The volume fluxes from the TEF analysis (see Table 5) are almost in the range of the TEF estimations proposed by Lorenz et al. (2020).

The allocation of high frequencies in the absolute framework results in the inflowing and outflowing volume and salinity fluxes as well as the relevant salinities being strongly influenced by tides (see the absolute results in Table 5). Tides can bring salt waters from deep layers (out-salinity) to mix with low-salinity surface layers (in-salinity). When using the absolute method, the CRM produces higher in-salinity and lower out-salinity compared to NTM (see Table 5). In this method, the difference between the salinities of inflows and outflows considerably decreases from the NTM (~1.35 psu) to the CRM (~0.61 psu), indicating a strong tidal impact in mixing these two different salinities in both vertical and lateral directions at the SOH. However, the difference between the inflowing and outflowing residual salinities changes slightly (<0.12 psu) from the NTM to CRM in the Eulerian and TEF methods (see Table 5). A quantitative assessment of tidal mixing at the SOH is analyzed in Section 5b, which is associated with the role of tides in the formation of landward net salt transport (Section 5a) throughout the PG.

Note that the terms “in-salinity” and “out-salinity” refer to the total inflows and outflows, which may not occur in the same water column. Therefore, their difference may not be an appropriate criterion for measuring vertical stratification.

Additionally, the three methods yield equal net volume fluxes (averaged from 1997 to 2001) and, consequently, the same net salt fluxes (Table 5).

The positive time-averaged net volume fluxes in the CRM and NTM (Table 5) are almost identical, indicating a negligible tidal impact on evaporation, which is computed in the model. This also describes the inverse estuarine system of the PG, where a positive net volume flux emerges as a net-inflow rate to compensate for higher evaporations rather than freshwater inputs by precipitation and river inflow. Unlike the net volume fluxes, the corresponding net salt flux changes from NTM to CRM (see Table 5) due to the influence of different density (salinity) gradients associated with tidal effects on salinity transport.

The annual- and depth-averaged net volume transport per unit width F (here attained by the cross-sectional mean at the SOH) is dominated by the positive non-tidal component F_{nt} ($F \approx F_{nt}$) in 1997 – 2001 (Table 6). This is because the corresponding Stokes drift component (F_{Stokes}) tends to zero. This confirms that barotropic tides have an insignificant influence on net volume transport at the annual time scales. The positive values of F (Table 6) indicate interannual variability caused by varying annual rates of evaporation and freshwater inputs from precipitation and river discharge in the inverse estuary of the PG.

Table 6- The net volume transports predominantly driven by the non-tidal component F_{nt} in the CRM in 1997 – 2001. The landward direction (toward the PG) is positive.

Year	1997	1998	1999	2000	2001
F_{nt} $(\frac{m^2}{s})$	0.40	0.42	0.40	0.39	0.37

Table 7 shows that the direction of the annual net salt flux $\langle Q^s_{net} \rangle$ can change from year to year depending on the strength and direction of the three salt flux components: advection, shear dispersion and tidal oscillation.

The direction of advective salt flux Q^s_a **(**see equation 10) and the net volume flux $\langle Q_{net} \rangle = \langle \iint_A U(y,z,t)dA \rangle = u_a \langle \iint_A dA \rangle$ are generally controlled by u_a (see equation 8). Therefore, landward (positive) values u_a and $\langle Q_{net} \rangle$ coincide with the same landward direction of Q^s_a at the SOH (see Table 7).

The direction of sheared salt transport (Q^s_{sh}) driven by horizontal density gradient reverses from the landward direction in positive estuaries (Aristizábal and Chant, 2015; Valle-Levinson, 2022) to the seaward direction in inverse estuaries. As seen from Table (7), in the PG, the direction of longitudinal (horizontal) density gradient becomes seaward. The seaward (negative) Q^s_{sh} may be strengthened by tides, as Section 4c demonstrates a relatively higher horizontal density gradient in the CRM compared to the NTM.

The salt flux by tidal pumping (Q^s_t) remains negative at the SOH during 1997 – 2001 (see Table 7 and Fig. 6). Thus, the direction of $\langle \mathrm{Q^s_{net}} \rangle$ is determined by the relative strength between positive (landward) component $\mathrm{Q^s_a}$ and the two negative (seaward) components ($\mathrm{Q^s_{sh}}$ and $\mathrm{Q^s_t}$), (see Table 7). Generally, both wind and tidal forcings can influence $\mathrm{Q^s_a}$ and $\mathrm{Q^s_{sh}}$. To eliminate the influence of wind forcing (from tidal forcing and density gradient) on $\langle \mathrm{Q^s_{net}} \rangle$, the salt-flux components are analyzed in the NWM, particularly for 2001 (Section 5a) on which the interaction between density gradient, wind and tidal forcings results in a seaward $\langle \mathrm{Q^s_{net}} \rangle$ in the CRM (see Table 7).

Table 7- The annual mean net salt flux $\langle Q_{net}^{s} \rangle$ from the CRM at the SOH in 1997 – 2001 that is decomposed into the three components of advection (Q_a^s), shear dispersion (Q_{sh}^s) and tidal oscillation (Q_t^s). The landward direction (toward the PG) is positive.

year	$\langle Q_{net}^{s} \rangle$	Q_a^s	Q_{sh}^s	Q_t^s
1997	-0.07	0.26	-0.30	-0.04
1998	0.04	0.35	-0.28	-0.03
1999	0.02	0.35	-0.31	-0.02
2000	-0.05	0.31	-0.35	-0.02
2001	-0.01	0.31	-0.29	-0.04

Fig.6 illustrates the prevalence of negative covariance between tidal velocities and salinities across the SOH-section during 1997 – 2001. This results in negative (seaward) salt transport by tidal pumping (see Table 7). The covariance is calculated at each cell of the cross-section using equation 13 (Thomson and Emery, 2014), where N represents the number of hourly data in the period of 1997 – 2001.

$$cov(S,U) = \frac{1}{N-1}\sum_{i=1}^{N}(S_i - \langle S \rangle)(U_i - \langle U \rangle) \quad (13)$$

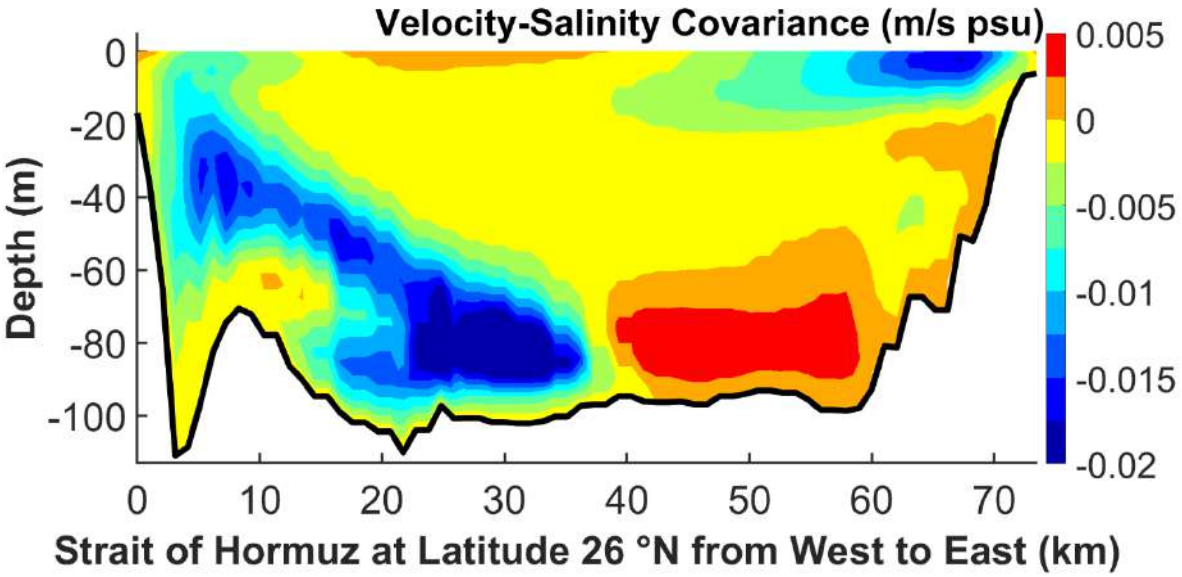

Fig. 6- The covariance between two time series of tidal velocity and salinity at the SOH-section in 1997 – 2001. The dominant negative covariance produces a negative (seaward) tidal pumping salt flux.

b. Knudsen relationship in the Persian Gulf

The Knudsen relationship, incorporating volume and salinity balances, can be defined as equations 14 and 15 (Lorenz et al., 2021). Here, we examine these two equations in the PG.

$$\langle \frac{\partial V}{\partial t} \rangle = \langle Q_{in} \rangle + \langle Q_{out} \rangle + \langle Q_r \rangle + \langle Q_p \rangle + \langle Q_e \rangle \quad (14)$$

where the whole volume of the PG bounded to latitude 26 °N (the SOH cross-section) is detected by $\boldsymbol{V}$ and temporal derivation is denoted by $\frac{\partial}{\partial t}$. $\boldsymbol{Q_{in}}$ and $\boldsymbol{Q_{out}}$ represent the inflowing and outflowing volume fluxes through the SOH, respectively. $\boldsymbol{Q_r}$ refers to river discharge, $\boldsymbol{Q_p}$ and $\boldsymbol{Q_e}$ represent surface freshwater transports through precipitation (with positive values) and evaporation (with negative values) rates, respectively.

$$\langle \frac{\partial}{\partial t} \int S \, dV \rangle = \langle Q_{in} \, S_{in} \rangle + \langle Q_{out} \, S_{out} \rangle \tag{15}$$

in which $\boldsymbol{S}$ is the salinity inside the PG. $\boldsymbol{S_{in}}$ refers to the salinity of inflowing ocean water (in-salinity), and $\boldsymbol{S_{out}}$ is the PG outflowing salinity (out-salinity). The left-hand side of equation (15) represents the time-averaged volume-integrated salt budget, which is the time-averaged value for the time rate of change in net salinity. The sum of the two terms on the right-hand side of the equation (the net salt flux) estimated in the CRM and NTM is presented in Table (5) in the period of 1997 – 2001.

The used model (SCHISM) demonstrates a high level of volume (Fig. 7a, b) and salinity (Fig. 7c, d) conservation in both CRM (Fig. 7a, c) and NTM (Fig. 7b, d). Although, in- and out- volume and salt fluxes differ in the absolute, Eulerian and TEF methods, the resultant net fluxes ($\langle Q_{net} \rangle$, $\langle Q^s_{net} \rangle$) remain the same in all three methods (as confirmed by Table 5).

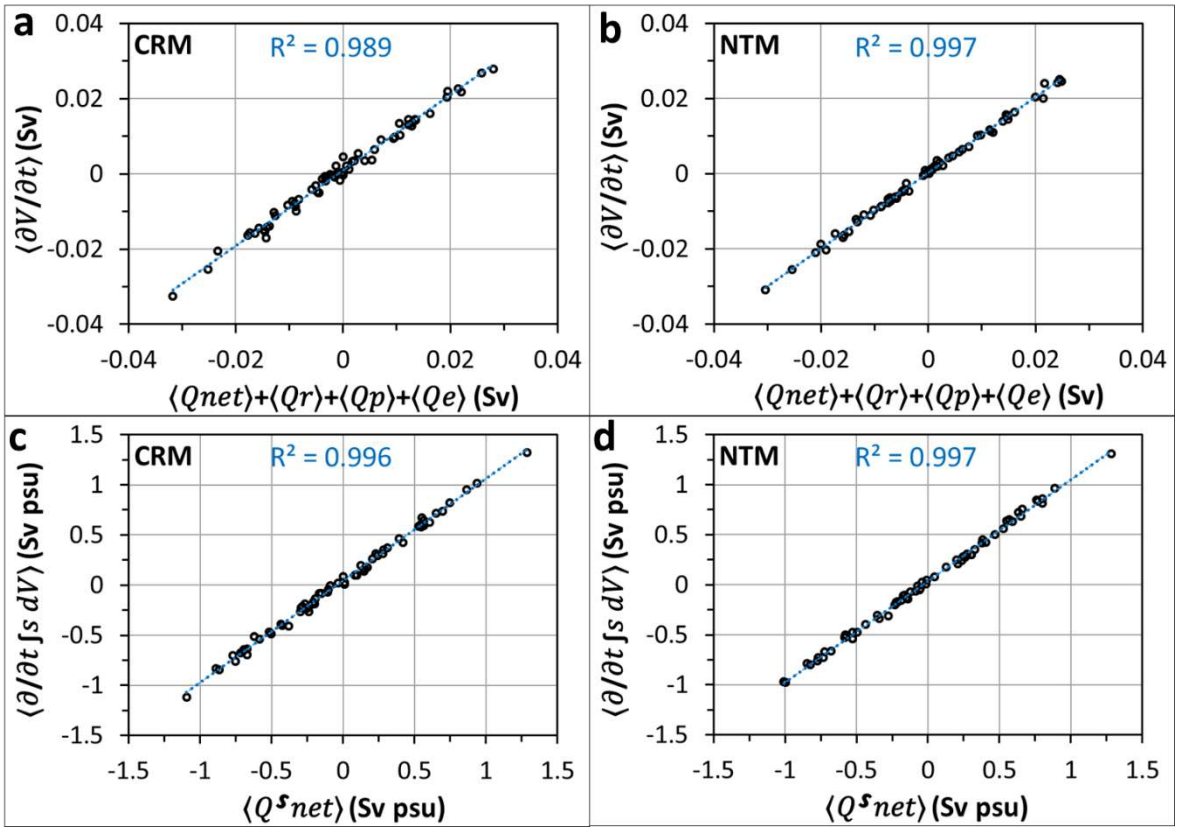

Fig. 7- The scatter plots of time (28 days)-averaged volume balance (**a, b**) and salt conservation (**c, d**) in which $\langle Q_{net} \rangle = \langle Q_{in} \rangle + \langle Q_{out} \rangle$ and $\langle Q^s_{net} \rangle = \langle Q_{in} S_{in} \rangle + \langle Q_{out} S_{out} \rangle$ calculated by the absolute method in the model at the SOH for the CRM (**a, c**) and NTM (**b, d**) during the five years (1997 – 2001).

c. Salinity distributions in the Persian Gulf affected by tides

When comparing the daily mean basin-averaged salinities at the PG-area (47.5° E- 56.25° E) from the CRM (the black line in Fig. 8a) and NTM (the blue dashed line in Fig. 8a), it is evident that tides tend to increase salinity in the PG during 1997 - 2001. The seasonal variability in the PG-salinity is almost the same in both

CRM and NTM (see Fig. 8a), and only the mean salinity is elevated by tides (Fig. 8a) from 40.45 psu in the NTM to 41.30 in the CRM.

In 2001, the sea surface salinity along the PG-thalweg also increases by adding tides from the NTM (Fig 8c) to CRM (Fig. 8b). This increase is particularly noticeable near the PG head, where isohalines higher than 41 psu form in the CRM.

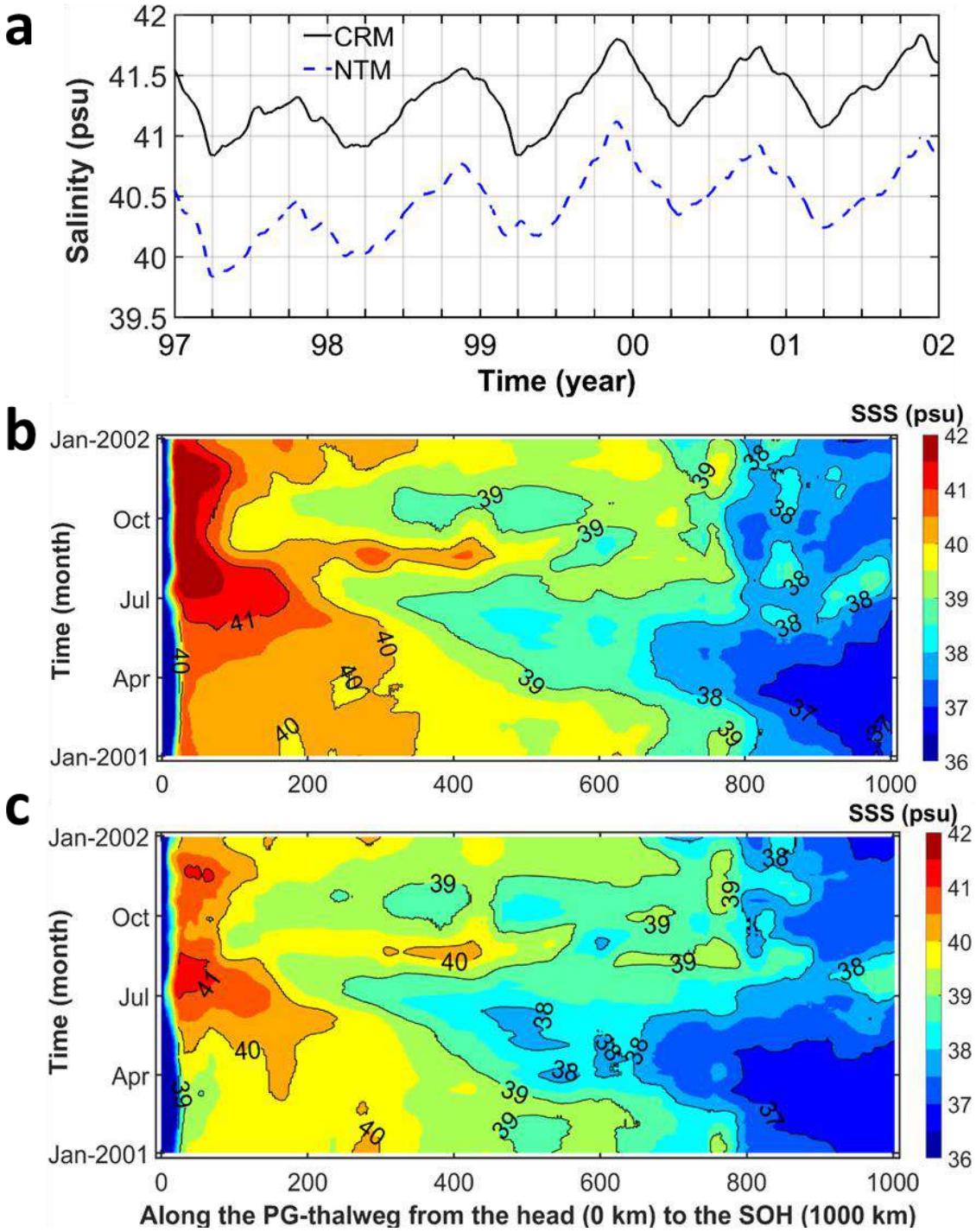

Fig. 8- Time series of daily- and depth-mean salinity averaged at the PG-area (47.5° E- 56.25° E) from the CRM (black line), and the NTM (blue dashed line) during 1997-2001 (**a**). Hovmöller diagrams of daily mean sea surface salinity (SSS), along the PG-thalweg from the mouth of Shat Al-Arab estuary (km 0) to the SOH (km 1000) in 2001 from the CRM (**b**) and the NTM (**c**). A moving average of 28 days is applied in the three figures. The location of the PG-thalweg is detected by the dotted line in Fig. 1.

The increase in the annual averaged inflow and outflow transports imposed by tides in the absolute method (see Table 5) is a direct consequence of the salinity increase over the PG (Fig. 8), which induces an increase in horizontal density variance (gradient) at the PG by adding tidal frequencies (see Fig. 9a, b). The horizontal density variance (Fig. 9a, b) is defined as $\boldsymbol{HDV} = (\overline{\boldsymbol{\rho}} - \overline{\overline{\boldsymbol{\rho}}})^{\boldsymbol{2}}$, as Li et al. (2018) used this concept for salinity. The double overbar $\overline{\overline{\ }}$ denotes volume-averaged values. The horizontal salinity (density) variance is induced by horizontal salinity (density) gradients (Li et al., 2018).

The increase in salinity (density) of the PG enhances the density gradient between the PGW and IOSW at the SOH. For instance, Fig. 9 shows a higher horizontal density gradient during cold months compared to warm months in 2001 near the SOH, especially in the CRM. Similarly, Fig. 2 illustrates almost the same seasonal variation for salinity of the deep PGW mass in December 1996 - March 1998 (the PGW is saltier in the cold month).

Pous et al. (2015) suggested that interannual increases and decreases in the PG-salinity result in similar variations in density gradient. In particular, the same authors showed that the interannual difference between the two water masses of PGW (west of the SOH) and the IOSW (east of the SOH) was highly correlated with the corresponding variations in volume influx through the SOH (see Figure 6c from Pous et al. (2015)).

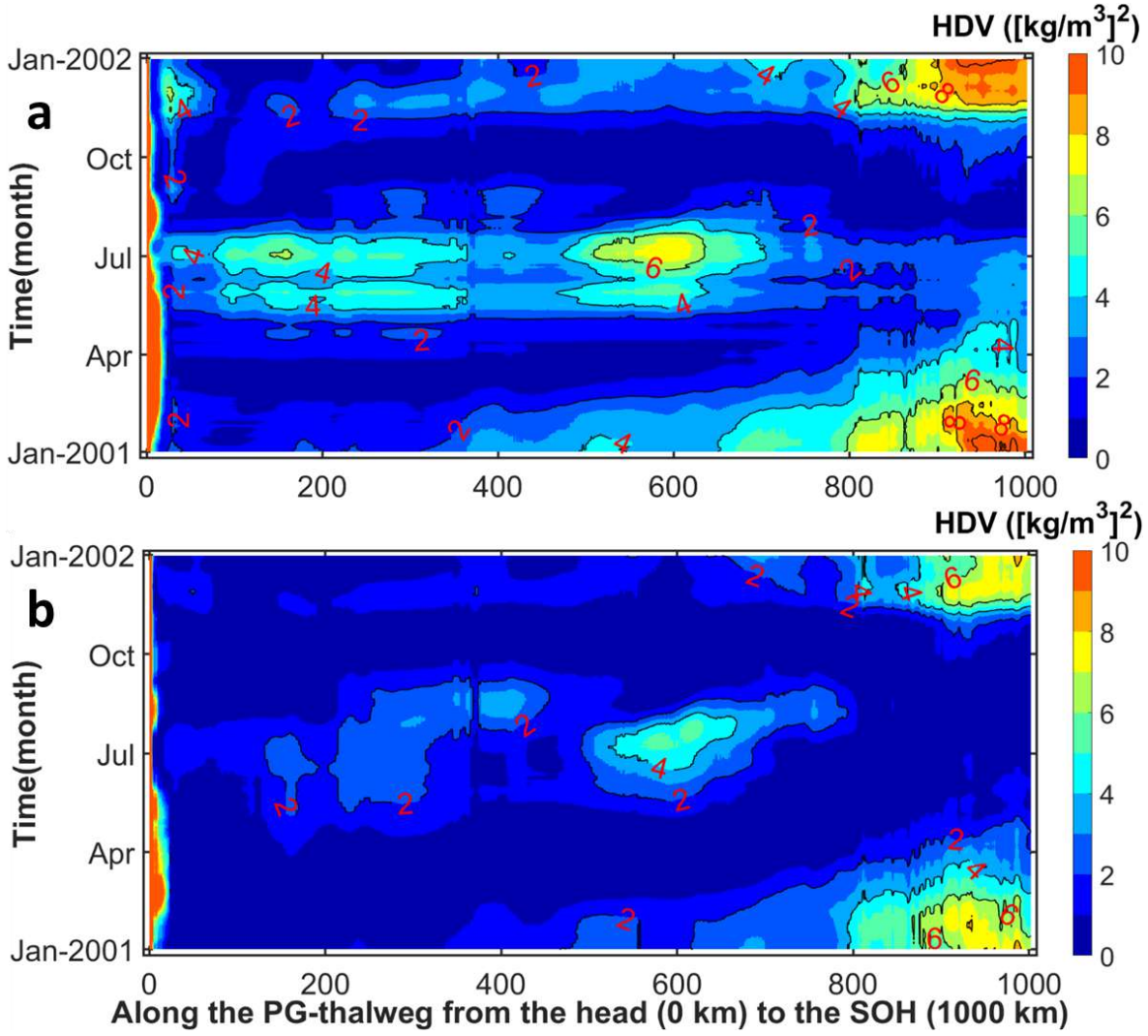

Fig. 9- Hovmöller diagrams of daily mean horizontal density variance (HDV) along the PG-thalweg from the mouth of Shat Al-Arab estuary (km 0) to the SOH (km 1000) in 2001 from the CRM (**a**) and the NTM (**b**). A moving average of 28 days is applied in both figures. The location of the PG-thalweg is detected by the dotted line in Fig. 1.

In early summer (June and July), the low-salinity IOSW intrudes longer distance along the thalweg compared to late fall and early winter (see the isohaline lower than 39 psu exceeding 600 km toward the head in Fig. 8b, c). This is attributed to a peak in horizontal density gradient in June and July around 600 km (see Fig. 9a, b), located north of Qatar peninsula at 51 °E (see Fig. 1). This finding is in agreement with prior studies (Kämpf and Sadrinasab, 2006), Thoppil and Hogan (2010) and Yao and Johns (2010a). They proposed that the IOSW, which serves as the northern flank of the PG-circulation, seldom extends north of Qatar during cold months due to weakened buoyancy forcing.

Close to the river mouth (km 0), HDV is stronger in the first six months compared to the second half of the year (Fig. 9) because of higher river discharge in winter and spring, which leads to increased density differences with adjacent high-salinity waters.

d. Vertical stratification in the Persian Gulf affected by tides

In order to investigate tidal impacts on vertical stratification, Fig. 10 uses the concept of vertical density variance $\boldsymbol{VDV} = (\boldsymbol{\rho} - \overline{\boldsymbol{\rho}})^2$ in which $\boldsymbol{\rho} - \overline{\boldsymbol{\rho}}$ is the vertical deviation of density from its depth-averaged value at each point. This concept is similar to the vertical salinity variance (Burchard and Rennau, 2008; Li et al., 2018) that can be used as a criterion to measure vertical stratification (Li et al., 2018). This variance is applied in this study but for density. In contrast to the increase in horizontal density variance HDV (gradient), (see Fig. 9a, b), tides slightly reduce VDV (vertical stratification) in the PG-area (Fig. 10).

Fig. 10 also illustrates that strong vertical stratifications occur during the warm months in both CRM, NTM, which transition to weak stratifications during the cold months. This is because the longer intrusion of the IOSW into the PG during warm months (see Fig. 8b, c), associated with the formation of a seasonal thermocline at the same time (Beal et al., 2000; Reynolds, 1993).

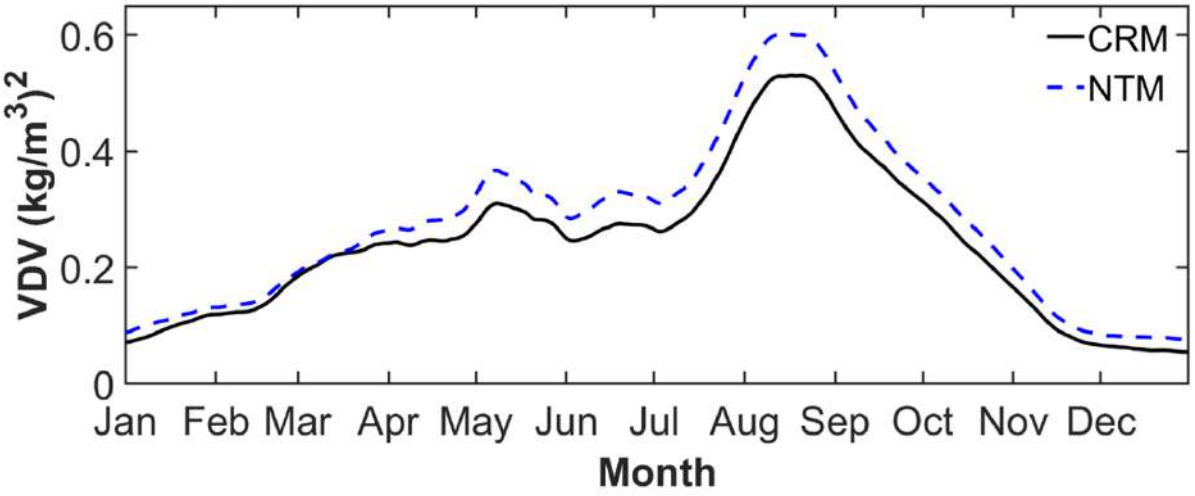

Fig. 10- Time series of daily and depth- mean vertical density variance VDV averaged at the PG-area (47.5° E-56.25° E) from the CRM (black line), and the NTM (blue dashed line) in 2001.

5. Discussion

a. Salt transports affected by tides

To quantify the tidal contribution to the advective salt transport, we decompose the net salt flux from the NWM at seven cross-sections (Fig. 11a) from the PG-head (the "Head" cross-section) to the SOH (latitude 26 °N or the "Strait" cross-section) in 2001 (see the seven cross-sections in Fig. 11b). In the inverse estuarine system of the PG, tides are the primary driver of advective salt flux in the absence of wind. The tidal advection is often the strongest salt flux component driving the annual mean net salinity transport (see Fig. 11a). In

contrast to the two seaward (negative) salt fluxes by shear dispersion and tidal oscillation, the advective salt transport mainly remains landward (positive) at all cross-sections except at the PG-head (see Fig. 11a and Table 7). The directions of the net volume flux and the advective salt flux are the same throughout the PG (see Fig. 11a), as confirmed by Table 7 for the SOH. In the absence of wind forcing, the tidal advective salt transport is usually landward in inverse estuarine systems which can be reversed to the seaward direction in positive estuaries due to riverine advective flux (Hosseini et al., 2023).

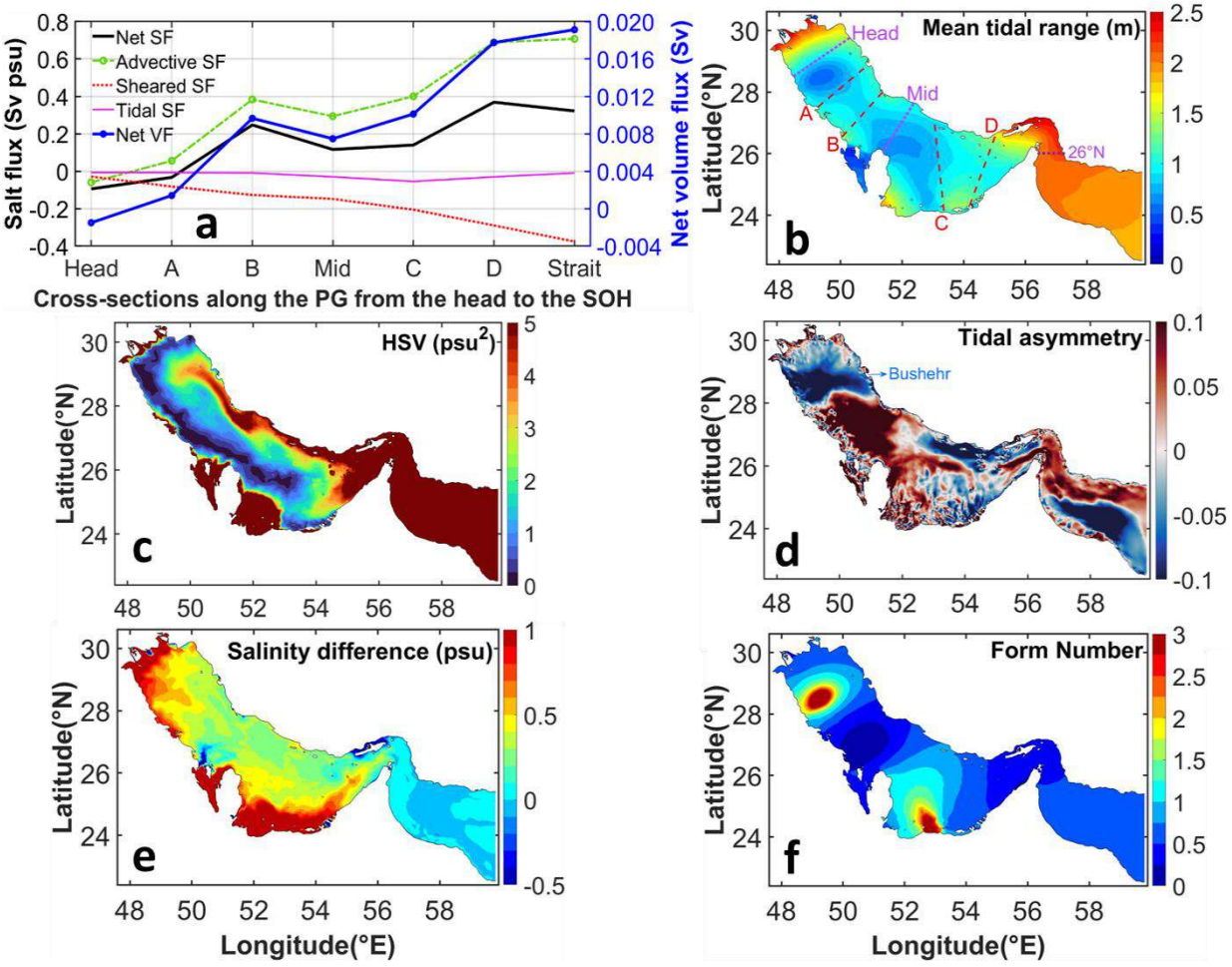

Fig. 11- (a) The distributions of annually averaged salt flux (SF) components and the net volume flux (Net VF) at the seven cross-sections perpendicular to the PG-thalweg from the head to the SOH (latitude 26 °N) and (**c**) the annually averaged horizontal salinity variance HSV resulting from the NWM in 2001. (**b**), (**d**) and (**f**) respectively present mean tidal range (height), tidal velocity asymmetry and the tidal Form number from the CRM at the PG in 2001. (**e**) The CRM-NTM differences between their depth-mean salinities in 2001. The seven cross-sections from the head to the SOH (latitude 26 °N) are shown in (b). The net salt flux (Net SF) in (a) is decomposed into three terms of advection, shear dispersion and tidal oscillation. Positive fluxes are landward (toward the PG-head).

In inverse estuarine systems, both salt transports by seaward shear dispersion and landward tidal advection decrease from the mouth toward the head (see Fig. 11a and Hosseini et al. (2023)). The landward decrease of the sheared salt flux is linked to the corresponding variation in the horizontal salinity gradient, decreasing toward the PG-head (see Fig. 11c).

The NWM experiences a landward decrease in the tidal advective salt flux because this salt flux is predominantly driven by tidal changes in water level (see Fig. 11b). Similarly, Aristizábal and Chant (2015) found that changes in sea surface height caused by wind forcing were the main driver of the advective salt flux in Delaware Bay. In this bay, the advective salt flux varied between seaward and strongly landward values. The

mean tidal range (height) (Fig. 11b) decreases from the SOH to the “D”, “C” and “Mid” cross-sections, coincident with the tidal advective salt flux (Fig. 11a). Then both mean tidal height and advective salt flux slightly increase to cross-section "B" and decrease again to cross-section A, (see Fig. 11a, b). The mean tidal height shows another minimum between the “A” and “Head” cross-sections and then strengthens landward peaking at the northwesterly coastal (land) boundary.

At cross-section A, the landward tidal advective salt flux weakens as u_a decreases with increasing bottom friction in the shallow depths of this cross-section. Consequently, the net salt flux becomes seaward, as the combined effect of seaward salt transports by shear dispersion and tidal pumping outweighs the landward advective salt transport.

The negative (seaward) values of tidal advective salt flux and the net volume flux at cross-section "Head" may be attributed to the landward increase of tidal height at the PG-head, contrary to its typical seaward enhancement at the east part of the PG.

In an inverse estuary, salt is transported from the estuary mouth to the head by tidal advection. Consequently, salinity increases towards the head (landward direction), which is associated with high evaporation rates. This landward salt transport is damped near the estuarine head due to decreasing depth (increasing friction) and declining u_a. As u_a tends towards zero due to bottom friction of shallow areas, salt accumulates. Residual tidal flows from this area with $u_a \sim 0$ to the upstream coastal boundary, are influenced by tidal asymmetry. Here, tidal asymmetry (TA) in velocity is defined by equation (16):

$$\mathrm{TA} = (\bar{v}_f - |\bar{v}_e|)/(\bar{v}_f + |\bar{v}_e|) \quad (16)$$

in which $\bar{v}_f$ and $\bar{v}_e$ are the mean of depth-averaged velocities during flood and ebb tidal phases, respectively (Mantovanelli et al., 2004). When a positive tidal velocity asymmetry is present, the residual tidal flows, u_a, the relevant net volume flux, and tidal advective salt transport are flood oriented. Conversely, for a negative tidal asymmetry, they are oriented towards the ebb-velocity direction.

The tidal asymmetry is associated with non-linear interactions between tidal waves and boundary limits, as well as between incoming and reflected tidal waves (Uncles et al., 1985; Van de Kreeke, 2018). The tidal asymmetry can affect tidal residual flows and consequently u_a may become rectified to a weak seaward (in the direction of ebb currents) or landward (in the direction of tidal flood flows) flow at the shallow frictional areas near the coastal boundary. At the head of the PG, the low seaward u_a results in a weak seaward net volume flux and advective salt flux, resembling a positive estuary (see Fig. 11a), despite behaving as an inverse estuary and contributing to the dense PGW mass. The negative (seaward) values in this case can be explained by the ebb-dominated tidal asymmetry at the head of the PG (see Fig. 11d) and standing waves generated by the interaction between incoming and reflected tidal waves from the northwestern coastal boundary (see Fig. 11b, f).

The distribution of flood and ebb asymmetries around the SOH (see Fig. 11d) agrees with the tidal asymmetries observed in the study by Azizpour et al. (2016). The ebb-dominated asymmetry was also observed at the northwestern Iranian coasts (Bushehr Port, see (Hosseini et al., 2016).

In 2001, the value of u_a at the "Head" cross-section is negative and negligible, which is largely due to the proximity of the cross-section to the northwestern coastal boundary. As a result, this cross-section experiences low seaward net volume flux and advective salt flux in the absence of wind forcing (see Fig. 11a).

The seaward advective salt flux by the riverine inflow has a local impact on the northwestern coast and does not reach the "Head" cross-section. For instance, the advective salt flux near the river mouth (-0.044 Sv psu) is lower than that at the "Head" cross-section (-0.060 Sv psu in Fig. 11a).

Reflected tidal waves from the northwestern land boundary of the PG interfere with incoming waves and generate standing wave with a node (minimum tidal range) near the “Head” cross-section (see Fig. 11b, f) and an antinode (maximum tidal range) along the northwestern coastal boundary (see Fig. 11b).

A comparable mechanism also operates on the southern coast, between the Qatar peninsula and the SOH, with a complex tidal asymmetry (see Fig. 11d). This is due to the complex bathymetry and coastal geometry on

the shallow banks and around small islands. Another node forms east of Qatar near this coastal boundary (Fig. 11b, f) coinciding with negligible residual tidal flows and net volume flux in 2001.

To summarize, the tidal advective salt flux is driven by changes in the mean tidal height and typically becomes landward in the inverse estuary of the PG over annual time scales. However, at the PG-head, reflected tidal waves and ebb-directed tidal asymmetry dominate. Additionally, this landward salt flux often intensifies towards the SOH (see Fig. 11a) due to the oceanward rise of the mean tidal height. Thus, the salinity is transported into the PG by the tidal advective term, in contrast to the seaward salt transports by tidal oscillation and the sheared dispersion. The landward salt flux by tidal advection is mostly stronger than the two seaward salt fluxes induced by shear dispersion and tidal oscillation (see Fig. 11a). Therefore, the relevant net salt flux typically becomes landward in the NWM. Winds, in turn, may affect the landward net salt flux, depending on the strength and direction of the wind forcing. The distribution of the tidal Form number $(A_{K_1} + A_{O_1})/(A_{M_2} + A_{S_2})$ in the PG shows two semi-diurnal amphidromic points (tidal diurnal regime with the Form number > 3) and one diurnal node (semi-diurnal tidal regime with the Form number < 0.25) (Fig. 11f). Beyond these three points, the PG experiences a mixed tidal regime mainly diurnal or semi-diurnal tide. The locations of the amphidromic points in Fig. 11f align with earlier studies (Hoseini and Soltanpour, 2022; Pous et al., 2012; Reynolds, 1993). Beyond these three points, the PG experiences a mixed tidal regime mainly diurnal or semi-diurnal tide. This tidal regime is complex and indicates a high tidal range of over 2 m at the SOH, primarily between Qeshm Island and Iranian coasts (see the location in Fig.1) and along the northwestern coasts (Fig. 11b). In contrast, low tidal ranges of less than 0.5 m occur west and south of Bahrain Island located between cross-sections "B" and "Mid" (see Fig. 11b).

Fig. 11e confirms that salinity transport into the PG through the SOH is closely tied to tides and follows the northwestern and southern coastal areas, where u_a significantly diminishes. Higher salinities of about 1 psu in the CRM than in the NTM occur in these shallow water areas and are deflected to the right-hand side by the Coriolis force. The difference in depth-averaged salinity between the two experiments decreases towards the SOH and approaches zero, or even becomes negative, in the Oman Sea (Fig. 11e).

b. Impacts of tidal mixing at the Strait of Hormuz

The time series of the total salt flux, ($\iint_A USdA$), from the CRM (Fig. 12a) and NTM (Fig. 12b) during six M2-tidal cycles (75 hours) at the SOH are mainly controlled by the corresponding cross-sectionally averaged flows, especially in the CRM (see the blue and black lines in Fig. 12a, b). This emphasizes the importance of strong tidal flows at the SOH in producing a robust total salt flux. The peaks of the normal velocity and total salt flux in the CRM are approximately six times higher than those in the NTM. However, the range of cross-sectionally averaged salinity remains relatively consistent from the CRM to the NTM over the 75-hour period (see the red lines in Fig. 12a, b). During this time, the difference between the time-averaged inflowing salinity ($S_{in}^{Abs} = \frac{Q_{in}^{s,Abs}}{Q_{in}^{Abs}}$) and outflowing salinity ($S_{out}^{Abs} = \frac{Q_{out}^{s,Abs}}{Q_{out}^{Abs}}$) across the section is 1.025 psu in the NTM, decreasing to approximately 0.3 psu in the CRM. This indicates that the PG undergoes significant mixing due to tides, particularly in the SOH. At this strait, tides not only enhance the landward net salt flux through the advective salt flux (see Fig. 11a) but also reinforce mixing throughout the cross-section (see Fig. 12c, d).

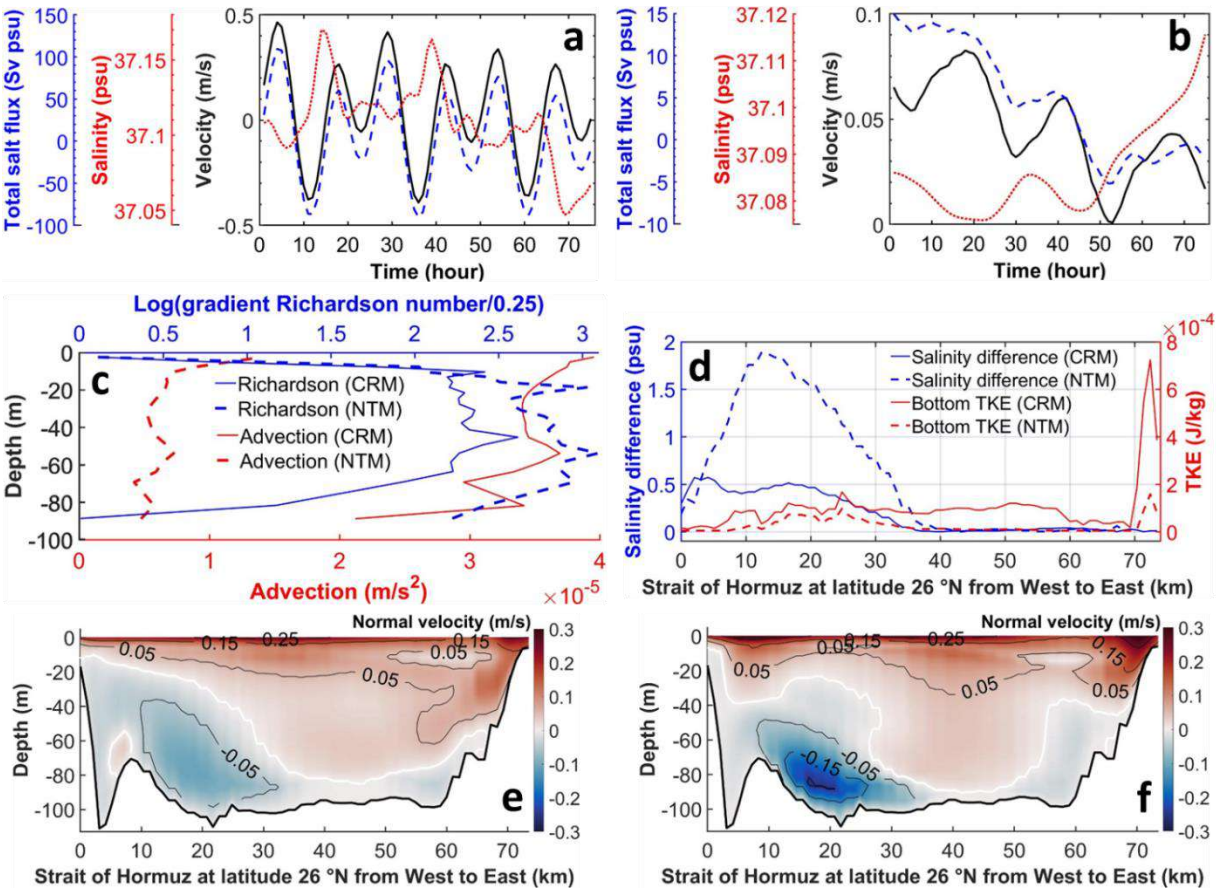

Fig. 12- Time series of total salt flux and cross-sectionally averaged salinity and normal velocity at the cross-section of latitude 26° N (SOH) during 75 hours from the CRM (**a**) and NTM (**b**). The time- (75 hours) averaged laterally-mean advective acceleration (from the momentum equations) and log(gradient Richardson number/0.25) (**c**), and the difference between the time- averaged inflowing and outflowing salinities along with the time-averaged bottom turbulent kinetic energy TKE (**d**) at the SOH cross-section. Vertical profiles of time-averaged normal velocity from CRM (**e**) and NTM (**f**) at the SOH. Flows and net salt flux toward the PG (landward) are positive in (a) and (b). Similarly, positive (red color) and negative (blue color) values in (e) and (f) indicate inflow and outflow, respectively.

Fig. (12c) shows that as advection (the numerator in Equation 12) increases from the NTM to the CRM at the SOH (the cross-section of 26° N) on the tidally-averaged timescale, the gradient Richardson number (stratification) decreases in the CRM. Both advection and gradient Richardson number are directly computed by the model. Also, the difference between the time-averaged outflowing and inflowing salinity decreases from the NTM to the CRM along the section, especially near the western side (Fig. 12d). Conversely, the time-averaged bottom turbulent kinetic energy increases from the NTM to the CRM, particularly close to the Iranian (eastern) side (Fig. 12d), highlighting the importance of tidal mixing across the SOH. At latitude 26 °N, tidal mixing becomes stronger from west to east, which laterally mixes the dense PGW of the western part with the low-salinity IOSW at the eastern side. The locations of the two inflowing (positive) and outflowing (negative) velocities from the CRM and NTM at the cross-section are demonstrated in Fig. 12e, f, respectively.

When comparing the vertical profiles of time-averaged normal velocity (the 75-hour averaged v-velocity) at the cross-section of latitude 26 °N from the two models, it is evident that both inflowing IOSW and outflowing PGW masses have higher peak velocities in the NTM (Fig. 12f) than in CRM (Fig. 12e). In particular, the outflowing PGW exhibits a considerably higher velocity in the NTM, about 20 km from the western coast (see Fig. 12e, f). This outflow is also deeper along the Iranian coast (east of latitude 26°N) in the CRM (deeper than 60 m) than in the NTM (deeper than 40 m). These changes in the PGW mass from the NTM to the CRM are

related to the impacts of tidal mixing. In other words, stronger stratification in the NTM results in stronger flows at the SOH. The time-averaged velocity in CRM represents residual tidal flows, which are different from the non-tidal flows in NTM. The CRM includes non-linear interactions of tidal flows with the bottom topography. These interactions are represented by the advection terms in the momentum equations (Lavín and Marinone, 2003). The respective advection terms weaken the stratification (strengthen mixing), resulting in lower tidally averaged (residual) inflows and outflows.

c. Tides vs density gradient

Two types of dynamics in the PG are identified by T_f, which is a non-dimensional number that quantifies the competition between tidal forcing and density gradient (Fig. 13): (1) a tidally driven regime in the northwestern and southern shallow banks, where $Log(T_f) > 1$ (red color in Fig.13), and (2) a mixed, tidally and density-driven, regime ($0 \leq Log(T_f) \leq 1$) in the western and central PG toward the SOH (orange and yellow colors in Fig.13). The interior of the Oman Sea is an area dominated by a density-driven regime ($Log(T_f) < 0$).

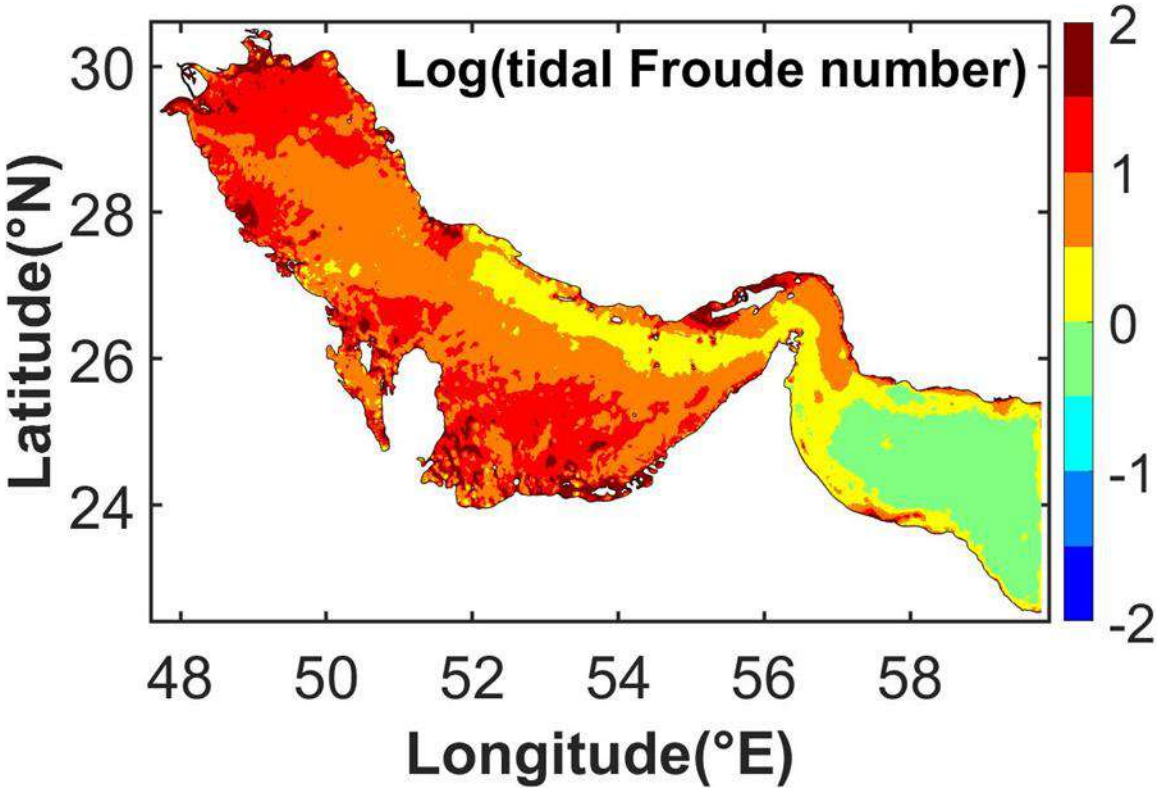

Fig. 13- The tidal Froude number (equation 12) from the CRM in 2001.

The absence of zones with $Log(T_f) < 0$ at the PG and SOH indicates that baroclinicity alone cannot drive residual flows (Fig. 13). In particular, exchange flows through the SOH are driven by both tidal forcing and baroclinicity. It should be noted that previous studies (Campos et al., 2020; Chao et al., 1992; Kämpf and Sadrinasab, 2006; Yao and Johns, 2010b) only considered the density gradient as the primary factor controlling the exchange flows through the SOH.

The northwestern and southern shallow banks of the inverse estuary PG exhibit considerably higher salinity in the CRM than in NTM (Fig. 11e). These areas are identified as tidally driven systems with high values of $T_f > 10$ (Fig. 13).

Conclusion

The results show that the annual inflow-outflow rates through the SOH increase to ~ ±0.54 Sv when tides are taken into account. Although tidal stokes drift insignificantly changes the annual net-inflow rate, tidal mixing can weaken residual (time-averaged) velocities at the SOH. The annual mean salt transport by advection is consistently landward in the SOH, aligning with the landward direction of the net-inflow rate. Conversely, the sheared salt transport driven by horizontal salinity gradient becomes seaward in the inverse estuary of the PG, which contrasts with the landward direction of this salt flux in positive estuaries. The covariance between tidal velocity and salinity remains a small negative value at the SOH on annual time scales, resulting in a low negative (seaward) tidal pumping salt flux. Therefore, the direction of the net salt flux through the SOH can change between landward and seaward directions depending on the relative strength of the landward advective salt flux against the two seaward salt fluxes caused by shear dispersion and tidal oscillation. Finally, this study provides three explanations of why tides tend to increase salinity at the PG:

(1) ***The strong landward salt flux by tidal advection:*** In the absence of wind, the landward salt flux by tidal advection is usually stronger than the two seaward fluxes resulting from the shear dispersion and tidal oscillation in the PG. Thus, the relevant net salt flux is typically directed landward leading to an influx of salt into the PG.

(2) ***Strong tidal mixing at the SOH:*** Tides bring salt waters from deep layers to mix with the low-salinity surface layers at the SOH. This results in an increase in inflowing surface salinity and a decrease in the salinity of outflowing deep waters.

(3) ***The formation of tidal standing waves in the northwestern and southern coasts:*** When $T_f > 10$, tidal standing waves form due to interactions between incoming and reflected tidal waves from the northwestern and southern coastal boundaries. This causes salt to accumulate in the shallow banks of the PG.

The salinity increase over the PG by adding tidal frequencies, results in the significant increase in inflowing-outflowing volume transports enhancing horizontal density gradient.

Acknowledgments

This study contributes to the theme “C3: Sustainable Adaption Scenarios for Coastal Systems” of the Cluster of Excellence EXC 2037 ‘CLICCS - Climate, Climatic Change, and Society’ – Project Number: 390683824 funded by the Deutsche Forschungsgemeinschaft (DFG, German Research Foundation) under Germany’s Excellence Strategy. This study used data from the FES, CMEMS and ECMWF. The authors express their gratitude to Dr. Marvin Lorenz (Leibniz Institute for Baltic Sea Research, Germany) for making available the observational data. We also thank him (Dr. Marvin Lorenz) and Dr. Jilian Xiong (University of Washington, Seattle, USA) for their helpful comments on the calculation of volume and salinity fluxes.

Funding

Open Access funding enabled and organized by Deutsche Forschungsgemeinschaft, CCLICCS-C3: 390683824.

Data availability

The datasets generated or analyzed in this study are available upon request by email to the corresponding author.

Declarations

Conflict of interest The authors declare that there were no commercial or financial interests that might be perceived as conflicts of interest affecting the research.

References

Ackleson, S.G., Pitts, D.E., Sullivan, K.D., Reynolds, R.M.J.G.I., 1992. Astronaut observations of the Persian (Arabian) gulf during STS-45. Geocarto International, 7(4), 59-68. https://doi.org/10.1080/10106049209354389.

Ahmad, F., Sultan, S.J.A.-O., 1991. Annual mean surface heat fluxes in the Arabian Gulf and the net heat transport through the Strait of Hormuz. Atmosphere-Ocean, 29(1), 54-61. https://doi.org/10.1080/07055900.1991.9649392.

Al-Shehhi, M.R., Song, H., Scott, J., Marshall, J.J.J.o.P.O., 2021. Water mass transformation and overturning circulation in the Arabian Gulf. Journal of Physical Oceanography, 51(11), 3513-3527. https://doi.org/10.1175/JPO-D-20-0249.1.

Alessi, C.A., Hunt, H.D., Bower, A.S., 1999. Hydrographic Data from the US Naval Oceanographic Office: Persian Gulf, Southern Red Sea, and Arabian Sea, 1923-1996 (No. 99). Woods Hole Oceanographic Institution.

Alosairi, Y., Alsulaiman, N., Petrov, P., Karam, Q.J.M.P.B., 2019. Responses of salinity and chlorophyll-a to extreme rainfall events in the northwest Arabian Gulf: Emphasis on Shatt Al-Arab. Marine Pollution Bulletin, 149, 110564. https://doi.org/10.1016/j.marpolbul.2019.110564.

Alosairi, Y., Alsulaiman, N., Rashed, A., Al-Houti, D.J.M.P.B., 2020. World record extreme sea surface temperatures in the northwestern Arabian/Persian Gulf verified by in situ measurements. Marine Pollution Bulletin, 161, 111766. https://doi.org/10.1016/j.marpolbul.2020.111766.

Alosairi, Y., Pokavanich, T.J.M.P.B., 2017. Residence and transport time scales associated with Shatt Al-Arab discharges under various hydrological conditions estimated using a numerical model. Marine Pollution Bulletin, 118(1-2), 85-92. https://doi.org/10.1016/j.marpolbul.2017.02.039.

Aristizábal, M.F., Chant, R.J.J.o.G.R.O., 2015. An observational study of salt fluxes in Delaware Bay. Journal of Geophysical Research: Oceans, 120(4), 2751-2768. https://doi.org/10.1002/2014JC010680.

Azizpour, J., Siadatmousavi, S.M., Chegini, V.J.E., Coastal, Science, S., 2016. Measurement of tidal and residual currents in the Strait of Hormuz. Estuarine, Coastal and Shelf Science, 178, 101-109. https://doi.org/10.1016/j.ecss.2016.06.004.

Beal, L.M., Ffield, A., Gordon, A.L.J.J.o.G.R.O., 2000. Spreading of Red Sea overflow waters in the Indian Ocean. Journal of Geophysical Research: Oceans, 105(C4), 8549-8564. https://doi.org/10.1029/1999JC900306.

Burchard, H., Bolding, K., Feistel, R., Gräwe, U., Klingbeil, K., MacCready, P., Mohrholz, V., Umlauf, L., van der Lee, E.M.J.P.i.o., 2018. The Knudsen theorem and the Total Exchange Flow analysis framework applied to the Baltic Sea. Progress in oceanography, 165, 268-286. https://doi.org/10.1016/j.pocean.2018.04.004.

Burchard, H., Rennau, H.J.O.M., 2008. Comparative quantification of physically and numerically induced mixing in ocean models. Ocean Modelling, 20(3), 293-311. https://doi.org/10.1016/j.ocemod.2007.10.003.

Campos, E.J., Gordon, A.L., Kjerfve, B., Vieira, F., Cavalcante, G.J.P.o., 2020. Freshwater budget in the Persian (Arabian) Gulf and exchanges at the Strait of Hormuz. Plos one, 15(5), e0233090. https://doi.org/10.1371/journal.pone.0233090.

Chao, S.Y., Kao, T.W., Al-Hajri, K.R.J.J.o.G.R.O., 1992. A numerical investigation of circulation in the Arabian Gulf. Journal of Geophysical Research: Oceans, 97(C7), 11219-11236. https://doi.org/10.1029/92JC00841.

Hassanzadeh, S., Hosseinibalam, F., Rezaei-Latifi, A.J.O., Studies, H., 2012. Three-dimensional numerical modeling of the water exchange between the Persian Gulf and the Gulf of Oman through the Strait of

Hormuz. Oceanological and Hydrobiological Studies, 41, 85-98. https://doi.org/10.2478/s13545-012-0010-6.

Hoseini, S.M., Soltanpour, M.J.O.S.J., 2022. Numerical Study of Influencing Factors on Tidal Wave Propagation in the Persian Gulf. Ocean Science Journal, 57(4), 642-671. https://doi.org/10.1007/s12601-022-00091-x.

Hosseini, S.T., Chegini, V., Sadrinasab, M., Siadatmousavi, S.M., Yari, S.J.O.S.J., 2016. Tidal asymmetry in a tidal creek with mixed mainly semidiurnal tide, bushehr Port, Persian Gulf. Ocean Science Journal, 51, 195-208. https://doi.org/10.1007/s12601-016-0017-9.

Hosseini, S.T., Stanev, E., Pein, J., Valle-Levinson, A., Schrum, C.J.F.i.M.S., 2023. Longitudinal and lateral circulation and tidal impacts in salt-plug estuaries. Frontiers in Marine Science, 10, 1152625. https://doi.org/10.3389/fmars.2023.1152625.

Johns, W., Yao, F., Olson, D., Josey, S., Grist, J., Smeed, D.J.J.o.G.R.O., 2003. Observations of seasonal exchange through the Straits of Hormuz and the inferred heat and freshwater budgets of the Persian Gulf. Journal of Geophysical Research: Oceans, 108(C12). https://doi.org/10.1029/2003JC001881.

Kämpf, J., Sadrinasab, M., 2006. The circulation of the Persian Gulf: a numerical study. Ocean Science, 2(1), 27-41. https://doi.org/10.5194/os-2-27-2006.

Khosravi, M., Siadatmousavi, S.M., Vennell, R., Chegini, V.J.O.D., 2018. The transverse dynamics of flow in a tidal channel within a greater strait. Ocean Dynamics, 68, 239-254. https://doi.org/10.1007/s10236-017-1127-3.

Kuo, A., Park, K.J.D., Estuaries, E.i., Zone, t.C., 1992. Transport of Hypoxic Waters: An Estuary-Subestuary Exchange. Dynamics and Exchanges in Estuaries and the Coastal Zone, 40, 599-615. https://doi.org/10.1029/CE040p0599.

Lavín, M., Marinone, S.J.N.P.i.G.F.D.A.t.t.t.s.w.o.P.R., 2003. An overview of the physical oceanography of the Gulf of California. Nonlinear Processes in Geophysical Fluid Dynamics: A tribute to the scientific work of Pedro Ripa, 173-204. https://doi.org/10.1007/978-94-010-0074-1_11.

Lerczak, J.A., Geyer, W.R., Chant, R.J.J.J.o.P.O., 2006. Mechanisms driving the time-dependent salt flux in a partially stratified estuary. Journal of Physical Oceanography, 36(12), 2296-2311. https://doi.org/10.1175/JPO2959.1.

Li, X., Geyer, W.R., Zhu, J., Wu, H.J.J.o.P.O., 2018. The transformation of salinity variance: A new approach to quantifying the influence of straining and mixing on estuarine stratification. Journal of Physical Oceanography, 48(3), 607-623. https://doi.org/10.1175/JPO-D-17-0189.1.

Lorenz, M., Klingbeil, K., Burchard, H.J.J.o.G.R.O., 2020. Numerical study of the exchange flow of the Persian Gulf using an extended total exchange flow analysis framework. Journal of Geophysical Research: Oceans, 125(2), e2019JC015527. https://doi.org/10.1029/2019JC015527.

Lorenz, M., Klingbeil, K., Burchard, H.J.J.o.P.O., 2021. Impact of evaporation and precipitation on estuarine mixing. Journal of Physical Oceanography, 51(4), 1319-1333. https://doi.org/10.1175/JPO-D-20-0158.1.

Lorenz, M., Klingbeil, K., MacCready, P., Burchard, H.J.O.S., 2019. Numerical issues of the Total Exchange Flow (TEF) analysis framework for quantifying estuarine circulation. Ocean Science, 15(3), 601-614. https://doi.org/10.5194/os-15-601-2019.

Lyard, F., Carrere, L., Cancet, M., Guillot, A., Picot, N.J.O.D., in preparation, 2017. FES2014, a new finite elements tidal model for global ocean. Ocean Dynam., in preparation, 10.

MacCready, P.J.J.o.P.O., 2011. Calculating estuarine exchange flow using isohaline coordinates. Journal of Physical Oceanography, 41(6), 1116-1124. https://doi.org/10.1175/2011JPO4517.1.

Mantovanelli, A., Marone, E., Da Silva, E., Lautert, L., Klingenfuss, M., Prata Jr, V., Noernberg, M., Knoppers, B., Angulo, R.J.E., Coastal, Science, S., 2004. Combined tidal velocity and duration asymmetries as a

883 determinant of water transport and residual flow in Paranaguá Bay estuary. Estuarine, Coastal and Shelf
884 Science, 59(4), 523-537. https://doi.org/10.1016/j.ecss.2003.09.001.

885 Mashayekh Poul, H., Backhaus, J., Dehghani, A., Huebner, U.J.J.o.G.R.O., 2016. Effect of subseabed salt
886 domes on Tidal Residual currents in the Persian Gulf. Journal of Geophysical Research: Oceans, 121(5),
887 3372-3380. https://doi.org/10.1002/2015JC011421.

888 Nagy, H., Mohamed, B., Ibrahim, O.J.J.o.M.S., Engineering, 2021. Variability of Heat and Water Fluxes in the
889 Red Sea Using ERA5 Data (1981–2020). Journal of Marine Science and Engineering, 9(11), 1276.
890 https://doi.org/10.3390/jmse9111276.

891 Perrone, T.J., 1979. Winter shamal in the Persian Gulf. (p. 180). Monterey, CA: Naval Environmental
892 Prediction Research Facility.

893 Pous, S., Carton, X., Lazure, P.J.O.J.o.M.S., 2012. A process study of the tidal circulation in the Persian Gulf.
894 Open Journal of Marine Science, 2(04), 131-140. https://doi.org/10.4236/ojms.2012.24016.

895 Pous, S., Carton, X.J., Lazure, P.J.O.J.o.M.S., 2013. A process study of the wind-induced circulation in the
896 Persian Gulf. Open Journal of Marine Science, 3(1), 27160.

897 Pous, S., Lazure, P., Carton, X.J.C.S.R., 2015. A model of the general circulation in the Persian Gulf and in the
898 Strait of Hormuz: Intraseasonal to interannual variability. Continental Shelf Research, 94, 55-70.
899 https://doi.org/10.1016/j.csr.2014.12.008.

900 Reynolds, R.M.J.M.p.b., 1993. Physical oceanography of the Gulf, Strait of Hormuz, and the Gulf of Oman—
901 Results from the Mt Mitchell expedition. Marine pollution bulletin, 27, 35-59.
902 https://doi.org/10.1016/0025-326X(93)90007-7.

903 Rezaei-Latifi, A., Hosseinibalam, F.J.J.o.R.R., Sciences, A., 2015. An estimate of the surface heat fluxes
904 transfer of the Persian Gulf with the overlying atmosphere. Journal of Radiation Research and Applied
905 Sciences, 8(3), 354-361, https://doi.org/10.1016/j.jrras.2015.02.002.

906 Sadrinasab, M., Kämpf, J.J.G.r.l., 2004. Three-dimensional flushing times of the Persian Gulf. Geophysical
907 research letters, 31(24). https://doi.org/10.1029/2004GL020425.

908 Sylaios, G., Boxall, S.J.E., Coastal, Science, S., 1998. Residual currents and flux estimates in a partially-mixed
909 estuary. Estuarine, Coastal and Shelf Science, 46(5), 671-682. https://doi.org/10.1006/ecss.1997.0312.

910 Thomson, R.E., Emery, W.J., 2014. Data analysis methods in physical oceanography. Newnes.

911 Thoppil, P.G., Hogan, P.J.J.J.o.P.O., 2010. A modeling study of circulation and eddies in the Persian Gulf.
912 Journal of Physical oceanography, 40(9), 2122-2134. https://doi.org/10.1175/2010JPO4227.1.

913 Uncles, R., Jordan, M.J.E., Science, C.M., 1979. Residual fluxes of water and salt at two stations in the Severn
914 Estuary. Estuarine and Coastal Marine Science, 9(3), 287-302, https://doi.org/10.1016/0302-
915 3524(79)90042-2.

916 Uncles, R., Elliott, R., Weston, S.J.E., Coastal, Science, S., 1985. Observed fluxes of water, salt and suspended
917 sediment in a partly mixed estuary. Estuarine, Coastal and Shelf Science, 20(2), 147-167.
918 https://doi.org/10.1016/0272-7714(85)90035-6.

919 Uncles, R., Elliott, R., Weston, S., Pilgrim, D., Ackroyd, D., McMillan, D., Lynn, N.J.P.o.S.E., Bays, 1986.
920 Synoptic observations of salinity, suspended sediment and vertical current structure in a partly mixed
921 estuary. Physics of Shallow Estuaries and Bays, 16, 58-70. https://doi.org/10.1029/LN016p0058.

922 Valle-Levinson, A., 2022: Introduction to Estuarine Hydrodynamics. Cambridge University Press.
923 https://doi.org/10.1017/9781108974240.

924 Van de Kreeke, J., 2018: Dispersion in shallow estuaries. Hydrodynamics of estuaries, CRC Press, 27-40.

Vasou, P., V. Vervatis, G. Krokos, I. Hoteit, and S. J. O. D. Sofianos, 2020: Variability of water exchanges through the Strait of Hormuz. Ocean Dynamics, 70(8), 1053-1065. https://doi.org/10.1007/s10236-020-01384-2.

Wang, T., W. R. Geyer, and P. J. J. o. P. O. MacCready, 2017: Total exchange flow, entrainment, and diffusive salt flux in estuaries. Journal of Physical Oceanography, 47(5), 1205-1220. https://doi.org/10.1175/JPO-D-16-0258.1.

Xiong, J., J. Shen, and Q. J. J. o. G. R. O. Qin, 2021a: Exchange flow and material transport along the salinity gradient of a long estuary. Journal of Geophysical Research: Oceans, 126(5), e2021JC017185. https://doi.org/10.1029/2021JC017185.

Xiong, J., J. Shen, Q. Qin, and J. J. J. o. M. S. Du, 2021b: Water exchange and its relationships with external forcings and residence time in Chesapeake Bay. Journal of Marine Systems, 215, 103497. https://doi.org/10.1016/j.jmarsys.2020.103497.

Xue, P., and E. A. J. J. o. C. Eltahir, 2015: Estimation of the heat and water budgets of the Persian (Arabian) Gulf using a regional climate model. Journal of Climate, 28(13), 5041-5062, https://doi.org/10.1175/JCLI-D-14-00189.1.

Yao, F., and W. E. J. J. o. G. R. O. Johns, 2010a: A HYCOM modeling study of the Persian Gulf: 2. Formation and export of Persian Gulf Water. Journal of Geophysical Research: Oceans, 115(C11). https://doi.org/10.1029/2009JC005788.

——, 2010b: A HYCOM modeling study of the Persian Gulf: 1. Model configurations and surface circulation. Journal of Geophysical Research: Oceans, 115(C11). https://doi.org/10.1029/2009JC005781.

Zhang, Y. J., F. Ye, E. V. Stanev, and S. J. O. M. Grashorn, 2016: Seamless cross-scale modeling with SCHISM. Ocean Modelling, 102, 64-81. https://doi.org/10.1016/j.ocemod.2016.05.002.

5 Discussion

The aim of this thesis is to link the dynamics of low-inflow estuaries in the arid climate of the PG region and its coastal estuaries (such as the MRE), using numerical modeling. The thesis enhances understanding of salt-plug (***Study I***), freshwater lens (***Study II***) and inverse (***Study III***) estuarine hydrodynamics.

Salt-plug (***Study I***) and inverse (***Study III***) estuaries represent two of the main low-inflow systems. These two estuaries are characterized by hypersalinity (i.e., estuarine water is saltier than seawater) and inverse circulation under dry conditions, which is typical in the arid PG-region. This contrasts with normal estuaries in wet climates, which always have lower salinity than the adjacent seawater and exhibit classical (positive) estuarine circulation.

The MRE on the gulf's northern coast exhibits significant temporal variations, from positive and freshwater water lens estuaries in winter to inverse and salt-plug estuaries in summer (***Study II***). This thesis (in ***Study I***) provides compelling evidence that the formation and extension of a salt plug can be related not only to density gradients, but also to the tidal forcing. Prior to Study I, the salt-plug formation has been solely attributed to the density gradient. ***Study I*** also addresses lateral circulation in salt-plug estuaries for the first time.

Studies I and III, respectively, demonstrate the roles of tides on salt-plug and inverse (the PG) estuarine hydrodynamics in competition with density gradients. The tidal forcing-density gradient competition was quantified by tidal Froude number in the two estuaries. This non-dimensional number shows high values (dominating tidal forcing over baroclinicity) in the high-salinity areas of both salt-plug and inverse (the PG) estuaries. The areas encompass the zone of the salt plug (salinity maximum zone) in

salt-plug estuaries (***Study I***) and the northwestern and southern shallow banks of the PG (***Study III***). For the first time, ***Study III*** analyses the impact of high frequencies (tidal forcing) on inflowing-outflowing volume transports in the SOH. The tidal Froude number is greater than 1 at the SOH, and tidal forcing increases the annual inflow-outflow rates to approximately ±0.54 Sv, which is more than twice the rates reported in previous studies (***Study III***).

The Red Sea is another marginal sea, separated from the PG by the Arabian Peninsula. Similar to the PG, the Red Sea is characterized by permanent hypersalinity, a consequence of an arid climate and an excess of evaporation over freshwater inflows. The difference between the rates of evaporation and precipitation is 1.32 m/yr in the PG (used in Study III), which is comparable to the corresponding rate of 1.46 ± 0.24 m/yr in the Red Sea (Naghy et al., 2021). Sofianos et al. (2002) estimated the annual mean water exchange between the Red Sea and the Gulf of Aden utilizing moored current meter data collected in the Strait of Bab el Mandeb from June 1995 to November 1996. The same authors demonstrated that the annual mean inflow and outflow velocities in the Red Sea result in residual incoming and outgoing volume transports of +0.39 Sv and -0.36 Sv, respectively. Consequently, the net inflow rate of +0.03 Sv was calculated to compensate for the freshwater loss to the atmosphere. On synoptic time scales (days to weeks), high frequencies can reach magnitudes of 2-3 times the residual inflowing and outflowing volume transports (amplitudes of up to 1 Sv) in the Red Sea (Johns & Sofianos, 2012). These amplitudes of ~1 Sv are comparable with extreme volumetric 2-day-mean flow rates at the PG (Study III). Guo et al., (2022) investigated tidal effects on the monthly volume transport in the Red Sea, using models with and without tidal forcing. Similar to the findings of our PG's study (Study III), the model with tides demonstrated a higher salinity in the Red Sea, particularly during the summer months. Indeed, the intrusion of Gulf of Aden Intermediate Water (GAIW) along the main axis is reduced by approximately 100 km in summer as a result of tidal forcing (Guo et al., 2022). Furthermore, the same authors demonstrated that tidal forcing reduces the monthly mean volume transport of the GAIW by 20% on average.

This is evidenced by a decrease in the mean volume transport of the GAIW from 0.30 Sv in the non-tidal model to 0.24 Sv in the tidal model. This result is similar to the findings of the Eulerian and TEF methods in Study III, which used residual (time-averaged) properties to calculate volume fluxes. In these two methods, the inflowing and outflowing volume fluxes decrease by ~0.01 Sv from the non-tidal model to the tidal model (see Table 5 in Study III). Guo et al. (2022) elucidated the two main factors that contributed to their results. Firstly, the southward propagating tidal residual currents in the southern Red Sea act to counteract the GAIW intrusion. Secondly, the enhancement of vertical mixing along the summer thermocline and near the benthic topography of the Bab el Mandeb Strait. Tidal mixing increases the roughness of the interfaces between layers, thereby increasing friction and hindering intrusion.

Study II presents an analysis of longitudinal salinity variation in a freshwater lens estuary, which opposes the salt-plug estuaries discussed in ***Study I***. In salt-plug estuaries (***Study I***), the salinity maximum zone is replaced by a relative freshwater lens in ***Study II***. The text raises a substantial question about differences in longitudinal circulations between salt-plug and freshwater lens estuaries. It can be posited that "*the opposite longitudinal variations in salinity observed in salt-plug estuaries will result in the reversed of longitudinal circulation cells when they transition to freshwater lens estuaries."* This hypothesis is tested and supported by the findings of Studies I and II. ***Study I***, which employs an idealized funnel-shaped basin, demonstrates an inverse estuarine circulation at the down-estuary (near the mouth) and a positive circulation at the up-estuary (near the head), separated by a salinity maximum zone at the mid-estuary. ***Study II***, exhibits two positive estuarine circulations, which are detached by a mixing maximum zone in the same idealized embayment.

Study I demonstrates that differential advection is the primary driver of lateral circulations in the absence of Coriolis and wind forces. The time-averaged lateral circulations driven by the differential advection exhibit similar patterns of downwelling surface flows over the deep channel within the positive and inverse estuarine

segments of a salt-plug estuary. These lateral flows reverse in the salt plug zone and show upwelling surface flows over the deep channel. Coriolis forcing affects the lateral circulation driven by differential advection, even in narrow sections near the estuary head. The lateral circulation within the salt plug also shows clear neap-spring variability, with downwelling cells during spring tides and upwelling during neap tides.

All three studies analyze the decomposition of the net salt flux on subtidal time scales. ***Studies I and III*** use the formulation of Lerczack et al. (2006) to implement the flux decomposition at each arbitrary cross-section. **Study II** calculates the net salt flux and its relevant components per unit of width at each cross-section using observed data and the formulation of Restrepo & Kjerfve (2002).

Following the method of Lerczack et al. (2006), the net salt flux can be decomposed into three components: advection, shear dispersion and tidal oscillation at each cross-section. In salt-plug (***Study I***) and inverse (***Study III***) estuaries with low river discharge and no wind, the advective salt flux is primarily driven by tides, especially in the down-estuary. The salt transport caused by tidal advection is mainly positive (landward) in both the idealized salt-plug estuaries (***Study I***) and the inverse estuarine system of the PG (***Study III***), increasing oceanward. This salt flux is typically the strongest component, resulting in a net landward salt flux. As a result, the tidal advective salt flux increases salinity in the PG (***Study III***). Similarly, an increase in tidal forcing at the mouth of the idealized salt-plug estuary results in higher salinities in the salt-plug zone. In fact, the location of the salt plug is controlled by the main longitudinal salt transports of tidal advection (***Study I***). In addition to the strong landward salt flux by tidal advection, strong tidal mixing in the PG, especially at the SOH, contributes to the increase in PG-salinity (***Study III***).

Salt flux by shear dispersion is generated by horizontal salinity gradients. It typically transports salt from high-salinity areas to lower salinity areas. Therefore, this salt flux is usually landward in positive estuaries and seaward in inverse estuaries on subtidal time scales. ***Study I*** shows that the direction of the sheared salt flux changes from

landward in the positive estuarine segment to seaward direction in the inverse system of a salt-plug estuary. In the inverse estuary of the PG, the salt flux by shear dispersion is always seaward and increases towards the SOH (***Study III***).

Study III shows that the tidal pumping of salt in the PG is characterized by insignificant seaward values on annual time scales. ***Study I*** also shows that on subtidal timescales, this salt flux exhibits almost seaward values at the salinity maximum zone of salt-plug estuaries. The salt flux by tidal oscillation may be influenced by interactions between strong tidal flows and bathymetric changes. ***Study I*** shows that in meso-tidal salt-plug estuaries, a peak in landward tidal salt flux occurs at a location with sudden bathymetric change.

At the MRE (***Study II***), the strong hypersaline runoff driven the freshwater lens estuary results in the dominance of the advective salt flux over other flux terms using the formulation of Restrepo & Kjerfve (2002). As a result, there is a net seaward salt transport throughout the estuary with a net salt transport of 680.18 psu cm/s from the estuary mouth to the PG. ***Study II*** also shows that of all the terms contributing to the net salt flux, the salt flux component of the cross-correlation between sea-level and salinity is in phase with the depth- and time-averaged velocity near the mouth, which coincides with a landward decrease in salinity due to the low-water lens. Conversely, it is out of phase with the mean velocity near the head, where salinity increases landward due to hypersaline runoff. Numerical experiments in ***Study II***, show that the hypersaline runoff should have a discharge of at least 400 m^3/s to dampen the tidal level at the head. ***Study II*** also investigates the effect of a 20 cm sea level rise on the longitudinal salinity of the MRE in its four temporal estuarine states: positive and freshwater lens estuaries in wet months (winter), and inverse and salt-plug estuaries in dry months (summer). Sea level rise increases salinity in the wintertime estuaries and slightly decreases it in the summertime estuaries.

Future Research Suggestions

Some important physical characteristics of low-inflow regional-coastal estuaries in the arid climate of the PG are presented in this thesis. Further research is required to investigate other hydrodynamic issues and biogeochemical processes in this area. Suggestions for future studies are provided below.

- **Wind – baroclinicity competition in salt-plug estuaries**

This study investigates the formation and extension of a salt plug resulting from the interplay between tides and density gradients. However, there is still a gap in our understanding of the hydrodynamics of salt-plug estuarine systems with regard to the competition between wind–baroclinicity in forming and/or modifying the extension of the salt plug. This competition can be quantified using the non-dimensional Wedderburn number (Valle-Levinson, 2022).

- **Implementation of more observational studies in the MRE**

The in-situ observations of the MRE are limited and indicate the presence of a freshwater lens in winter and a salt plug in summer. Further observational studies are needed to link the physical and biogeochemical processes in these estuaries. Additionally, the transition of estuarine states between positive and freshwater lens estuaries in wet months, and especially between inverse and salt-plug estuaries in dry months, needs to be investigated in more detail. These studies can improve our understanding of the complex interplay of factors in the MRE and its ecological implications in the different temporal estuarine systems. The studies can also provide valuable insights for the management, conservation, and sustainable use of the MRE ecosystem.

- **Wind impacts on volume transport in the SOH and on PG-salinity**

Both wind and tides play an important role in influencing the exchange flow between the PG and the Oman Sea. The prevailing northwesterly wind in the region acts against

the inflow from the Indian Ocean. This work has only considered the tidal effects on the volume transports and has shown that tides contribute to an increase in salinity in the PG. Therefore, it is suggested that future studies focus on investigating the impact of wind on volume and salt transport at the SOH and on salinity distribution in the PG.

In particular, extreme net-flow rates greater than ~ ±0.25 Sv in the two experiments of CRM (control run model including all forcings) and NTM (non-tidal model) disappear in the NWM (non-wind model) (see Fig. 5a, b from Study III and Figure 1). This indicates that the extreme net volume fluxes are caused by strong wind-induced flow rates on synoptic time scales.

Also, the seasonal mean flows and salinities averaged in the upper 50 m from the CRM and NWM are compared in winter and summer 2001 (Figure 2). It can be observed that the prevailing northwesterly wind opposes the IOSW inflow to the PG. Subsequently, turning off wind forcing (in the NWM) results in the prolongation of low-salinity incursions from the IOSW along the northern and southern coasts in both seasons (compare Figure 2a with Figure 2c, and Figure 2b with Figure 2d). Consequently, the salinity distributions of the PG undergo a substantial change at the NWM.

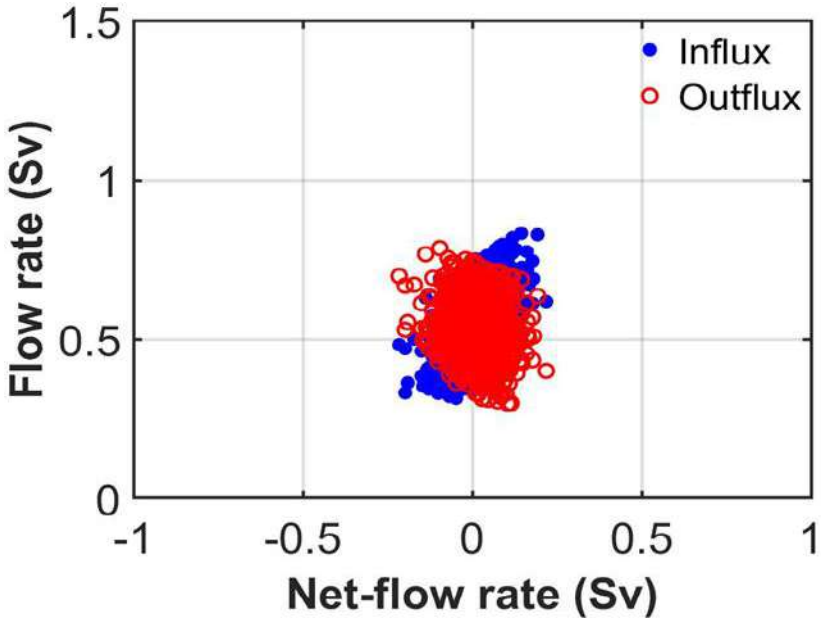

Figure 1. *Volumetric 2-day-mean flow rates across the SOH at latitude 26° N during the last 5 years (1997-2001) of the NWM. see the location of the cross-section in Fig. 1 of Study III.*

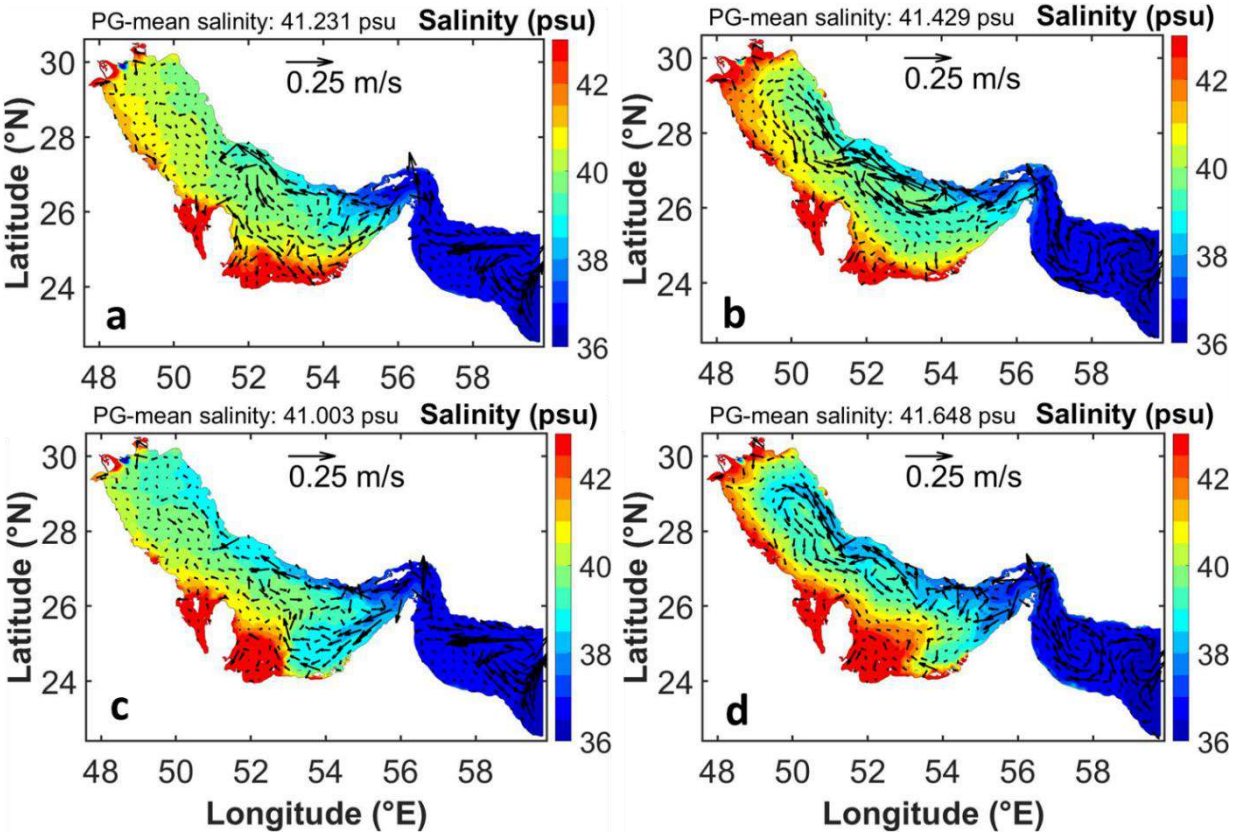

Figure 2. *Seasonal mean flows and salinities averaged in the upper 50 m from the CRM (a, b) and NWM (c, d) in winter (a, c) and summer (b, d) 2001. The salinity values averaged at the PG-area (47.5° E- 56.25° E) are also presented above each figure.*

- **Biochemical modeling in the PG**

In light of the scarcity of biogeochemical modeling studies in the PG, it is of the utmost importance to investigate the impacts of physical processes on ecological parameters and nutrient transport in this gulf.

One of the few ecological modelling studies conducted in the PG was undertaken by Lachkar et al. (2022). Using the Regional Ocean Modeling System (ROMS), they investigated seasonal and interannual variations of O2 reduction (hypoxia) in the PG from 1982 to 2010. They showed that a strong hypoxia exists at deep layers of the central part of the PG with a spatial peak in the mid-autumn. During the 29 years (1982-2010), the hypoxic waters cover the rate of 3818 km^2 per decade at the PG.

In another study, de Verneil et al. (2021) used a simple 1-dimensional (vertical) biogeochemical model in the reef basin of the southern shallow banks of the PG to interpret O2 measurements. They quantified estimates of the O2 fluxes produced by photosynthesis both in the water column and within the coral framework. Their model showed that the dominant contribution to the O2 fluxes occurs in the water, through photosynthesis and respiration.

6 Synthesis

The three individual studies presented in this thesis offer a holistic understanding of estuarine hydrodynamics in the arid PG region, with a particular emphasis on the influence of tidal forcing. The overarching goal of this research is to provide valuable insights into the behavior of low-inflow estuaries, focusing on the unique conditions of the PG's inverse estuary, salt-plug estuaries, and the freshwater lens system in the MRE. By integrating observational data, numerical modeling, and theoretical analyses, this synthesis seeks to present a broader understanding of estuarine hydrodynamics, particularly in arid climates. It enhances the context provided by previous studies and contributes to future regional-coastal oceanographic and estuarine studies.

Contributions to science

1. Advancing previous research on estuarine hydrodynamics

The findings of this thesis extend previous research in estuarine hydrodynamics. While prior studies have mostly focused on positive estuaries, this thesis contributes significantly to the understanding of low-inflow estuarine hydrodynamics in arid climates. The thesis addresses previously unexplored hydrodynamical features in the low-inflow estuarine systems. In particular, the integration of the three studies elucidates complex interactions between low-salinity water and high-salinity water masses, with an emphasis on the role of tidal forcing in comparison to density gradients. It bridges critical gaps in the existing literature. The thesis is also beneficial for the management of the regional-coastal area of the PG, as it provides detailed explanations of physical-hydrodynamical knowledge and demonstrates the continuum of the regional system of the PG and its coastal areas, such as the MRE.

Study I- Idealized salt-plug estuary

Study I offers innovative insights into the hydrodynamics of salt-plug estuaries. Earlier studies of salt-plug estuaries have linked the formation of the salinity maximum zone solely to the density gradient. However, this study demonstrates that tidal forcing can also contribute to the formation and location of the salt plug zone. Residual lateral circulations in salt-plug estuaries are also presented in Study I for the first time, demonstrating their significance in understanding the circulation patterns within these estuaries. Furthermore, the employment of a three-dimensional hydrodynamic model to demonstrate different scenarios in an idealized funnel-shaped salt-plug system contributes to the theoretical framework for salt-plug estuarine classification.

Study I introduces a threshold for salt-plug estuaries, where a tidal Froude number of 1000 indicates tidal forcing overwhelming density gradients. This condition results in the formation of a robust salinity maximum zone , which is identified by a high Ekman number exceeding 1.78. Therefore, the framework (estuarine classification) is introduced for salt-plug estuaries based on Ekman and tidal Froude numbers.

This foundational study sets the stage for understanding how specific hydrodynamic mechanisms can be generalized to real-world salt-plug estuaries in subsequent studies.

Study II- Freshwater lens estuary in the Mond River Estuary

Study II extends to the understanding of low-inflow estuaries in arid coasts, focusing on the MRE's temporal variability. These types of estuaries highlight strong seasonal variability in response to fluctuations in river discharges and evaporation rates altering from the positive estuary in wet months to inverse and salt-plug estuarine systems during dry months. In addition to these three estuarine types, the MRE exhibits the highly unsteady condition of freshwater lens estuary. This study combines numerical modeling and observations to characterize the physical aspects of the freshwater lens and assesses the impact of sea level rise on the estuary's various states.

A notable absence of research exists on the estuarine hydrodynamics within the MRE, largely due to the deficiency of available measurements. The few relevant studies investigated stratification-mixing conditions associated with tidal dynamics when this estuary acts as a typical positive estuary (Azad et al., 2019) and is affected by salt-water river inflows, imposing a freshwater lens state (Hosseini & Siadatmousavi, 2018).

Study III- Inverse estuary of the Persian Gulf:

The findings of Study III have implications for understanding the role of tides in inverse estuaries. This study examines the inverse estuary dynamics of the PG, highlighting the significant role of tidal forcing in volume and salt transports through the SOH and the resultant effects on salinity distribution in the PG. Previous studies (see Table 1 in Study III) estimated annual inflow-outflow rates mostly ~0.2 Sv and rarely investigated the salinity transport into the PG by different mechanisms, particularly by tidal forcing. Study III challenges the previous estimates by demonstrating that tidal forcing significantly enhances annual inflow-outflow rates to higher values of 0.5 Sv. This study also shows that tides play a substantial role in salinity distribution in the PG. Tidal forcing not only amplifies density gradients to exchange flows but also reinforces vertical mixing in the PG, particularly at the SOH.

2. Connecting to future oceanographic studies

The fundamental hydrodynamical view presented in this thesis will facilitate future studies analyzing both physical and biogeochemical properties in highly evaporative regional-coastal ecosystems. For instance, a review of the literature on positive estuaries reveals that secondary (lateral) circulation plays a crucial role in the estuarine properties (Geyer et al., 1998; Stieglitz & Ridd, 2001; Huijts et al., 2006; Fugate et al., 2007; Kim & Voulgaris, 2008; Seim et al., 2009; Huijts et al., 2011; Lacy et al., 2014; Zhu et al., 2018; Chen et al., 2020). In the context of estuarine hydrodynamics, the present thesis (Study I) is the first to investigate lateral circulations in salt-plug estuaries. The results obtained will therefore be of great assistance to future studies investigating the

impact of lateral flows on stratification conditions, sediment dynamics and biogeochemical cycling in this particular type of low-inflow estuaries. The secondary circulation facilitates the dispersion of salt and other tracers in estuarine systems, thereby affecting ecosystem dynamics. For example, Stieglitz & Ridd (2001) showed that the spatial distribution of mangroves in the Normanby River estuary, situated in northeast Australia, is predominantly influenced by secondary estuarine circulation. The lateral flows also affect cross-channel salinity differences and vertical stratification (e.g., Seim et al., 2009; Zhu et al., 2018). Additionally, the secondary flows transport sediments laterally (Fugate et al., 2007; Chen et al., 2020), influencing the estuarine turbidity maximum (Geyer et al., 1998) and sediment trapping patterns (Kim & Voulgaris, 2008; Lacy et al., 2014). This, in turn, influences estuarine morphology (Huijts et al., 2006 and 2011) and the biogeochemical cycling associated with sediment (Chen et al., 2020).

A weak seaward flushing of low-riverine waters and a considerable landward intrusion of ocean waters may potentially drive a relatively longer residence time in the low-inflow estuaries in comparison to positive estuaries with a significant river discharge. Consequently, low-inflow estuaries can be more susceptible to water quality issues than positive estuaries (Valle-Levinson, 2010; Cabrera et al., 2014; Shaha et al., 2022). The related studies on the low-inflow estuarine hydrodynamics (Study I on salt-plug estuaries and Study III on the inverse estuary of the PG) can be used to provide valuable information on the dispersion of pollutants and nutrients in these estuaries. The resulting information will have significant benefits for managing water quality issues in the low-inflow estuaries.

Research in estuarine hydrodynamics can contribute to an understanding of how estuaries may respond to climate change impacts (e.g. sea level rise, increasing sea surface temperature, and consequent changes in evaporation and salinity values) and anthropogenic pressures (such as dam constructions at estuary upstream and desalination of seawater in arid regions like the PG). Study II examines the impact of a

sea level rise on longitudinal salinity variations in different estuarine systems of the MRE, including positive, inverse, freshwater lens, and salt-plug estuaries. It provides a foundation for future studies investigating the impact of climate change on estuarine hydrodynamics.

Biogeochemical parameters in estuaries with significant seasonal salinity variations, such as the MRE (Study II), may exhibit similar temporal variability. In particular, the different time-dependent estuarine systems of the MRE result from variations in evaporation-precipitation and fresh- and salt-river discharges. These variations lead to different residence times and water ages that connect to water quality issues. This thesis can therefore serve as a foundation for further studies exploring biogeochemical processes, residence times, and water quality in these estuaries.

The study of volume and salinity transport into the regional inverse estuary of the PG (Study III) provides valuable insights into the biogeochemical processes of gulf systems. For example, understanding volume and salinity variations helps to quantify nutrient inputs through the SOH. The water exchange influences oxygen distribution, dissolved inorganic carbon, and alkalinity. Regional gulf systems generally play a role in global carbon budgets. Therefore, the thesis may be used to quantify the PG contribution to changing biogeochemical conditions on global scales.

The thesis examines the influence of tidal forcing and density gradient competition on the formation of residual flows in salt-plug (Study I) and inverse (Study III) estuaries. The different residual flows, which are either dominated by tides or density gradients or a combination of both, can result in dissimilarities in residual sediment and nutrient transports in these two particular types of low-inflow estuaries. In contrast to density gradients, which control the vertical stratification of water masses, tidal forcing enhances vertical mixing. Both tidal forcing and density gradients can affect water and salinity exchanges. Hence, the findings of this thesis are useful for studying biogeochemical conditions in both regional-coastal inverse and salt-plug estuaries.

Conclusions

This thesis presents novel insights into estuarine hydrodynamics in arid climates, with the PG area serving as a case study. These insights are integrated with a refined comprehension of tidal impacts on salt-plug and inverse estuaries. The findings can be linked to the broader scientific understanding of low-inflow estuaries globally. This thesis not only fills some critical knowledge gaps in low-inflow estuarine hydrodynamics, but its results also serve as a foundation for further biogeochemical research in similar embayments. The principal findings of this thesis account for lateral circulations in salt-plug estuaries, volume and salinity transport in inverse estuaries, and tidal forcing-density gradient competition in these two categories of low-inflow estuaries. Furthermore, the impact of rising sea-level on longitudinal salinity variations in positive, freshwater lens, inverse and salt-plug estuaries can be explained. All of these findings have the potential to inform useful tools for estuarine ecosystem management, biogeochemical conditions, sediment transport, and the sustainable development of coastal areas with the impact of climate change. By synthesizing the results of three distinct studies, this thesis emphasizes the importance of tidal forcing in influencing low-inflow estuarine dynamics and provides a foundation for future research and management strategies in arid coastal-regional estuarine systems. In particular, there is a pressing need for further research to bridge the gaps between biogeochemical and physical processes in the PG and its coastal estuarine basins.

References

Aboobacker, V. M., Shanas, P. R., Al-Ansari, E. M., Sanil Kumar, V., & Vethamony, P. (2021). The maxima in northerly wind speeds and wave heights over the Arabian Sea, the Arabian/Persian Gulf and the Red Sea derived from 40 years of ERA5 data. Climate Dynamics, 56, 1037-1052.

Al-Muzaini, S., & Jacob, P. G. (1996). Marine plants of the Arabian Gulf. Environment International, 22, 369-376.

Alosairi, Y., Alsulaiman, N., Petrov, P., & Karam, Q. (2019). Responses of salinity and chlorophyll-a to extreme rainfall events in the northwest Arabian Gulf: Emphasis on Shatt Al-Arab. Marine Pollution Bulletin, 149, 110564.

Azad, M. T., Mehrfar, H., Mansouri, D., & Pasand, M. M. (2019). A physical study on tidal currents in Mond and Helleh rivers in the Persian Gulf. Res. Mar. Sci., 4(2), 518-527.

Azizpour, J., Siadatmousavi, S. M., & Chegini, V. (2016). Measurement of tidal and residual currents in the Strait of Hormuz. Estuarine, Coastal and Shelf Science, 178, 101-109.

Cabrera, O. C., Villanoy, C. L., Jacinto, G. S., Bernardo, L. P. C., Ferrera, C. M., Velasquez, I. B., & Azanza, R. V. (2014). Salt-plug estuarine circulation in Malampaya sound, Palawan, Philippines. Phil. Sci. Lett, 7, 428-437.

Campos, E. J. D., Gordon, A. L., Kjerfve, B., Vieira, F., & Cavalcante, G. (2020). Freshwater budget in the Persian (Arabian) Gulf and exchanges at the Strait of Hormuz. PLoS ONE, 15, e0233090.

Chant, R. J. (2010). Estuarine secondary circulation. In Contemporary issues in estuarine physics (pp. 731-49). Cambridge University Press.

Chao, S. Y., Kao, T. W., & Al-Hajri, K. R. (1992). A numerical investigation of circulation in the Arabian Gulf. Journal of Geophysical Research: Oceans, 97, 11219-11236.

Chen, L., Gong, W., Zhang, H., Zhu, L., & Cheng, W. (2020). Lateral circulation and associated sediment transport in a convergent estuary. Journal of Geophysical Research: Oceans, 125(8), e2019JC015926.

de Verneil, A., Burt, J. A., Mitchell, M., & Paparella, F. (2021). Summer oxygen dynamics on a southern Arabian gulf coral reef. Frontiers in Marine Science, 8, 781428.

Fugate, D. C., Friedrichs, C. T., & Sanford, L. P. (2007). Lateral dynamics and associated transport of sediment in the upper reaches of a partially mixed estuary, Chesapeake Bay, USA. Continental Shelf Research, 27(5), 679-698.

Geyer, W. R., Signell, R. P., & Kineke, G. (1998). Lateral trapping of sediment in a partially mixed estuary. In D. Scheffers (Ed.), Physics of Estuaries and Coastal Seas (pp. 115–124). Rotterdam: Balkema.

Ghaemi, M., & Gholamipour, S. (2017). Seasonal Measurement of Nutrient Concentrations and Total Alkalinity in the Mond Estuary Ecosystem. Journal of Oceanography, 8, 11-18.

Guo, D., Yao, F., Zhan, P., Krokos, G., & Hoteit, I. (2022). Hindrance effect of tides on water exchanges between the Red Sea and the Gulf of Aden. Frontiers in Marine Science, 9, 964097.

Hosseini, S. T., & Siadatmousavi, S. M. (2018). Field observations of hypersaline runoff through a shallow estuary. Estuarine, Coastal and Shelf Science, 202, 54-68.

Huijts, K. M. H., De Swart, H. E., Schramkowski, G. P., & Schuttelaars, H. M. (2011). Transverse structure of tidal and residual flow and sediment concentration in estuaries: Sensitivity to tidal forcing and water depth. Ocean Dynamics, 61(8), 1067–1091. https://doi.org/10.1007/s10236-011-0414-7

Huijts, K. M. H., Schuttelaars, H. M., de Swart, H. E., & Valle-Levinson, A. (2006). Lateral entrapment of sediment in tidal estuaries: An idealized model study. Journal of Geophysical Research, 111, C12016. https://doi.org/10.1029/2006JC003615

Johns, W. E., & Sofianos, S. S. (2012). Atmospherically forced exchange through the Bab el Mandeb Strait. Journal of physical oceanography, 42(7), 1143-1157.

Johns, W. E., Yao, F., Olson, D. B., Josey, S. A., Grist, J. P., & Smeed, D. A. (2003). Observations of seasonal exchange through the Straits of Hormuz and the inferred heat and freshwater budgets of the Persian Gulf. Journal of Geophysical Research: Oceans, 108.

Juarez, B., Valle-Levinson, A., & Li, C. (2020). Estuarine salt-plug induced by freshwater pulses from the inner shelf. Estuarine, Coastal and Shelf Science, 232, 106491.

Juarez, B., Valle-Levinson, A., & Canestrelli, A. (2022). Mechanisms of Estuarine Salt-Plug Formation by an Along-Shelf Buoyant Current: A Numerical Model Approach. Journal of Geophysical Research: Oceans, 127, e2021JC017971.

Kämpf, J., & Sadrinasab, M. (2006). The circulation of the Persian Gulf: a numerical study. Ocean Science, 2, 27-41.

Kim, Y. H., & Voulgaris, G. (2008). Lateral circulation and suspended sediment transport in a curved estuarine channel: Winyah Bay, SC, USA. Journal of Geophysical Research, 113, C09006. https://doi.org/10.1029/2007JC004509

Lachkar, Z., Mehari, M., Levy, M., Paparella, F., & Burt, J. A. (2022). Recent expansion and intensification of hypoxia in the Arabian Gulf and its drivers. Frontiers in Marine Science, 9, 891378.

Lacy, J. R., Gladding, S., Brand, A., Collignon, A., & Stacey, M. (2014). Lateral baroclinic forcing enhances sediment transport from shallows to channel in an estuary.

Estuaries and Coasts, 37(5), 1058–1077. https://doi.org/10.1007/s12237-013-9748-3

Lardner, R. W., & Das, S. K. (1991). On the computation of flows driven by density gradient: Residual currents in the Arabian Gulf. Applied mathematical modelling, 15, 282-294.

Largier, J. L. (2023). Recognizing low-inflow estuaries as a common estuary paradigm. Estuaries and Coasts, 46(8), 1949-1970.

Lerczak, J. A., Geyer, W. R., & Chant, R. J. (2006). Mechanisms driving the time-dependent salt flux in a partially stratified estuary. Journal of Physical Oceanography, 36, 2296-2311.

Lorenz, M., Klingbeil, K., & Burchard, H. (2020). Numerical study of the exchange flow of the Persian Gulf using an extended total exchange flow analysis framework. Journal of Geophysical Research: Oceans, 125, e2019JC015527.

Marcella, M. P., & Eltahir, E. A. (2008). The hydroclimatology of Kuwait: explaining the variability of rainfall at seasonal and interannual time scales. Journal of hydrometeorology, 9, 1095-1105.

Mariani, R., Lessa, G. C., & Marta-Almeida, M. (2022). Long-term Variability of the Salinity Field in a Large Tropical, Well-Mixed Estuary: the Influence of Climatic Trends. Estuaries and Coasts, 1-16.

Nagy, H., Mohamed, B., & Ibrahim, O. (2021). Variability of heat and water fluxes in the red sea using ERA5 data (1981–2020). Journal of Marine Science and Engineering, 9(11), 1276.

Pous, S., Carton, X., & Lazure, P. (2012). A process study of the tidal circulation in the Persian Gulf. Open Journal of Marine Science, 2, 131-140.

Pous, S., Carton, X. J., & Lazure, P. (2013). A process study of the wind-induced circulation in the Persian Gulf. Open Journal of Marine Science, 3(1), 27160.

Pous, S., Lazure, P., & Carton, X. (2015). A model of the general circulation in the Persian Gulf and in the Strait of Hormuz: Intraseasonal to interannual variability. Continental Shelf Research, 94, 55-70.

Privett, D. W. (1959). Monthly charts of evaporation from the N. Indian Ocean (including the Red Sea and the Persian Gulf). Quarterly Journal of the Royal Meteorological Society, 85, 424-428.

Restrepo, J. D., & Kjerfve, B. (2002). The San Juan Delta, Colombia: tides, circulations, and salt dispersion. Continental Shelf Research, 22, 1249-1267.

Reynolds, R. M. (1993). Physical oceanography of the Gulf, Strait of Hormuz, and the Gulf of Oman—Results from the Mt Mitchell expedition. Marine pollution bulletin, 27, 35-59.

Sadrinasab, M., & Kämpf, J. (2004). Three-dimensional flushing times of the Persian Gulf. Geophysical research letters, 31.

Seim, H. E., Blanton, J. O., & Elston, S. A. (2009). The effect of secondary circulation on the salt distribution in a sinuous coastal plain estuary: Satilla River, GA, USA. Continental Shelf Research, 29(1), 15-28.

Shaha, D. C., & Cho, Y. K. (2016). Salt plug formation caused by decreased river discharge in a multi-channel estuary. Scientific Reports, 6, 1-11.

Shaha, D. C., Cho, Y. K., Kundu, S. R., Hasan, J., Haque, F., & Salam, M. A. (2022). The calculation of flushing time for the upper Pasur River Estuary, Bangladesh. Terrestrial, Atmospheric and Oceanic Sciences, 33, 15.

Sheppard, C. (2019). World seas: an environmental evaluation. Academic Press London.

Sofianos, S. S., Johns, W. E., & Murray, S. P. (2002). Heat and freshwater budgets in the Red Sea from direct observations at Bab el Mandeb. Deep Sea Research Part II: Topical Studies in Oceanography, 49(7-8), 1323-1340.

Stieglitz, T., & Ridd, P. V. (2001). Trapping of mangrove propagules due to density-driven secondary circulation in the Normanby River estuary, NE Australia. Marine Ecology Progress Series, 211, 131-142.

Swift, S. A., & Bower, A. S. (2003). Formation and circulation of dense water in the Persian/Arabian Gulf. Journal of Geophysical Research: Oceans, 108, 4-1-4-21.

Thoppil, P. G., & Hogan, P. J. (2010). A modeling study of circulation and eddies in the Persian Gulf. Journal of Physical Oceanography, 40, 2122-2134.

Valle-Levinson, A. (2011). 1.05 Classification of Estuarine Circulation. Treatise on estuarine and coastal science, 75-86.

Valle-Levinson, A. (2010). Contemporary issues in estuarine physics. Cambridge University Press.

Valle-Levinson, A. (2022). Introduction to Estuarine Hydrodynamics. Cambridge University Press.

Valle-Levinson, A., & Bosley, K. T. (2003). Reversing circulation patterns in a tropical estuary. Journal of Geophysical Research: Oceans, 108.

Wolanski, E. (1986). An evaporation-driven salinity maximum zone in Australian tropical estuaries. Estuarine, Coastal and Shelf Science.

Zhang, Y. J., Ye, F., Stanev, E. V., & Grashorn, S. (2016). Seamless cross-scale modeling with SCHISM. Ocean Modelling, 102, 64-81.

Zhu, L., He, Q., & Shen, J. (2018). Modeling lateral circulation and its influence on the along-channel flow in a branched estuary. Ocean Dynamics, 68, 177-191.

Acknowledgements

Four years ago, I embarked on a great adventure of learning and growth, beginning with the relocation of my family and myself from our homeland, Iran. During this period, I've had the privilege of meeting many inspiring individuals and gaining invaluable insights into science and life in general. Thank you, Corrina, for putting me in this position. I'm also grateful for your professional and moral support along with positive outlook, which have given me the confidence to keep moving forward on this adventure. I'd also like to thank Emil and Johannes, who have also taught me a lot. In particular, I'd like to thank Emil for our great discussions on various aspects of my PhD research and for spending as much time as he did to improve my papers. Thank you, Emil, for all your support and for sharing your valuable experience and knowledge with me. Many thanks, Johannes, for your commitment and all the support and encouragement you've given me over the years, especially when I've needed advice on solving my technical modeling problems and scientific issues.

I extend my sincere thanks to Arnoldo Valle-Levinson (University of Florida), who has been great to work with on our joint paper. Arnoldo, your great comments on the first paper really improved it. Thanks again! I also appreciate Marvin Lorenz (Leibniz Institute for Baltic Sea Research), who's already worked on the physical oceanography of the Persian Gulf and I ’ve benefitted from his valuable comments.

I'd like to express my gratitude to SICCS Graduate School, especially Annette Eschenbach (Head of SICSS), Berit Hachfeld (Doctoral Programme Coordinator) and Eduardo Zorita-Calvo (my panel chair) for all their help and support. Thanks also to Eduardo for his great comments on this thesis and related papers.

Special thanks go to my friends Lucas, Nils and Peter who have always been there to help me with work or personal issues. This dissertation wouldn’t have been possible without your support. Thank you, Benjamin, you've provided excellent guidance on modeling and effective solutions to related issues. I also appreciate all the wonderful former and current colleagues at Helmholtz-Zentrum Hereon who have created a positive and enjoyable working atmosphere: Jan, Mengyao, Pooja, Pascal, Himansu, Deborah, Ute, Kai, Sabine, Joanna, Robert, Philip-Neri, Wei, Luciana, Nour, Nasim, Bing, Nam, Thao, Douglas, Kelli, and everyone else I may have forgotten to mention – my apologies!

I'm profoundly grateful for the tremendous support of my family. My deepest thanks go to my wife, Elaheh, and our son, Yasin, for accompanying and encouraging me on this journey from the very beginning.